



**HAL**  
open science

# Compact multiscale modeling of carbon-based nano-transistors

Yi Zheng

► **To cite this version:**

Yi Zheng. Compact multiscale modeling of carbon-based nano-transistors. Electromagnetism. Sorbonne Université, 2018. English. NNT : 2018SORUS518 . tel-03125275

**HAL Id: tel-03125275**

**<https://theses.hal.science/tel-03125275>**

Submitted on 29 Jan 2021

**HAL** is a multi-disciplinary open access archive for the deposit and dissemination of scientific research documents, whether they are published or not. The documents may come from teaching and research institutions in France or abroad, or from public or private research centers.

L'archive ouverte pluridisciplinaire **HAL**, est destinée au dépôt et à la diffusion de documents scientifiques de niveau recherche, publiés ou non, émanant des établissements d'enseignement et de recherche français ou étrangers, des laboratoires publics ou privés.

# Sorbonne Université

Ecole doctorale : Science Mécanique Acoustique Electronique et Robotique

(SMAER)

*Laboratoire d'Electronique et Electromagnétisme*

## **Compact Multiscale Modeling of Carbon-Based Nano-transistors**

Par Yi ZHENG

Thèse de doctorat d'Électronique

Présentée et soutenue publiquement le 19/12/2018

Devant un jury composé de :

M. Philippe Dollfus, Directeur de recherche CNRS	Rapporteur
M. Thomas Zimmer, Professeur des Universités	Rapporteur
M. Stéphane Clenet, Professeur des Universités	Examineur
M. Marco Saitta, Professeur des Universités	Examineur
M. Zhuoxiang Ren, Professeur des Universités	Directeur de thèse
M. Guido Valerio, Maitre de Conférences HDR	Co-encadrant de thèse
M. David Brunel, Maitre de Conférences	Co-encadrant de thèse



Except where otherwise noted, this work is licensed under  
<http://creativecommons.org/licenses/by-nc-nd/3.0/>

*Dédicace*

This research is dedicated:

To my supervisors: Associate Prof. Guido VALERIO, David BRUNEL, and Prof. Zhuoxiang REN, for their valuable instructions and suggestions.

To my parents: my father “ZHENG Bo” and mother “LI Jingzhong”, for their understanding, respecting my choice and caring for me.

To my husband: HungChyun CHOU, thank you for sharing your experience, giving me support without any complaint.

# Acknowledgements

First and foremost, I would like to express my deep appreciation to my supervisors: Associate Prof. Guido VALERIO and Prof. Zhuoxiang REN for their patient guidance and suggestions. Without their invaluable help and generous encouragement, this thesis would not have been accomplished. I am grateful to Associate Prof. David BRUNEL for supervising me with advice and experimental resources on my thesis.

I am also thankful to the members of jury; particularly the reviewers M. Philippe Dollfus and M. Thomas Zimmer who gave me very useful recommendations, and M. Stéphane Clenet and M. Marco Saitta.

Besides, I wish to thank my colleague Fernando ZANELLA, I often have warm discussion with him about graphene modeling, who also built the model by different method.

Also, I would like to express my sincere gratitude to China Scholarship Council (CSC) for providing me opportunity to complete this work.

Last but not least, I would like to express my special thanks to my beloved parents and husband, whose care, endless love and support motivate me progress and make me want to be a better person.

# Contents

Acknowledgements .....	2
Contents.....	3
Abstract .....	5
Chapter 1. Introduction .....	7
1.1 Research background .....	7
1.2 Electronic properties of a graphene sheet .....	11
1.3 Energy bands of graphene nanoribbons .....	16
1.4 Review of modeling methods for nano-transistors .....	18
1.4.1 Carrier transport model in GFET .....	19
1.4.2 Analytical models for GFET .....	20
1.5 Modelling methods used in this thesis .....	22
1.5.1 Micromodel: the Non-equilibrium Green's function .....	24
1.5.2 Micromodel: the Semi-analytic multiscale approach.....	27
1.6 Approximated quantities describing nanoribbon energy-bands.....	28
1.7 Research Objectives .....	31
1.7.1 Graphene nanoribbon based transistors.....	31
1.7.2 Graphene nanomesh based transistors.....	33
Chapter 2. Dispersion Relations under Deformation and Schottky Field-Effect Transistor....	36
2.1 Energy bands of a deformed graphene nanoribbon.....	36
2.2 Effective mass and density of states.....	45

2.3. Deformations in Schottky Field-Effect Transistor .....	48
2.4 Study of deformation effects on carbon-based transistors with Semi-Analytic and Ab-Initio Models .....	49
2.5. Semi-analytical multiscale coupled modeling.....	53
2.5.1 A short discussion on the tight binding model without variation of hopping parameters .....	54
2.5.2 The full model of deformation: the Ballistic regime.....	59
2.5.3 Partially Ballistic regime .....	68
2.5.4 On/Off current ratio and differential conductance with different deformations .....	73
2.5.5 Shift of transfer characteristics with different SB height.....	76
Chapter 3. Application of Nanomesh in Field-Effect Transistor .....	78
3.1 Graphene nanomesh and its electronic properties.....	78
3.2 Compact model validation with <i>ab-initio</i> method.....	83
3.3 Graphene nanomesh transistor and its <i>I-V</i> characteristics.....	88
3.4 Numerical and experimental study of graphene nanomesh transistor.....	93
Conclusions and Perspectives .....	99
Annex: Experiments on graphene transistors at Chang Gung University.....	101
A.1 Chemical Vapor Deposition (CVD) method to produce graphene and graphene transfer technology .....	101
A.2 Deformation of pristine graphene based transistor in CGU .....	102
List of Publications.....	106
Bibliography.....	108

# Abstract

Among emerging carbon materials, graphene has rapidly become an ideal candidate for nano-electronics. In this context, different methods have been proposed to transform its electric properties and remove the Dirac degeneracy point, leading to application to nano-transistors. In this thesis we apply a semi-analytical compact model to study two kinds of graphene-based nanotransistors: nanoribbon graphene transistor and nanomesh transistor. A tight-binding model is used to determine analytical expressions for the energy bands of a graphene nanoribbon. Comparisons are shown with *ab-initio* approaches and with measurements done on larger-scale transistors of the same kind.

In the context of flexible electronics, mechanical stresses on circuits and subsequent geometric deformations of graphene-based components is an important issue. We investigate these effects on the conduction properties of nanoribbon transistors (both in ballistic and partially ballistic regimes). By assuming the presence of small deformations, a spectral scaling and a spectral shift due to the presence of a deformation can be taken into account analytically. This model leads to define in closed form effective quantities (masses, densities of states) used to numerically calculate potentials and currents in the nano-device. Numerical results are shown both in a ballistic and partially-ballistic regime, with and without the presence of Schottky contacts. The proposed results in Chapter 2 illustrate in a very simple way how the deformation of graphene nanoribbon influences the  $I$ - $V$  characteristics of transistor.

Another solution to realize graphene nanotransistor is the etching of nanoholes in a graphene sheet (thus realizing a nanomesh). If graphene nanomesh is properly shaped, the On/Off current ratio of transistor is expected to be enhanced. In Chapter 3, the semi-analytic method is used to evaluate the performance of nanomesh transistor with nanoribbon ones. The results are again compared with an *ab-initio* method.  $I$ - $V$  characteristics of graphene nanomesh transistor are presented and compared with experimental results. The proposed results show how graphene nanomesh size influences the  $I$ - $V$  characteristics of transistor.

Given the simplicity and the reduced computation time of the approach, these results can lead to perform parametric analyses, optimizations and characterization of graphene nano-transistor when applied in larger-scale circuits.

# Chapter 1. Introduction

In this chapter, we give some introductory notions about the interests of graphene, its application in electronics, and the modelling tools to predict its electronic behaviour in nanotransistors. Namely, the tight binding model is introduced and discussed, leading to compute the conduction bands of graphene and its properties. A brief review of modelling methods for transistors is also given, together with their fields of application. A semi-analytic method for carbon-based nanotransistors is then described with some details, being the approach chosen for the study of the devices analysed in the following chapters.

## 1.1 Research background

Materials can be classified into three categories with respect to their electronic properties, according to the shape of energy band around the Fermi level (i.e., the approximate energy level of charged carriers). Conductive materials (such as copper, iron, etc.) enable the conduction of electric currents since an energy level is present around the Fermi level. This band offers the carriers free degrees of states to create a current flow. Insulator materials (such as ceramics, plastics, etc.) do not allow electric current to flow, since the Fermi level falls in an energy gap and no close available energy bands allows the conduction of current. Finally, semiconductor materials (such as Germanium, Silicium, etc.) can conduct current if some external energy is provided to carriers in order to overcome the small energy gap around the zero-Kelvin Fermi level. Figure 1.1 shows different band gaps in metals, isolators and semiconductors. Semiconductor materials were discovered in the 19th century; however it did not arouse researcher attention at that time. Due to the development of radar technology in World War II and electronics, semiconductor materials played a fundamental role in technology advancements and stimulated a considerable amount of research activities.

Semiconductor materials are in fact of crucial importance for today's electronic technology as the development of integrated circuit is based on it. Figure 1.2 shows some important steps of the development of semiconductor devices going from the discovery of semiconductor properties to the invention of transistor and the development of modern electronic circuits. Vacuum tubes were once the basic components of electronic devices for

signal amplifications and mixing. However, their large volume and fragility would hinder the development of miniaturized and embedded circuits. In this context, the emergence of semiconductor transistors was the greatest breakthrough leading to electronic devices of smaller size, lower cost, reduced power-consumption and heat dissipation. The appearance of the first transistor in 1947 at Bell Labs marked the beginning of the electronic era [1]. In 1958, integrated circuits were invented by Jack Kilby, when it became possible to place many transistors on the same chip. In 1965 Gordon Moore, one of Intel's founders, observed that the number of components in an integrated circuit is doubled every 18-24 months while the overall price of the circuit being constant [2]. This was later acknowledged as the well-known Moore's Law, describing the evolution of the electronic technology of the rest of the century.

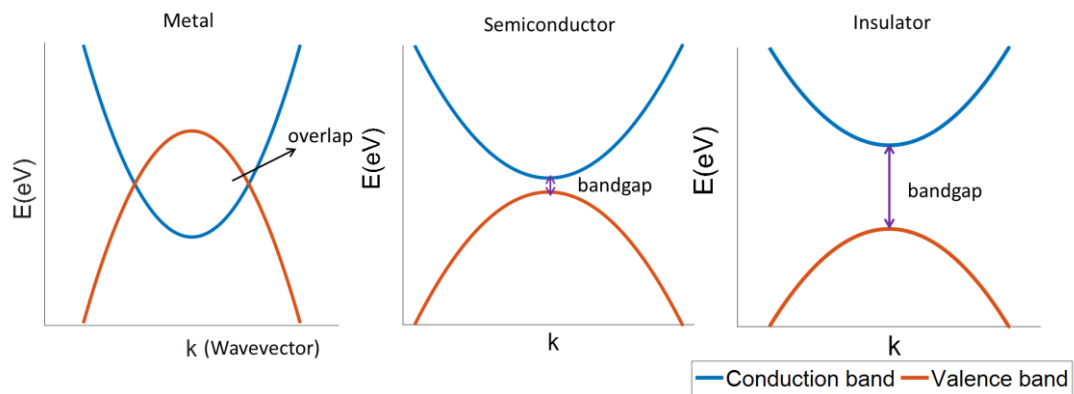


Figure 1.1: Bandgap of different kind materials.

Following Moore's Law, the miniaturization of transistors proceeded at a steady pace in the last decades. Nowadays limitations of bulk MOSFET are arising to short-channel effects that slow down the miniaturization of devices. Effects such as the saturation velocity of charges and the lowering of threshold voltage limit the performance of devices at nano-scale. In this framework, carbon-based nano-transistors have recently attracted a lot of attentions due to their tiny sizes and remarkable electronic properties [3]-[5]. In [3], P. Avouris et al. studied the performance of carbon nanotubes (CNTs) transistors. The electronic characteristics of CNTs transistors (gate length 260 nm) are compared with two silicon devices, proving that CNTs transistors can have superior on-off current ratios and better transconductance than silicon transistors. In [4], R. Martel et al. also presented some experimental data of nanoscale carbon-based transistors. Different electronic characteristics of

carbon-based transistors are compared with 25 nm Si FETs and 100 nm Si FETs respectively, the improved performance of carbon-based transistors demonstrated that they may be competitive with Si FETs [4]. Moreover, even if great progresses have been achieved for the realization of Si-based devices, their gate length and gate insulator thickness cannot be continuously scaled. The unique electronic properties of carbon based material offer the possibility to overcome these limitation and achieve further device miniaturization.

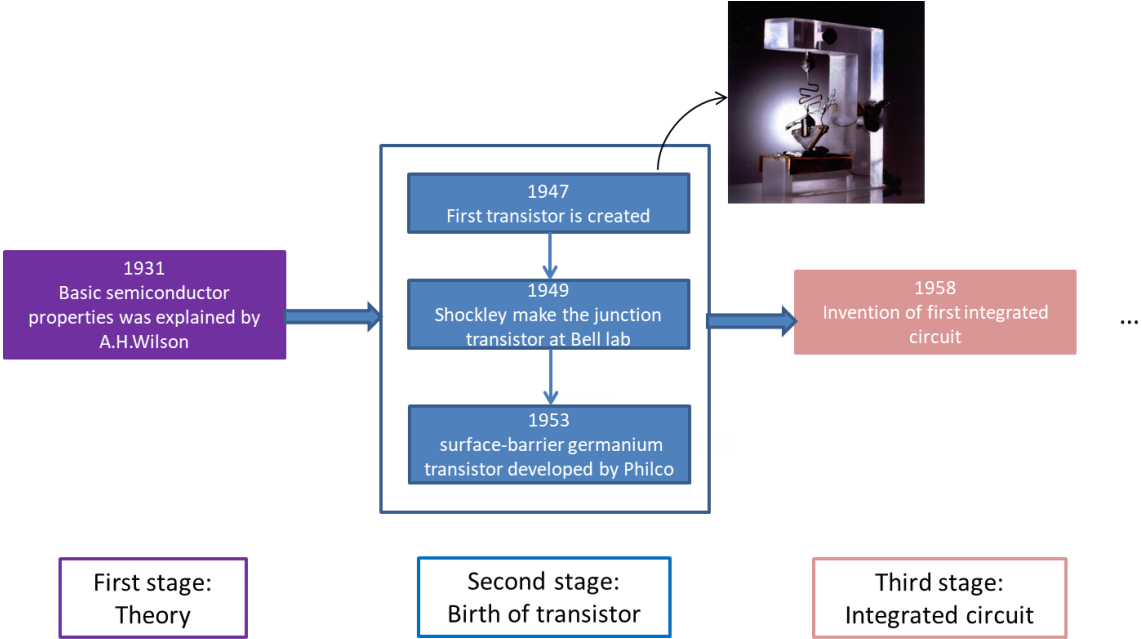


Figure 1.2: Events during the development of semiconductor devices.

The design of novel electronic devices for diverse applications, such as biomedical, security or leisure, must face several challenges, notably in terms of flexibility, biocompatibility, and low power consumption. In this framework, thanks to the electric properties of graphene, graphene-based transistors are currently regarded as an attractive solution of these issues.

There are already several cases of graphene implementation in industry engineering (see Figure 1.3). Graphene can be used e.g. as the coating material of touch screens for telephones and computers [6]. If we apply graphene in our computers, the new material will make them much fast [7]. Graphene-based patch can also be used for monitoring possibly treats diabetes [8]. It can maintain healthy blood glucose levels in people through measuring the sugar in sweat and delivering necessary diabetes drugs through the skin.

Furthermore, electronic properties of graphene are not the only advantages of this material. Due to mechanical robustness and flexibility, carbon-based transistors are natural candidates for different electronics (see Figure 1.3 and Figure 1.4).

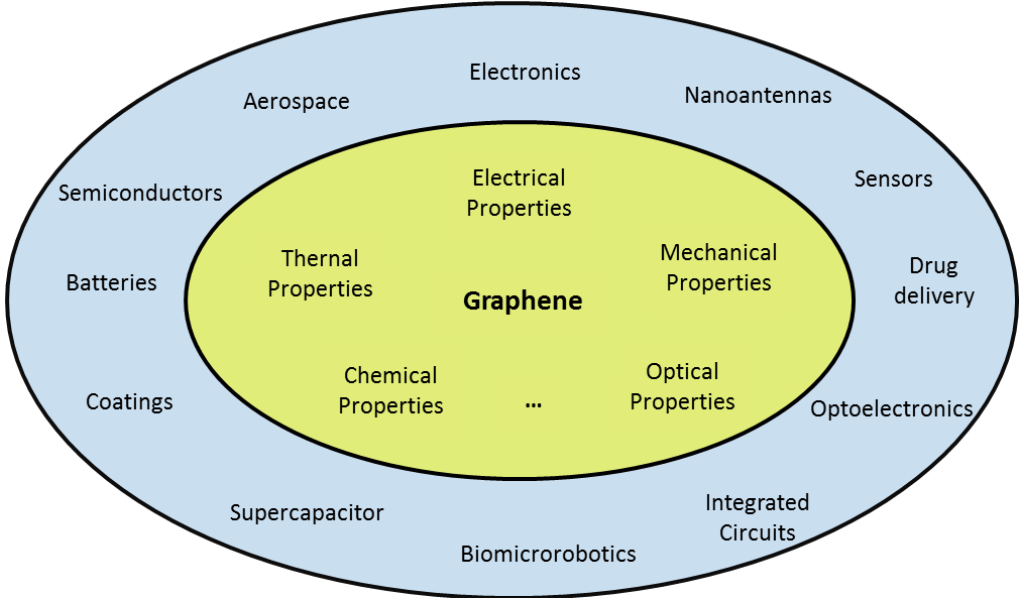


Figure 1.3: Properties of graphene and its potential applications.



(a)

(b)

Figure 1.4: (a) Graphene-treated nanowires could replace current touchscreen technology

(b) A graphene patch that monitors and possibly treats diabetes [9][10].

## 1.2 Electronic properties of a graphene sheet

Graphene is a two-dimensional material consisting of hexagonal carbon atoms arranged in honeycomb lattice (see Figure 1.5) [11]-[12]. More specifically, it is an allotrope of carbon in the structure with a molecule bond length of 0.142 nm. Since mechanical exfoliation of monolayer graphene was first reported in 2004 by Andre Geim and Konstantin Novoselov [13], interest in this material has increased dramatically. Compared with other materials, graphene has many excellent properties, which are shown in Table 1.1.

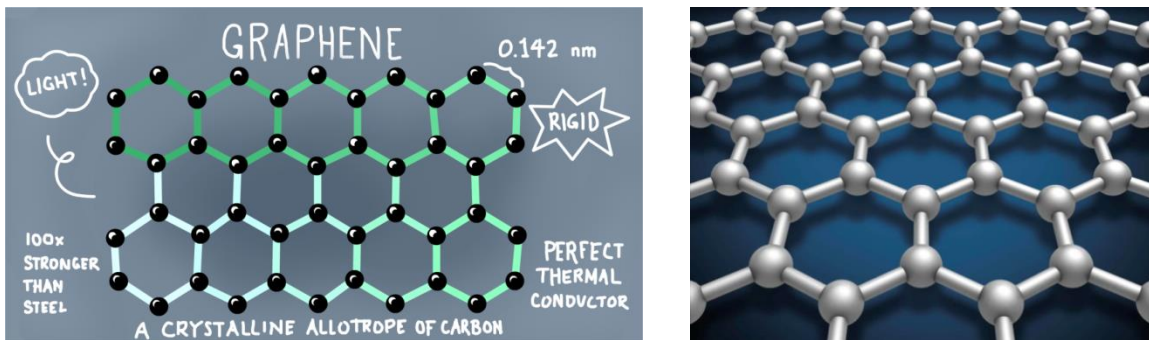


Figure 1.5: Shape and characteristics of graphene [14].

Table 1.1: List of typical graphene properties.

Graphene Property	Numerical Value	Comparison with other material
Tensile Strength	~130 GPa [15]	steel ~550 MPa [17]
Young's Modulus	~1 TPa [15]	Bronze ~ 96–120 GPa [18]
Thermal Conductivity	~5000 Wm <sup>-1</sup> K <sup>-1</sup> [16]	Diamond: ~ 1000 Wm <sup>-1</sup> K <sup>-1</sup> [19] Copper: ~ 401 Wm <sup>-1</sup> K <sup>-1</sup> [19]
Electron mobility	excess of cm <sup>2</sup> /(V·s) [11]	Si ~ 1400 cm <sup>2</sup> /(V·s) [20]

The graphene primitive cell is shown in Figure 1.6, where each blue point is a carbon atom, and green lines join adjacent atoms. In order to develop an analytical expression for the

energy band structure of graphene the time-independent Schrödinger's equation should be solved,

$$H\psi(\mathbf{k}, r) = E(\mathbf{k})\psi(\mathbf{k}, r) \quad (1.1)$$

where  $\psi$  is the electron wavefunction,  $H$  is the Hamiltonian operator which operates on the wavefunction and the energy  $E$  is its eigenvalue.  $\mathbf{k} = k_x \mathbf{x} + k_y \mathbf{y}$  is the wavefunction momentum, also called reciprocal vector. Models for the computation of energy bands of graphene structures can be based on first-principle or on tight binding approaches. In both cases we aim at solving the Schrödinger equation.

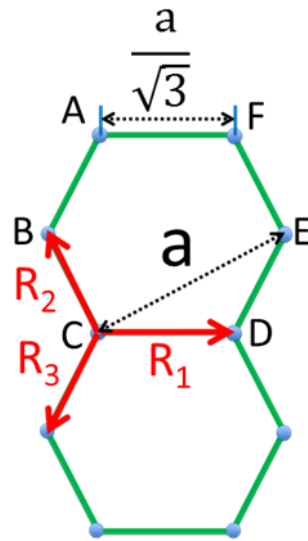


Figure 1.6: Schematic illustration of a graphene cell.

First principle models aim at solving the Schrödinger equation by using only physical fundamental constants and the atomic composition of the material as input. They allow the computation of several quantities of interest in solid-state physics and chemistry, namely the electron density, energy levels, and nuclei positions, leading in our case to a precise characterization of electric features of nano-devices. Due to the extreme complexity of the calculation (large number of unknowns, of variables of wave functions, non-linear nature of the problem and iterative solutions required, etc.) many ab-initio approaches exists, depending on the specific assumptions used to simplify the problem under study. Among the best known is the Hartree–Fock (HF) method and its variations. It uses the so-called Born-Oppenheimer approximation, consisting in a two-step solution of the time-independent Schrödinger

equation separately for the electronic coordinates (with an “electronic” Hamiltonian) and for the nuclei coordinates (by including the nuclear kinetic energy). The unknown wave function is expressed as a sum of basis functions (“atomic orbitals”), chosen to approximate a complete basis in order to represent at the best the wave function. The Hartree-Fock *ab-initio* method is certainly among the most accurate and flexible modeling for a vast class of atomic structures. It allows getting accurate results at high energies, in the presence of irregular shapes, defects, loss of symmetry. However, due to the complexity of the problem and the number of different particle interactions, *ab-initio* calculation time becomes long as the size of the domain increases and prevents the simulation and the optimization of large devices. Thanks to the symmetry of the graphene lattice, nano-electronic applications presented in this thesis can be often modeled, at least partially, with simplified methods leading to fairly accurate results.

- Tight binding model

Tight binding theory can overcome limitations of *ab-initio* simulations and even give analytic closed-form results, which can help us gain a physical insight about the device operation. It leads to the electronic structure of the material under study, by solving also in this case the time-independent Schrödinger’s equation for the energy dispersion band structure.

The tight binding model is a method of calculating the electronic band structure by using a set of approximate wave functions which are based on superposition of isolated atomic wave functions. This model is different from nearly-free electron model. For nearly-free electron model, interactions between electrons are ignored and assume the electrons in the crystal only have weak Coulomb attraction from respective nucleus [12]. On the contrary, in tight binding model we assume that the atom has a strong binding effect on electrons. Electrons near the atom are mainly affected by the potential field due to the atom, while the effect of other atoms is regarded as a small perturbation.

In order to obtain simple closed-form results, leading to a fast analysis tool, in this thesis we choose to use a tight binding model for solving the electronic structure of deformed graphene. Furthermore, the method can be used also to calculate the modification of energy bands due to small deformations of the graphene lattice. In the following the main results

obtained with the tight binding approach are summarized. More details and calculations about the effect of deformations will be presented in Chapter 2.

A tight binding model can be considered to solve (1.1), consisting in retaining only a finite number of mutual interactions among atoms in the Hamiltonian  $H$  [12]. If only the closest atoms interact, a so-called nearest-neighbor approach is obtained. In this case, the spectral Hamiltonian becomes:

$$H(\mathbf{k}) = V \left( e^{-jk \cdot \mathbf{R}_1} + e^{-jk \cdot \mathbf{R}_2} + e^{-jk \cdot \mathbf{R}_3} \right) \quad (1.2)$$

with the tight-binding hopping parameter  $V=2.7$  eV, experimentally determined, describes the energy related to an electron exchange between adjacent sites.  $V$  is also referred to as the nearest neighbor overlap energy, the hopping or transfer energy, or the carbon-carbon interaction energy [12]. Of course the symmetry of the lattice grants that the value of  $V$  is the same for all the possible exchanges with each of the three nearest neighbors.

In the nearest-neighbor approach, graphene energy bands can be computed from equation (1.2), [12].

$$E^2(\mathbf{k}) = V^2 \left( e^{-jk \cdot \mathbf{R}_1} + e^{-jk \cdot \mathbf{R}_2} + e^{-jk \cdot \mathbf{R}_3} \right) \left( e^{jk \cdot \mathbf{R}_1} + e^{jk \cdot \mathbf{R}_2} + e^{jk \cdot \mathbf{R}_3} \right) \quad (1.3)$$

The hexagonal symmetry of the lattice makes it simple to express the vectors  $\mathbf{R}_1$ ,  $\mathbf{R}_2$ , and  $\mathbf{R}_3$  as a function of the inter-atomic distance  $a = 2.46$  Å (see Figure 1.6).

$$\begin{aligned} \mathbf{R}_1 &= \left( \frac{a}{\sqrt{3}}, 0 \right) \\ \mathbf{R}_2 &= \left( -\frac{a}{2\sqrt{3}}, -\frac{a}{2} \right) \\ \mathbf{R}_3 &= \left( -\frac{a}{2\sqrt{3}}, \frac{a}{2} \right) \end{aligned} \quad (1.4)$$

A simple replacement of (1.4) in (1.3) leads to the final expression:

$$E(k_x, k_y) = \pm V \sqrt{1 + 4 \cos\left(\frac{\sqrt{3}a}{2} k_x\right) \cos\left(\frac{a}{2} k_y\right) + 4 \cos^2\left(\frac{a}{2} k_y\right)} \quad (1.5)$$

Figure 1.7 shows the bi-dimensional Brillouin diagram obtained with the nearest-neighbor tight-binding approach (1.5). The upper half dispersion is the conduction band and the lower half dispersion is the valence band. The K points, also called Dirac points, are the point in the  $k_x k_y$  spectral plane where the conduction band and valence bands touch each others exhibiting a locally linear behavior. Figure 1.8 shows the typical Dirac cone at the points K, where a locally linear dispersion is found. In Figure 1.8, the Dirac cone shows clearly that an infinite graphene sheet exhibits no band gap.

Figure 1.9 shows the comparison of an *ab-initio* and a nearest neighbor tight-binding (NNTB) model for graphene energy dispersion. The *ab-initio* model is of course more accurate than NNTB method. From Figure 1.9, we can observe subtle differences for higher energies. However, behavior of electrons around Dirac points is the most relevant to study transport properties in nano-transistors. Since *ab-initio* model and NNTB model show good agreement at low energies, tight binding method are currently used for these applications mainly due to the reduced computation time and ease of implementation, even if not being as accurate as *ab-initio* models.

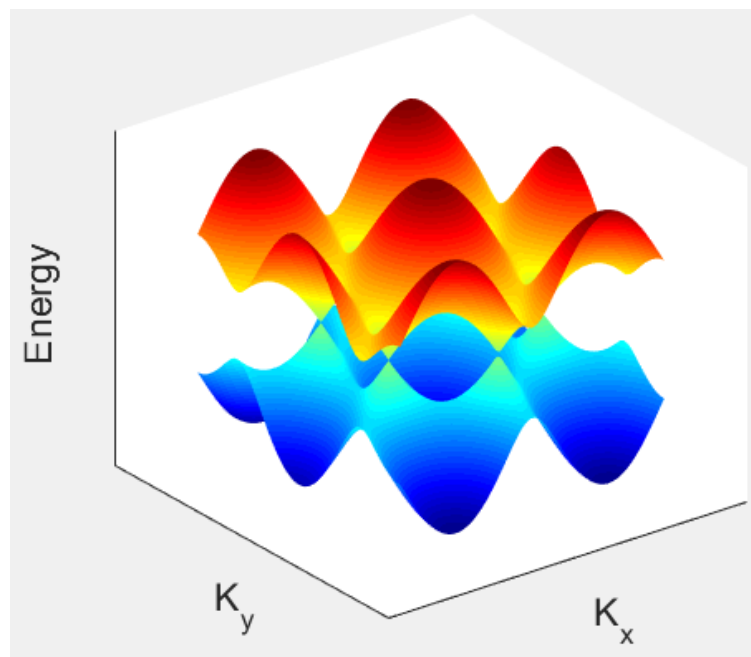


Figure 1.7: The nearest-neighbor tight-binding band structure of graphene.

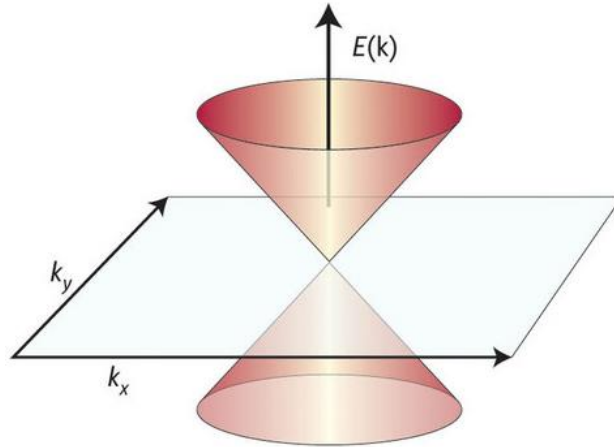


Figure 1.8: The linear energy dispersion of graphene at the K-point.

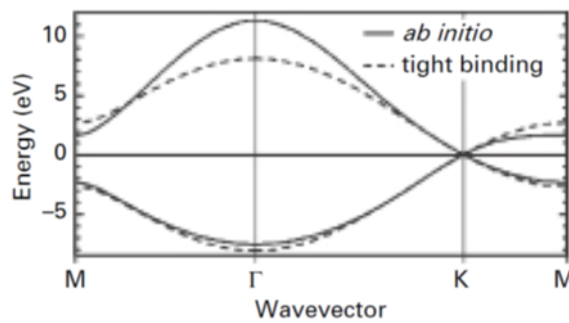


Figure 1.9: Comparison of *ab-initio* and NNTB model for energy dispersions calculation [12].

### 1.3 Energy bands of graphene nanoribbons

Graphene nanoribbons are narrow rectangles made from graphene sheets. Two main types of graphene nanoribbons can be considered, the armchair GNRs (aGNRs) and zigzag GNRs (zGNRs). The difference among them is that aGNRs has an armchair cross-section at its edges, while zGNRs has a zigzag cross-section at its edges [12]. An aGNR can be obtained by cutting a graphene sheet along a given direction (see Figure 1.10). Since the resulting strip lacks the translational symmetry along one direction (its width), no simple closed forms can be obtained for its energy bands as in the infinite-graphene case. However, if an ideal Dirichlet condition is enforced on the wavefunction at the opposite boundaries along the

width  $w = (N - 1)a/2$  of aGNR, where  $N$  is the number of tightly bound atoms in the direction of the ribbon width ( $y$  in Figure 1.10),

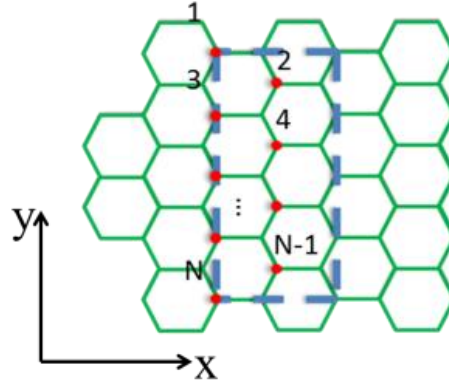


Figure 1.10: Armchair graphene nanoribbon.

$$\psi\left(y = -\frac{a}{2}\right) = \psi\left(y = w + \frac{a}{2}\right) = 0 \quad (1.6)$$

simple conditions can be derived on the  $k_y$  wavenumber for aGNR:

$$(w + a)k_{y,\alpha} = \alpha\pi \quad (1.7)$$

$$k_{y,\alpha} = \frac{\alpha\pi}{w + a} = \frac{\alpha\pi}{\frac{N-1}{2}a + a} = \frac{2\alpha\pi}{(N+1)a} \quad (1.8)$$

where  $\alpha = 1, \dots, N$ .

Once the discretized values of  $k_{y,\alpha}$  are replaced in the energy (1.5), the sub-band structure of the nanoribbon is obtained:

$$E_\alpha(k_x) = \pm V \sqrt{1 + 4 \cos \frac{\sqrt{3}ak_x}{2} A_\alpha + 4A_\alpha^2} \quad (1.9)$$

where

$$A_\alpha = \cos\left(\frac{\pi\alpha}{N+1}\right)$$

$$\alpha = 1, \dots, N$$

## 1.4 Review of modeling methods for nano-transistors

The electronic and mechanical properties of graphene are the reason of the interest in graphene-based devices. The behaviors are of course related to the energy bands graphene-base structures, but also to other factors like deformation features, temperature of the environment, geometric and physical parameters of the device. Unfortunately, accuracy issues of current models for transistors are already arising in connection to the progressive reduction of the scale of MOSFET devices. This complexity motivates the research of numerical models efficient and at the same time accurate. Different models are briefly reviewed here, and more details will be given about the model selected to study the transistors in the following chapters.

The drift-diffusion model is the most common semi-classical models of micron-scale semiconductor devices [21][22]. The current flowing through the device is the sum of a drift term and a diffusion term both for electrons and holes. The success of the drift diffusion model is due to its efficiency, simplicity, and flexibility on different kind of meshes for arbitrary geometries. However, this model does not take into account quantum effects arising in nano-scale devices, such as hot carriers and band discretization due to spatial-confinement effects [23]. Different modifications have been proposed in order to introduce suitable corrections to these limitations.

Monte Carlo algorithms are the most reliable and established approaches, extensively used to simulate devices under semi-classical regimes. They are based on the simulation of a large number of sample cases (particles motion through the device) whose trajectory is computed with semi-classic approximations. Scattering phenomena intervals of free-flight (time intervals between scattering events) are computed with suitable statistics [24]. The scattering effects and velocity spectra are also studied for nano-scaled MOSFET (which channel lengths are 15nm and 25nm) by using Monte Carlo simulation in [25]. Recent works have shown how to successfully include quantum effects due to thin films (by means of sub-band quantization corrections) and short-channels effects (by including quantum non-local effects in the charge density evolution) [26].

Hydrodynamic models are derived by applying the moment technique to the Boltzmann transport equation. The propagations of electrons and holes in a semiconductor

device is here simulated as the flow of a charged compressible fluid [27][28]. This allows for considering the effect of hot carriers, which is missing in the drift-diffusion model, and leads to accurate results for devices of size larger than  $0.05 \mu\text{m}$ . Also in this case, quantum corrections to the evolution of the charge distribution have been proposed to treat smaller devices [29]. This approach is much faster than Monte Carlo ones, but can fail at very small scale, where Monte Carlo is still reliable. Thoma [28] proposed a generalized hydrodynamic model, where formulas depending on temperature only are applied.

In order to reduce the computation time and obtain simplified models to be used in circuit design and optimization, the intensive research on graphene field-effect transistors (GFET) stimulated within the past decades several models for better understanding characteristics of these devices and to reduce the computation time of rigorous approaches.

#### 1.4.1 Carrier transport model in GFET

In [30], an analytical model for GFET is presented (see Figure 1.11). In this structure, the substrate is highly conducting and serving as the back gate, while the top gate controls the current. Thermionic transport is described for this kind of GEFT. Potential distribution in the channel and thermionic current are calculated accordingly by using this analytical model.

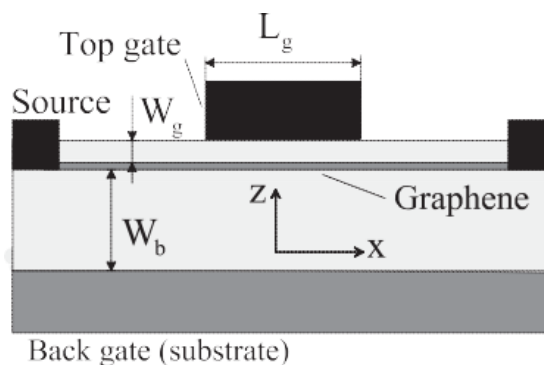


Figure 1.11: Schematic view of GFET structure studied by V. Ryzhii, M. Ryzhii, and T. Otsuji [30].

In [31] first principle approach is used to study the behavior of GFET, thus obtaining thermal, electrostatics, and electrodynamic quantities, channel current and transfer characteristics. Based on the physical model in [31], a small-signal model was proposed in [32]. This small-signal model is also based on first principle and the carrier transport in the

channel is studied by drift-diffusion model. S. Thiele and F. Schwierz proposed a simple model for calculating DC behavior of GFET [33]. Modeling results like transfer characteristics and output characteristics are successfully compared with experimental data.

In [34] the carrier transport is studied with a drift-diffusion perspective, for both single-layer and multiple-layer graphene. In [35] the non-equilibrium Green's function (NEGF) technique is used to solve the Dirac equation for GFET, and the carrier transport of double-gate GFET is investigated.

### 1.4.2 Analytical models for GFET

In the last decade, some analytical models for GFET have also been proposed. The authors of [36] describe the design of top gate GFET [36] (as Figure 1.12 shows). In their research, the channel material is zero-bandgap graphene. Although the utilization of zero-bandgap graphene limits the on-off current ratio, the results showed the possibility of applying graphene for radio frequency circuit.

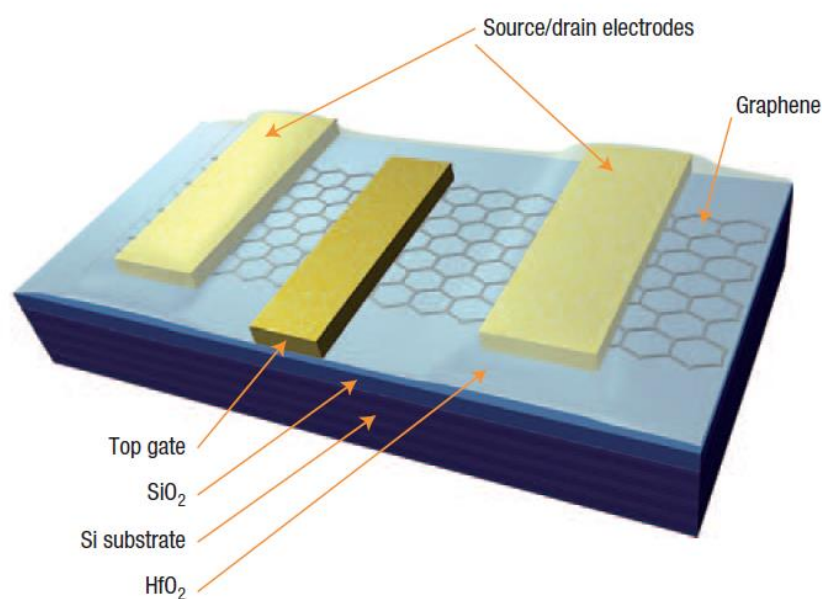


Figure 1.12: Top gate GFET structure studied by I. Meric [36].

The carrier concentration  $n$  is at first computed, and the quantum capacitance is calculated as:

$$C_q = \sqrt{(n/\pi)}e^2 / v_F \hbar \quad (1.10)$$

where  $v_F$  is the Fermi velocity. The current in the channel can then be derived as:

$$I_d = \frac{W}{L} \int_0^L en(x)v_{drift}(x)dx \quad (1.11)$$

where  $W$  is the channel width,  $L$  is the channel length,  $v_{drift}(x)$  is the carrier drift velocity. The carrier drift velocity can be calculated by using a velocity saturation model:

$$v_{drift}(x) = \frac{\mu E}{1 + \mu E / v_{sat}} \quad (1.12)$$

where  $v_{sat}$  is the saturation velocity of the carriers. A considerable amount of later research is based on [36]. In [37] the gapless graphene is also used as channel material. Compared with [36], stable saturation is obtained.

Quantum capacitance, channel charge,  $I$ - $V$  characteristics, the small signal parameter and cut-off frequency are all calculated in this model. These results are also validated with experimental data from long-channel GFETs (channel length larger than 1  $\mu\text{m}$ ).

A new compact model [38] is proposed based on the quasi-analytical model in [37] and verified by using measurements from the literature. The authors of [39] proposed a compact model suitable for short-channel GFETs (the channel length is 240 nm) and based on the concept of “virtual source”. This GFET virtual source model allows to study the carrier transport in GFETs and is also described in H. Wang’s model [39]. The derived  $I$ - $V$  characteristics are compared with experiment data showing a good agreement.

In [40] and [41], a GFET model is presented for radio frequency applications, based on drift-diffusion theory with saturation velocity effects. Drain current, charge, and capacitance of GFET are there discussed. In [42], a semi-empirical model is shown for single layer zero-bandgap graphene. The current can be calculated by using carrier density, the carrier velocity, the channel length and the channel width. The carrier density is modeled by semi-empirical charge-voltage relation and carrier drift velocity is obtained by a velocity

saturation model. Compared with physical models, this semi-empirical model gives accurate drain and source contact resistances and can provide acceptable accuracy with considerably reduced time.

In [43], models for both monolayer graphene and bilayer graphene based on the results in [36][37] are presented. In [44] a compact model for GFET in the quantum capacitance limit based on the drift-diffusion model [44]. The results of [36] were also used in [45] and [46] to achieve a scalable compact model based on quasi-analytical physics, where the charge distribution computation is improved by considering the specific graphene density of states. This approach has inspired a number of following papers such as [47]. In [48], a circuit-level model for GFET is proposed which channel being either a multilayer graphene involving an arbitrary number of layers. The multilayer geometry is described with the introduction of a novel interlayer capacitance leading to an accurate calculation of the channel surface potential and the channel resistance. In [49] an ambipolar-virtual-source model for nanoscale GFET is presented, including two separate virtual sources for electrons based on drift-diffusion equation.

These models are mainly focused on the use of graphene in FET and they are suitable for analogue and radio frequency circuit without considering band gap. However, the lack of bandgap limits the on-off current ratio. Different methods to tune the band gap of graphene for FET have been proposed for practical application. The most appealing approaches, compatible with the realization of fully planar nanotransistors, is the cutting of graphene sheets into thin nanoribbons and the fabrication of nanomeshes by removing atoms along a periodic pattern. Graphene nanoribbon exhibits a band gap directly related to their width, and equivalently to the number of atoms along their transverse (and shorter) dimension. The bandgap of nanomesh is also related with its geometric features, namely the shape and distributions of the holes.

## **1.5 Modelling methods used in this thesis**

In this section, we will introduce the two methods used in this Thesis to model the nano-transistors described later. In relation to the size of the transistors chosen, we aim at

analyzing the electronic characteristics of both ballistic and quasi-ballistic GFET. This means that the length of the device is smaller than the mean free path of graphene, so that charges move through the channel without experiencing any scattering (ballistic regime) or encountering a limited amount of scattering (partially ballistic regime).

The objective of the model is the computation of the current under different voltage excitations. However, the current can only be computed once the potential distribution along the channel  $\phi(x)$  is known ( $x$  being a linear coordinate along the channel). This potential is a quantity varying along the channel in the case of quasi-ballistic transistor, or a constant along the channel in the case of ballistic transistor. In order to determine the potential, the charge distribution along the channel should be computed with two different approaches at different scales, and a multiscale coupling between them is performed. We have then a macro-model and a micro-model. In order to obtain a coherent description of charge density, an equality is enforced between the charges computed with both models: this gives an equation leading to the numerical determination of the channel potential  $\phi(x)$ . This is described in Figure 1.13.

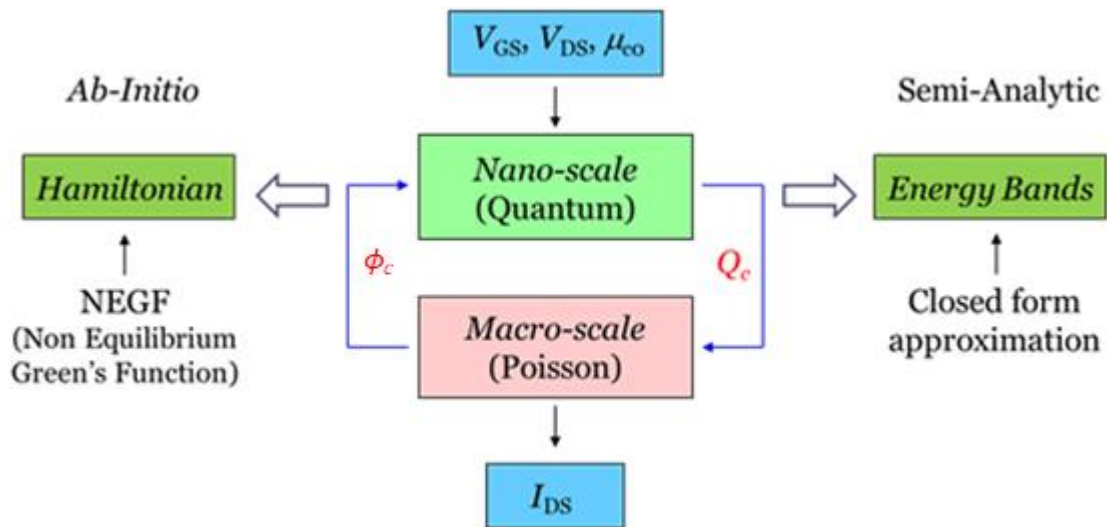


Figure 1.13: Diagram used in both models to compute source-drain current.

More specifically, the macro-model computes the charge distribution in the channel through an electrostatic analysis of the device. Its mathematical formulation is done through Poisson equation, but for canonical geometries as those studied here, analytic simplified

expressions for the capacitances between contacts can be used in order to avoid a full numerical solution of the Poisson equation.

In fact, a macroscopic expression for the charge, expressed through equivalent capacitances  $C_g$ ,  $C_s$  and  $C_d$  can be written straightforwardly as:

$$Q_{macro}[\phi_c(x)] = - \sum_{i=g,s,d} C_i [V_i - V_{FB,i} - \phi_c(x)] \quad (1.13)$$

where  $V_g$ ,  $V_s$ ,  $V_d$  are the voltage of gate, source and drain, respectively, and  $V_{FB,i}$  are the relevant flatband voltages.

The gate capacitance per unit area can be calculated as [50]:

$$C_g = \epsilon_r \epsilon_0 \left\{ \frac{\pi}{w \ln \left[ 6 \left( \frac{t}{w} + 1 \right) \right]} + \frac{1}{t} \right\} \quad (1.14)$$

where  $t$  is the thickness of the substrate ( $\text{SiO}_2$  in the following chapters)  $\epsilon_r$  is its relative permittivity, and  $\epsilon_0$  is the permittivity of vacuum. Note that this expression is quite different from the simple capacitance of a large parallel plate system, since fringing-field corrections are relevant at this length scale.

The micro-model computes the charge in the channel by means of a quantum approach, and its mathematical formulation is done by means of the Schrödinger equation. This micro-scale problem is formulated in two different ways. A rigorous but time-consuming *ab-initio* approach is chosen in order to obtain results to be used as a reference. However, in order to have a faster method useful for the parametric analysis and optimization of electronic devices, we use also a semi-analytic approach whose results will be compared with the *ab-initio* ones.

### 1.5.1 Micromodel: the Non-equilibrium Green's function

A very accurate *ab-initio* method often used for the study of physical properties of materials and more specifically the behavior of nano-transistors is the Non-equilibrium Green's function (NEGF). The NEGF approach is a dynamical formulation based on the solution of Schrödinger equation, solving for the energy bands of materials by describing the

interaction among atoms through proper atomic orbitals for the coupling between carbon atoms, and between the source/drain and the graphene [51]. Despite its accuracy and flexibility, this method is time consuming if compared with the analytic method described in the following paragraph 1.5.2. For this reason, the NEFG<sup>1</sup> method will be used in this Thesis to obtain reference results with the aim of validating the analytic method proposed later.

The NEFG method performs the numerical solution of Schrödinger equation in the Laplace domain, thus keeping a full information on the dynamic properties of the device. An extensive treatment of NEGF can be found in [51][52]; here we give a few definitions necessary to formulate our problem.

The current of graphene nanoribbon-based FET can be calculated by the following equation [53]:

$$I = \frac{2q}{\hbar\pi} \int \text{trace} \left[ \left( \Sigma_S - \Sigma_S^* \right) G(\phi_c) \left( \Sigma_D - \Sigma_D^* \right) G(\phi_c)^* \right] (f_S - f_D) dE \quad (1.15)$$

where  $\Sigma_S$  and  $\Sigma_D$  are operators describing the interactions with  $S$  and  $D$  contacts, respectively,  $f_S$  and  $f_D$  are Fermi distribution at the  $S$  and  $D$  contacts, respectively,  $G(\phi_c)$  is the Green's function,  $\phi_c$  is the channel potential to be determined with the multiscale approach described above.

Every atom in the lattice can be indexed by a couple of integers, and the interaction between sites by the indices  $mn, ij$ . To apply (1.15) to a graphene channel, the equation of motion must be enforced for the Green's function:

$$i\partial_t G_{mn,ij}^r(t,t') = \delta(t-t') \delta_{mn,ij} - i\theta(t-t') \{ [c_{mn}, H], c_{ij}^\dagger \} \quad (1.16)$$

and the operator  $H$  in (1.16) describing the electronic interactions is:

---

<sup>1</sup> The method has been developed by Dr. Fernando ZANELLA, at the time PHD student at the Universidad Federal do Paraná, Brasil, during two visits at Sorbonne in 2016 and 2017.

$$H_{i,j} = \frac{\hbar^2}{2m_e} \nabla^2 + \frac{q^2 Z_c}{4\pi\epsilon_0} \left( \frac{1}{r_i - R_j + a_0} \right) + \mu_c \quad (1.17)$$

where  $q$  is the electron charge and  $\hbar$  is the reduced Plank's constant. The first term in (1.17) is the kinetic energy of each electron, with  $m_e$  being the free electron mass. The second term is the Coulomb potential between an electron and a carbon nucleus, with  $Z_c$  the effective atomic number and  $\epsilon_0$  the vacuum permittivity;  $r_i - R_j$  is the distance between an electron and a nucleus, and  $a_0$  is the maximum radius of a carbon atom, significant when  $i = j$ . The last term is the localized channel potential that must be found by coupling the quantum-mechanics equations with the electrostatic problem (Poisson equation). The Green's function can be obtained by solving the Schrödinger equation in Laplace domain:

$$G(\phi_c) = \frac{1}{E - j\eta - H - \Sigma_S - \Sigma_D} \quad (1.18)$$

where  $E$  is the energy, and  $\eta$  is an infinitesimal number necessary to guarantee convergence. To find the matrix form of  $\mathbf{H}$  we project (1.17) in a  $\pi$  orbital basis for the channel given by

$$\varphi_{i,j}(r) = \sqrt{\frac{\lambda^5}{\pi}} \cos(\theta) e^{-\lambda r} \quad (1.19)$$

where  $\lambda = 2.18$  is a constant enforcing orthonormality. For the contacts, we consider a coupling between a carbon atom and gold atom.

We should notice this method is very accurate, but also time consuming and not suitable for fast analyses of circuits composed of several devices or optimization of devices with respect to several parameters. The method requires computational is related in the first place to the great number of interactions among orbitals considered.

### 1.5.2 Micromodel: the Semi-analytic multiscale approach

Therefore, in this thesis, we choose to apply ballistic transport model and partially ballistic transport model for analyzing the electronic characteristics of GFET. This means that the length of the device is smaller than the mean free path of graphene, so that charges move through the channel without experiencing any scattering (ballistic regime) or encountering a limited amount of scattering (partially ballistic regime).

An appealing model for nano-scale transistor in ballistic regimes (which can be easily extended to the semi-ballistic [54][55]) has been proposed in [51][56], based on the analytic calculation of energy bands and the density of states of nanoribbons. The current flowing in the transistor can be calculated by using a Landauer–Büttiker approach [51]:

$$I_i(\phi_c) = \frac{q}{\pi\hbar} \sum_{\alpha} \int_0^{E^{\max} - E(0)} \frac{T_s T_d}{T^*} \left[ f(\eta_{\alpha,s}^i) - f(\eta_{\alpha,d}^i) \right] dE \quad (1.20)$$

where  $T_s$  and  $T_d$  are the transmission coefficient of charges through Schottky barrier at the source and drain contacts, respectively, and become equal to one in the case of Ohmic contact. Their computation is detailed in next paragraph 1.6. The factor  $T^*$  is given by

$$T^* = T_s + T_d - T_s T_d$$

In equation (1.20),  $i = e, h$  stays for electrons and holes, and the Fermi-Dirac distribution  $f$  is integrated:

$$f(\eta) = \frac{1}{1 + e^{\eta}} \quad (1.21)$$

$$\eta_{\alpha,s(d)}^e = \frac{E - q\phi_c(x) + E_{\alpha}(0) - \mu_{s(d)}}{k_b T} \quad (1.22)$$

$$\eta_{\alpha,s(d)}^h = -\eta_{\alpha,s(d)}^e \quad (1.23)$$

$\mu_s$  and  $\mu_d$  are the Fermi levels of source and drain respectively,  $E$  is the kinetic energy (to be integrated in (1.20)) and  $\phi_c(x)$  is the surface potential, i.e., the potential along the channel.

As said above, its dependency on  $x$ , a coordinate along the channel length, cannot be neglected in the case of partially ballistic conduction.  $k_b$  is the Boltzmann's constant and  $T$  is the temperature. The total current is given by:

$$I = I_e - I_h \quad (1.24)$$

However, before computing (1.20) and (1.24), the surface potential  $\phi_c$  must be determined first. The surface potential  $\phi_c$  can be determined by imposing a consistency relation between the mobile charges in the channel  $Q_{micro}(\phi_c)$ , computed with a quantum-mechanical approach, and  $Q_{macro}(\phi_c)$ , computed through a macroscopic electrostatic model.

$Q_{micro}(\phi_c)$  can be expressed as an integral of the Fermi-Dirac distributions over all the energy bands:

$$\frac{Q_{micro}^{e/h}(\phi_c)}{q} = \sum_{\alpha} \int_0^{E^{max} - E(0)} D_{\alpha}(E) \left\{ \frac{T_s(2-T_d)}{T^*} f(\eta_{\alpha,s}^i) + \frac{T_d(2-T_s)}{T^*} f(\eta_{\alpha,d}^i) \right\} dE \quad (1.25)$$

$$Q_{micro}(\phi_c) = Q_{micro}^h(\phi_c) - Q_{micro}^e(\phi_c) \quad (1.26)$$

where the sum over  $\alpha$  is a sum over the different energy bands (only the lower bands are usually significant in this computation).  $D_{\alpha}(E)$  is the *density of states* of the  $\alpha$ th energy band as a function of the kinetic energy  $E$ .

## 1.6 Approximated quantities describing nanoribbon energy-bands

As shown in (1.25), the possibility to describe in an analytic form the energy bands of the channel material (graphene-based material in this case) is crucial to obtain a simple expression for  $D_{\alpha}(E)$  and easily calculate the relevant integrals. This is possible, as described in the near-neighbor tight-binding approach in Sec. 1.3. Starting from the analytic expressions for the energy bands we can perform first-order approximations in the cos function for small

$$k_x \cos \frac{\sqrt{3}ak_x}{2} \cong 1 - \frac{1}{2} \frac{3a^2}{4} k_x^2, \text{ we can write}$$

$$\begin{aligned}
E_\alpha(k_x) &\cong E_\alpha^{EM}(k_x) = \pm V \sqrt{1 + 4 \left(1 - \frac{3a^2}{4} k_x^2\right) A_\alpha + 4A_\alpha^2} = \pm V \sqrt{1 - \frac{3}{2} a^2 k_x^2 A_\alpha + 4A_\alpha + 4A_\alpha^2} \\
&= \sqrt{\left[E_\alpha(0)\right]^2 + \frac{\hbar^2 E_\alpha(0) k_x^2}{M_\alpha}}
\end{aligned}$$

with the following definition of an effective mass

$$M_\alpha = -\frac{2}{3} \frac{\hbar^2 [E_\alpha(0)]}{a^2 V^2 A_\alpha} \quad (1.27)$$

If a second approximation is done on the square-root function  $\sqrt{1 + \frac{\hbar^2 k_x^2}{M_\alpha}} \cong 1 + \frac{1}{2} \frac{\hbar^2 k_x^2}{M_\alpha}$

we obtain a parabolic expression:

$$E_\alpha^{EM}(k_x) = E_\alpha(0) \left[ 1 - \frac{1}{2} \frac{\hbar^2 k_x^2}{M_\alpha} \right] \quad (1.28)$$

The definition of  $M_\alpha$  allows different definitions of the density of states  $D_\alpha$  in the presence of deformation, according to the approximation chosen for the energy. Starting from the first-order approximation, we obtain

$$D_\alpha^{EM-d} = \frac{2}{\pi \hbar} \sqrt{\frac{M_\alpha^d}{2 [E_\alpha^d(k) - E_\alpha^d(0)]}} \quad (1.29)$$

while, starting from the second-order approximation, we obtain

$$D_\alpha^{I-d} = \frac{2}{\pi \hbar} \sqrt{\frac{M_\alpha^d}{E_\alpha^d(0)}} \frac{[E_\alpha^d(k)]^2}{\sqrt{[E_\alpha^{I-d}(k)]^2 - [E_\alpha^d(0)]^2}} \quad (1.30)$$

While (1.25) is a less accurate approximation, it allows to compute in close-form the integral in the case of ohmic contacts, and for this reason it is used in [56]. It will be show in next chapter that, in the presence of mechanic deformation, the parabolic expression is not always suitable for the deformed energy bands. The higher-order approximation will be there preferred and the integral (1.25) will be performed numerically.

The importance of the definition of an effective mass is also related to the possibility to achieve a closed-form calculation for the transmittivity  $T(E)$  of a charge through a Schottky contact at the source-graphene and drain-graphene interfaces and the electronic densities of charges in the channel. The final formulas can be used in the following for the relevant computation of charges and currents [56]. WKB approximation (named after physicists Wentzel, Kramers, and Brillouin and developed as a general method of approximating solutions to linear, second-order differential equations) can be used to obtain closed-form transmission coefficients valid under deformation. The transmission coefficient calculated through WKB approximation [56] reads:

$$\ln T(E) = -2 \int_0^{-\lambda \ln\left(\frac{E}{A_s}\right)} \sqrt{\frac{2M_\alpha}{\hbar^2} (A_s e^{-z/\lambda} - E)} dz \quad (1.31)$$

where  $\lambda$  describes the potential distribution along the channel and depends on the device geometry, and  $A_s$  is the height of Schottky barrier at the source (the same equation holds for the barrier at the drain). Let now  $e^{-z/\lambda} = t$ ,

$$\ln T(E) = -2 \int_1^{\frac{E}{A_s}} \left[ -\frac{\lambda}{t} \sqrt{\frac{2M_\alpha}{\hbar^2} (A_s t - E)} \right] dt \quad (1.32)$$

$$4\lambda \sqrt{\frac{2M_\alpha}{\hbar} A_s t - \frac{2M_\alpha}{\hbar} E} - \sqrt{\frac{2M_\alpha}{\hbar} E} \arctan \left[ \frac{\frac{2M_\alpha}{\hbar} A_s t - \frac{2M_\alpha}{\hbar} E}{\frac{2M_\alpha}{\hbar}} \right] \Bigg|_{t=1}^{t=\frac{E}{A_s}} \quad (1.33)$$

$$\ln T(E) = -4\lambda \sqrt{\frac{2M_\alpha (A_s - E)}{\hbar^2}} \left[ 1 - \sqrt{\frac{E}{A_s - E}} \tan^{-1} \left( \sqrt{\frac{A_s - E}{E}} \right) \right] \quad (1.34)$$

After (1.26) is computed, the surface potential  $\phi_c$  can be determined by enforcing the equality between the micro-model and the macro-model in Section 1.5:

$$Q_{micro}(\phi_c) = Q_{macro}(\phi_c) \quad (1.35)$$

resulting in a nonlinear equation to be solved numerically.

Practically, the numerical solution of (1.35)  $f(\phi_c) = Q_{micro}(\phi_c) - Q_{macro}(\phi_c) = 0$  for the variable  $\phi_c$  is performed by applying the bisection method [57], described in Figure 1.14. One starts looking for the solution in an arbitrary interval  $[\phi_{c1\_initial}, \phi_{c2\_initial}]$  (in our case, we set  $\phi_{c1\_initial} = -2V$  and  $\phi_{c2\_initial} = 2V$ ). We employ the continuity of the function  $f(\phi_c)$  on the interval  $[\phi_{c1}, \phi_{c2}]$  and we check if  $f(\phi_{c1})$  and  $f(\phi_{c2})$  have opposite signs. If  $f(\phi_{c1\_initial})f(\phi_{c2\_initial}) > 0$ , no sign change is present in the interval  $[\phi_{c1}, \phi_{c2}]$  (the presence of one zero at the most is assumed in the interval), and the initial interval is extended. Otherwise, one zero of  $f$  is present in the interval  $[\phi_{c1}, \phi_{c2}]$ . The interval is divided in two and the procedure is repeated in each of the sub-intervals, until when the zero is found with a sufficient accuracy.

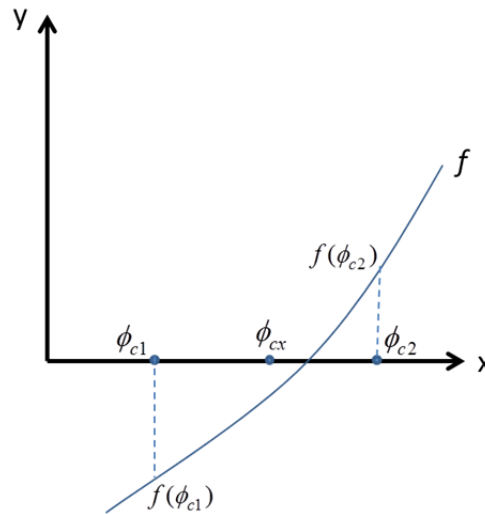


Figure 1.14: Illustration of the bisection method.

## 1.7 Research Objectives

### 1.7.1 Graphene nanoribbon based transistors

The electronic performance of graphene nanoribbon-based transistors is related with their geometric shape and working environment. In fact, strain operating on the flexible

substrate, and its subsequent deformation, could have a non-negligible impact on transistor performances (see Figure 1.15). Another interesting scenario where mechanical deformations could play a role is the use of transistors as bio-sensors [58]. The deformation of a graphene sheet would be related to the presence of a molecule to detect. For these reasons, we want to evaluate how the performance of graphene nanoribbon-based transistors will change when strains are applied on them.

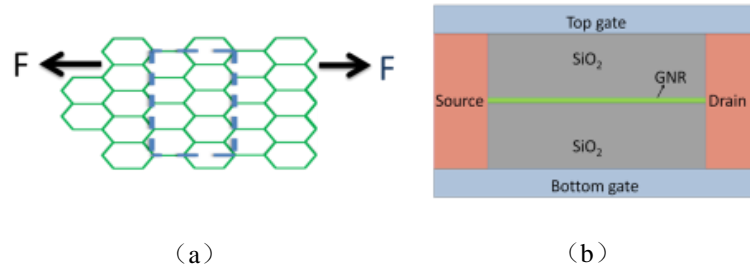


Figure 1.15: (a) deformed graphene nanoribbon, (b) sectional view of a double-gate aGNR FET.

The effect of mechanical deformations on electrical properties of nano-transistors should be taken into account though their impact on the conducting properties of graphene. This can be done of course by means of *ab-initio* calculation, which are quite computational expensive. However, thanks to the lattice symmetries of graphene and the assumption of small deformations, closed-form results for the impact of deformation on the full energy bands of graphene can be derived. In fact, previous work has already been performed to show the effect of deformations on energetic properties of graphene sheets and nanoribbons [59]-[61], with both *ab-initio* formulations and other models. In [62] the electronic structure of graphene and graphene nanoribbons under strain is studied by using first-principles approaches and tight binding theory. In [63], a field-effect transistor (FET) under strains is studied with first-principle approaches.

However, engineering applications to practical circuits require a simple model, whose parameters can be directly related to relevant geometric quantities. For this reason, we aim at employing the semi-analytical approach [56] described in Section 1.4.2 to study the electronic characteristics of FET. The effect of mechanical strain on graphene-based nanotransistors has not been previously taken into account in this approach in the literature. For this purpose, in Chapter 2 we consider nanoribbon transistors under deformation: we rigorously take into

account the effect of the deformation on the energy bands of the graphene and on the electrostatic analysis of the complete device. This leads to a complete characterization of the device in terms of its current-voltage characteristics. If the deformation is assumed small, as is expected in nanodevices for flexible electronics, due to the small dimensions of the transistor with respect to the local curvature radius of the deformed substrate, its effect will be seen to result both in a spectral scaling of energy bands and a Dirac-point shift. Both effects are derived on the basis of *ab-initio* simulations and are subsequently considered in our method. This approach is capable to describe both ballistic and partially-ballistic conduction regimes.

### 1.7.2 Graphene nanomesh based transistors

Creating regular holes in the graphene sheet (the so-called nanomesh graphene) may be another choice to tune the bandgap [64]. The structure of graphene nanomesh is shown in Figure 1.16 and the characteristics of nanomesh devices were first discussed in [64]. The advantage of graphene nanomesh in FET is having a high ON/OFF current ratio and a saturated current at high drain voltage.

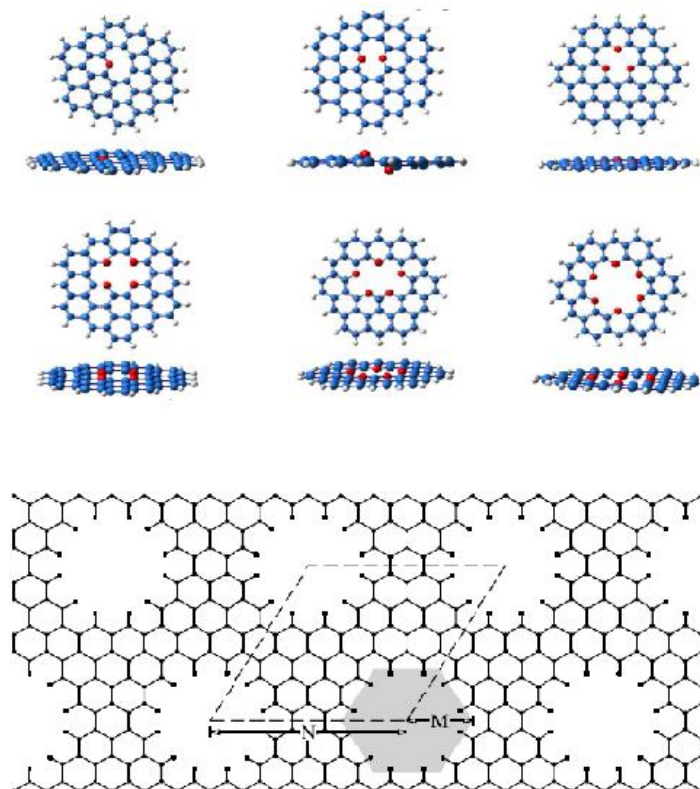


Figure 1.16: Structure of graphene nanomesh [65][66].

Electronic properties of graphene nanomesh have already been studied. In [67] the electronic properties of graphene nanomesh are computed by using first principle calculations, leading to the conclusion that zig-zag edged graphene nanomesh can be either semiconductors or semimetals according to their structure. In [68], the electronic, magnetic, and mechanical properties of graphene are studied by using a supercell method. The creation of a band gap due to quantum confinement in graphene nanomesh is discussed in [69], where a relationship between energy gap and hole arrangement is also given. Based on these previous studies of graphene nanomesh, in [70] the fabrication of graphene nanomesh which ribbon width less than 10 nm is achieved (see Figure 1.17). The fabricated graphene nanomesh samples are used in FET and the relationship between the On/Off current ratio and ribbon-width is obtained, showing that the On/Off current ratio increases when the ribbon width is reduced.

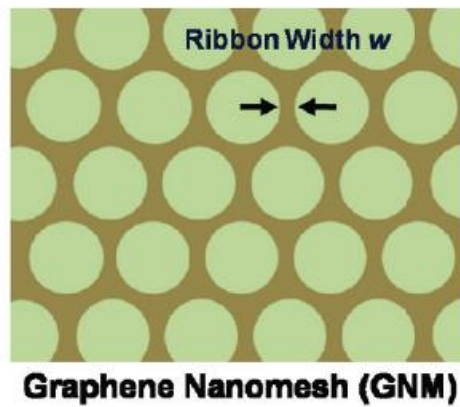


Figure 1.17: Schematic illustration of graphene nanomesh ribbon width [70].

In Chapter 3, computation and measurement of the  $I$ - $V$  characteristics of the graphene nanomesh transistors (see Figure 1.18) will be presented. We employ a semi-analytical compact approach based on the energy gap calculated with the *ab-initio* method. We compare the qualitative behavior of simulated devices with independent measurements performed on fabricated devices. We investigate the influence of mesh shape and of geometrical parameters on the conduction properties of the devices.

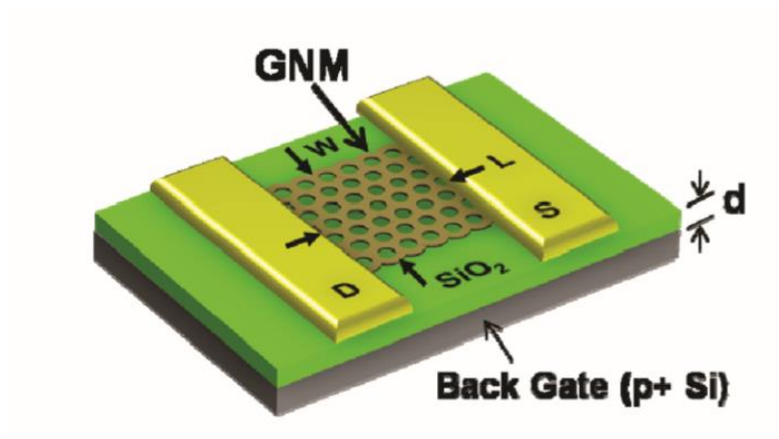


Figure 1.18: Nanomesh graphene transistor [70].

# Chapter 2. Dispersion Relations under Deformation and Schottky Field-Effect Transistor

In this chapter, a tight-binding model is used to describe the effect related to mechanical deformations of graphene nanoribbons on the performance of nano-transistors. We accordingly define modified effective masses and density of states which are necessary to be used in the description of graphene FET. Once electronic properties of graphene nanoribbons under strain are determined, the currents of the field effect transistor can be calculated.

Numerical results are presented in this Chapter for currents and potentials in a nanotransistor which channel is an aGNR strip with different widths, both in ballistic and in partially-ballistic regime. Both Ohmic contacts and Schottky barriers can be considered.

## 2.1 Energy bands of a deformed graphene nanoribbon

Equation (1.9) gives the energy bands of an aGNR in the absence of any geometrical deformation. In the presence of a relative deformation  $d$ , the values of the geometrical vectors  $\mathbf{R}_1$ ,  $\mathbf{R}_2$ , and  $\mathbf{R}_3$  describing the relative position of atoms will change accordingly into  $\mathbf{R}'_1$ ,  $\mathbf{R}'_2$  and  $\mathbf{R}'_3$  (the deformation is shown in Figure 2.1). Their values can be easily computed, thus leading to a modified equation for  $E_\alpha^d$ , the  $\alpha$ th energy band under deformation. The  $k_x$  dependence is then replaced in (1.9) into  $(1+d)k_x$ . On the one hand, regarding the  $k_y$  dependence, the width  $w$  in (1.7)-(1.8) is deformed into  $w' = w(1 - \nu_g d)$ , where  $\nu_g$  is the Poisson's ratio of the graphene, usually taken approximately equal to 0.145 [71]. The discretized values for  $k_y$  are scaled accordingly as  $k_{y,\alpha}^d = k_{y,\alpha}/(1 - \nu_g d)$ . The different values of the mutual distances among atoms modify also the relevant hopping parameter. More specifically, different hopping parameters are now expected depending on the considered couple of atoms, due to the loss of hexagonal symmetry. If we do not consider any variation of hopping parameter in the tight-binding Hamiltonian at this step, the argument of the cosines in the  $A_\alpha$  would then be unchanged due to the multiplication between  $k_{y,\alpha}^d$  and the

modified transverse dimension  $a(1 - \nu_g d)/2$ . In fact, by enforcing a hard condition on the electronic wavefunction  $\psi$ :

$$\psi \left[ y = -\frac{a}{2}(1 - \nu_g d) \right] = \psi \left[ y = (1 - \nu_g d) \left( w + \frac{a}{2} \right) \right] = 0 \quad (2.1)$$

we obtain the quantization condition

$$(1 - \nu_g d)(w + a)k_{y,\alpha}^d = \alpha\pi \quad (2.2)$$

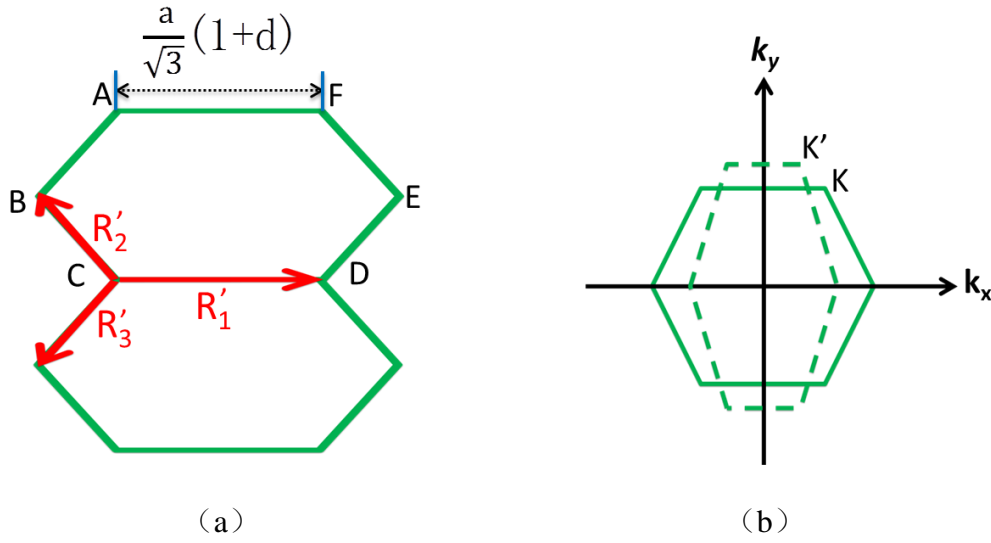


Figure 2.1: Deformation of Brillouin zone with the effect of strain (a) geometric effect of strain on graphene cell, (b) deformation of the Brillouin zone.

So that

$$k_{y,\alpha}^d = \frac{2\alpha\pi}{(N+1)a(1 - \nu_g d)} \quad (2.3)$$

The  $A_\alpha$  factor in (1.9) becomes then:

$$A_\alpha = \cos \left[ (1 - \nu_g d) \frac{a}{2} k_y^d \right] = \cos \left[ (1 - \nu_g d) \frac{a}{2} \frac{2\alpha\pi}{(N+1)a(1 - \nu_g d)} \right] = \cos \left( \frac{\pi\alpha}{N+1} \right) \quad (2.4)$$

where the effect of deformation has no impact. The final energy bands of the nanoribbon deformed along the  $x$  dimension is then:

$$E_{\alpha}^d(\mathbf{k}) = \pm V \sqrt{1 + 4 \cos \left[ (1+d) \frac{\sqrt{3}a}{2} k_x^d \right] \cos \left[ (1-v_g d) \frac{a}{2} k_y^d \right] + 4 \left\{ \cos \left[ (1-v_g d) \frac{a}{2} k_y^d \right] \right\}^2} \quad (2.5)$$

In (2.5), for convenience,  $k_x^d$  will be abbreviated as  $k$  in the following:

$$E_{\alpha}^d(k) = \pm V \sqrt{1 + 4 \cos \left[ (1+d) \frac{\sqrt{3}ak}{2} \right] A_{\alpha} + 4A_{\alpha}^2} \quad (2.6)$$

The band model (2.6) can be used together with a first-order correction  $\delta E'_{\alpha}$ , which is based on a perturbative approach [72] taking into account a different interaction among the atoms at the edges, being at a different chemical potential with respect to the central ones, by slightly varying their mutual hopping integrals:

$$\delta E'_{\alpha}(k) = \pm \frac{0.12V}{N+1} \sin^2 \left( \frac{\alpha\pi}{N+1} \right) \cos \left[ \frac{a(1+d)k}{\sqrt{3}} \right] \quad (2.7)$$

The edge-corrected energy dispersion is then:

$$E_{\alpha}^c(k) = E_{\alpha}^d(k) + \delta E'_{\alpha}(k) \quad (2.8)$$

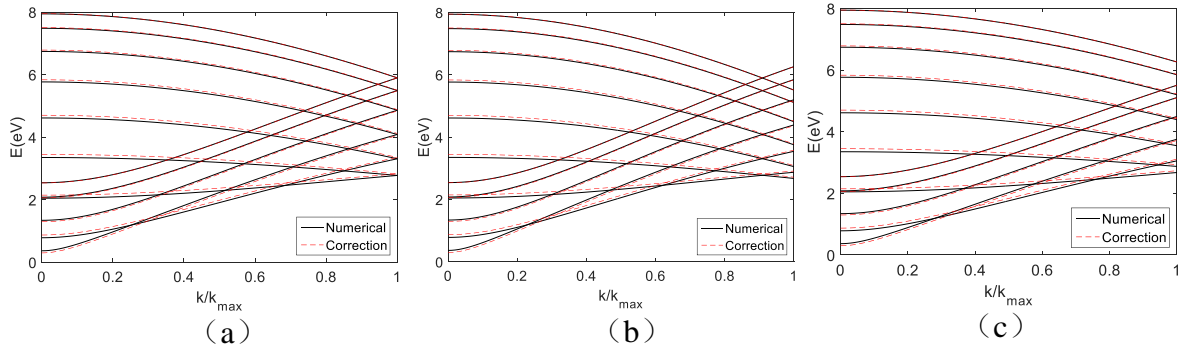


Figure 2.2: Comparison of the subbands of an aGNR with  $N=12$  lines between tight-binding calculation with and without edge correction. (a) No deformation (b) Relative deformation  $d=0.1$  (c) Relative deformation  $d=-0.1$ .

The discussion presented for energy dispersion is summarized in Figure 2.2, with and without edge correction (2.7) for different values of the relative deformation  $d$ . The solid black line represents the numerical result without edge correction and the dashed red line represents the result with edge correction.

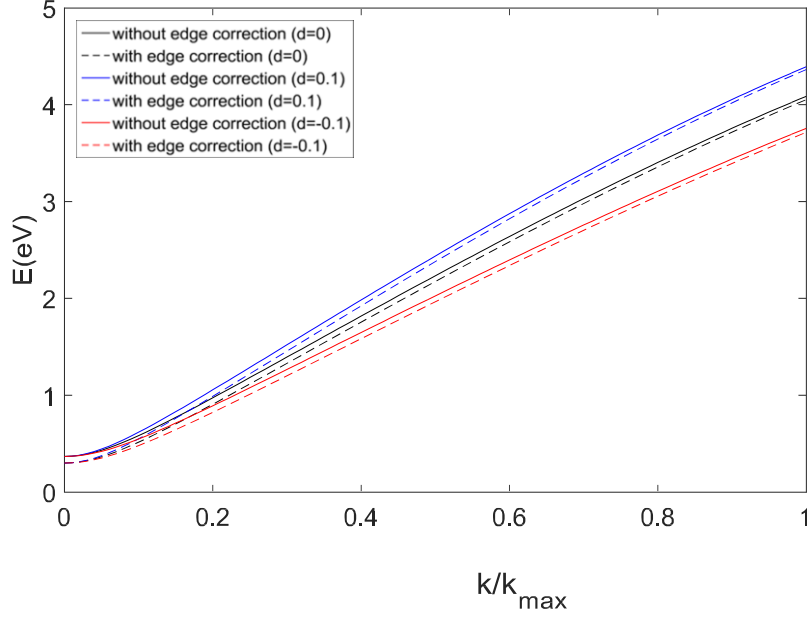


Figure 2.3: Comparison of the lowest subbands of an aGNR with 12 dimer lines with different deformations as explained in the legend.

An important limitation of (2.8) should be stressed: no energy-gap variation can be detected with this approach, as can be done with the first-principle formulations that will present next. This depends on the fact that the hopping integrals describing the interaction between two adjacent atoms have been kept constant even in the presence of a deformation. Therefore, we cannot see any change for energy gap in our simulation results as Figure 2.3 shows. In order to obtain more accurate results, the variation of hopping integrals under deformation should be taken into account, due to the presence of different distances among nearest-neighbor atoms [73]. When a symmetric strain is present, the Hamiltonian can be calculated with (1.2). If the strain applied is uniaxial, the hopping parameter depends on the bond lengths. In this case  $V_1$ ,  $V_2$ , and  $V_3$  are no longer equal and the Fermi point will deviate as Figure 2.1 shows.

The tight binding Hamiltonian is:

$$H(\mathbf{k}) = V_1 e^{-j\mathbf{k}\cdot\mathbf{R}_1} + V_2 e^{-j\mathbf{k}\cdot\mathbf{R}_2} + V_3 e^{-j\mathbf{k}\cdot\mathbf{R}_3} \quad (2.9)$$

In case of small deformations, a perturbation method can be performed on the Hamiltonian around the Fermi point. In order to do this, we need an analytic expression for the variation of the hopping parameters  $V_1$ ,  $V_2$ , and  $V_3$  with the respect to the deformation. A relation was proposed in [74][75] of the kind:

$$V_i = V(R_i/R_0)^2 \quad (2.10)$$

where  $R_0$  is the bond length between adjacent carbon atoms in the absence of strain, while  $R_i$  is the new bond length in the presence of strain.

In that case, a simplified model has been already proposed in [74] under the assumption that small deformations ( $|d| \ll 1$ ) are present and the effect of the variation of the hopping parameters can be regarded as an effective shift of the Dirac points of the graphene sheet [74]. This leads to an analytic expression for the energy band, and avoid the need to numerically compute the hopping parameters themselves.

More specifically, the shift of the Fermi point is described as a shift in the  $A_\alpha$  coefficients of the  $\alpha$ th energy bands. The energy band under deformation becomes

$$E_\alpha^d(k) = \pm V \sqrt{1 + 4 \cos \left[ (1+d) \frac{\sqrt{3}ak}{2} \right] A_\alpha^d + 4(A_\alpha^d)^2} \quad (2.11)$$

where

$$Ad_\alpha = \cos \left( \frac{\pi\alpha}{N+1} - \Delta k'_y \right) \quad \alpha = 1, \dots, N$$

$$\Delta k'_y = -\frac{\sqrt{3}}{2} S_t (1 + \nu_g) d$$

( $\alpha = 1, \dots, N$  defines the energy band),  $a = \sqrt{3}a_{cc}$  and  $a_{cc}$  is the atomic distance between two adjacent atoms,  $V = 2.7$  eV is the tight-binding hopping energy with no deformation.  $S_t$  is a constant reflecting the change of hopping parameter with respect to the bond lengths [74]:

$$S_t = -\frac{a}{2V} \frac{dV}{da} \quad (2.12)$$

If we use the relation (2.10) to calculate the tight binding Hamiltonian in presence of strain, the value of  $S_t$  equals to 1. However, later *ab-initio* simulations show that a better choice in nano-ribbon is  $S_t = 1.29$  [74]. This value will be used in the following results.

Two important features of (2.11) should be stressed. First, the presence of the factor  $d$  multiplying the wavenumber  $k$  derives from the spatial deformation, defining a reciprocal scaling in the spectral domain. However, as said before this geometrical effect does not account for a variation of the energy gap, which is a fundamental parameter for the evaluation of the transistor properties. The second feature is the presence of the  $\Delta k'_y$  shift in the term  $A_\alpha$ . As anticipated, this shift is the equivalent effect of the linear variation of hopping integrals. In the small-deformation hypothesis, its value is linearly varying with  $d$ , and correctly defines a modulation of the band-gap at  $k = 0$  [74]. This shift can be visualized as a shift of Fermi points: a graphical explanation can be seen in Figure 2.1(b), where Fermi points are the corners of the hexagonal Brillouin cell.

Figure 2.4 (a)-(c) show energy bands for different values of the relative deformation  $d$ . As can be observed, different deformation values can lead to different energy variations if we consider the change of hopping parameter. In Figure 2.5, the lowest sub-bands with different aGNR deformation are selected and compared among them. This choice is motivated by the fact that the lowest bands are the most important to describe conduction phenomena in FET devices.

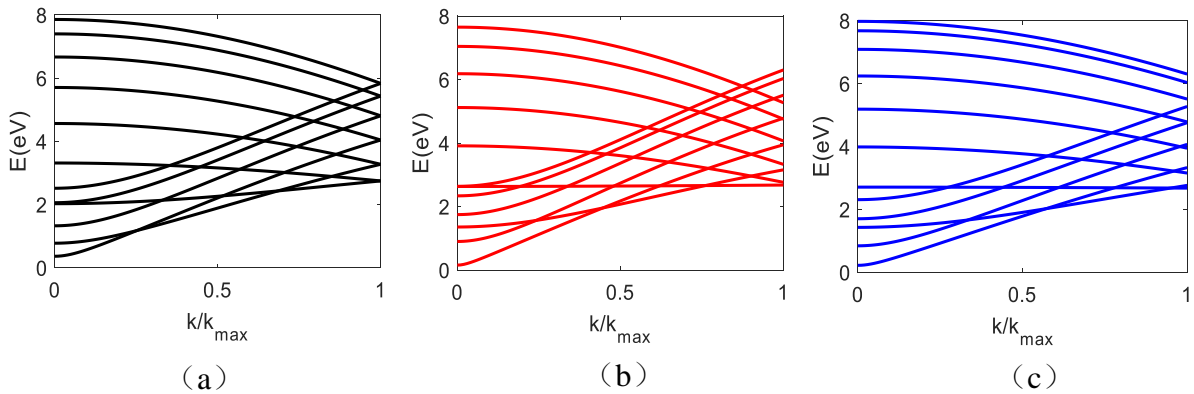


Figure 2.4: Comparison of the subbands of an aGNR with 12 lines between tight-binding calculation without edge corrections. (a) No deformation, (b) Relative deformation  $d = 0.1$ , (c) Relative deformation  $d = -0.1$ .

In Figure 2.5, we have observed that different deformation values can lead to different energy variations. In fact, as previously explained, a uniaxial strain has a non-negligible impact on the energy gap. For the further purpose of investigating the transistor performances, we have calculated the energy gap with different deformations ( $-0.1 \leq d \leq 0.1$ ). The energy

gap variation with respect to the relative deformation is shown in Figure 2.6. The results confirm that the energy gap oscillates following a zigzag pattern.

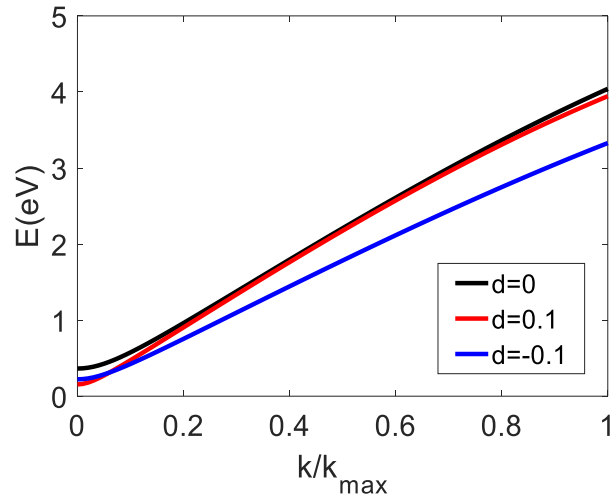


Figure 2.5: Comparison of the lowest subbands of an aGNR with 12 dimer lines with different deformations as explained in the legend.

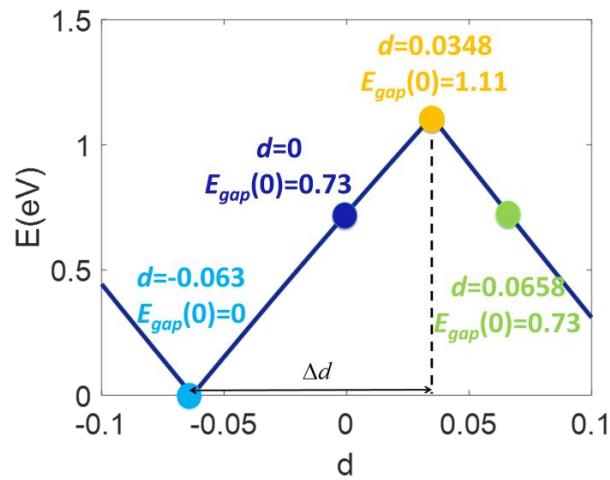


Figure 2.6: The calculated energy gap of aGNR with uniaxial strain  $d$ ,  $N=12$ .

Figure 2.6 is in perfect agreement with similar results obtained in [74], where a good agreement between the analytic approximation and first-principle calculations prove the accuracy of the model.

Under the linear approximation, the deviation of Fermi points is determined by:

$$\Delta k_F = \frac{S_t (1 + \nu_g) d}{a_{CC}} \quad (2.13)$$

where  $d$  is the uniaxial strain.

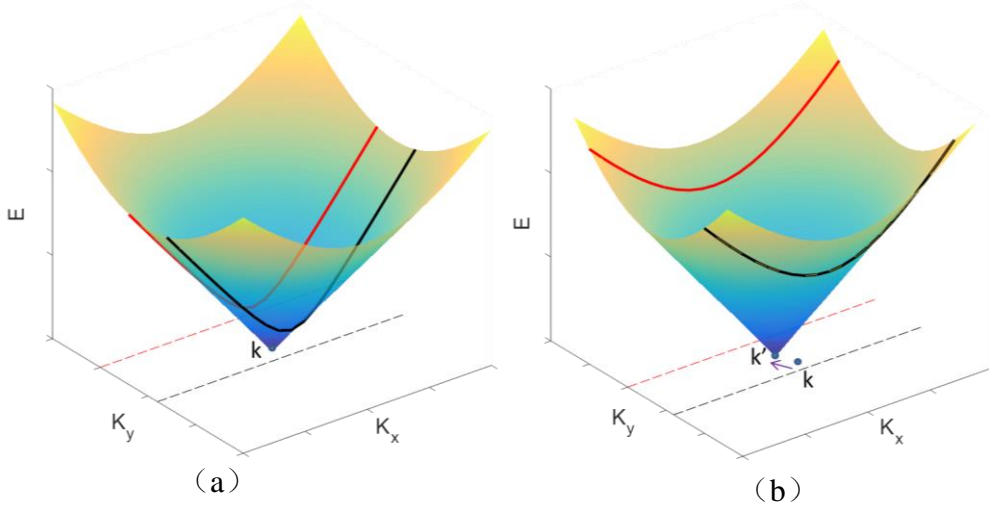


Figure 2.7: Schematic illustrations of the strain effect on aGNR bandgap.

The band gap is here defined as  $E_{\text{gap}} = 2E_{\alpha}^d(0)$  (the energy gap between the valence and the electronic bands). The variation of the energy bands with  $d$  can be graphically interpreted as the variation of the intersections between the discretized  $k_y$  lines and the Dirac cone which translates as  $d$  varies (Figure 2.7 and [74]). The variations of the bands lead of course to a variation of  $E_{\text{gap}}$ , which can be also calculated by recurring to the dispersion relation of the deformed graphene near the Fermi points. By assuming a locally linear dispersion close to the Fermi point:

$$E_{\alpha}^d(0) = \pm \frac{3}{2} V a_{CC} |\Delta k_F| \quad (2.14)$$

and then

$$E_{\text{gap}} = 2E_{\alpha}^d(0) = 2 \frac{3}{2} V a_{CC} |\Delta k_F| = 3V a_{CC} \frac{S_t (1 + \nu_g) d}{a_{CC}} = 3V S_t (1 + \nu_g) d \quad (2.15)$$

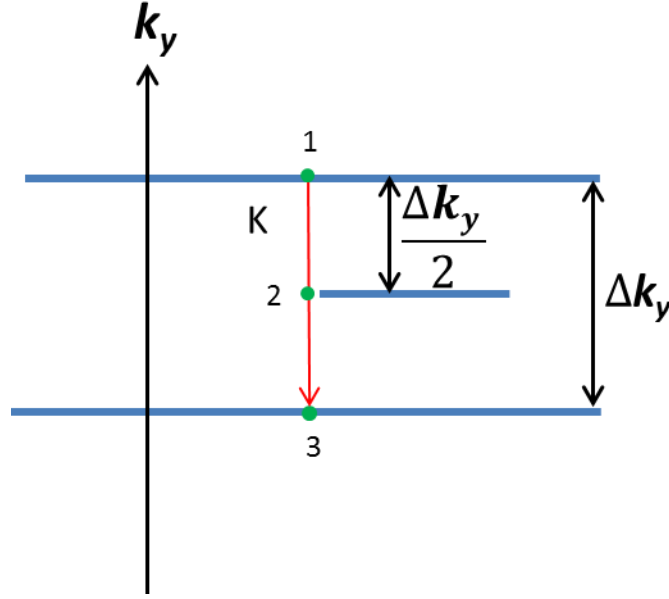


Figure 2.8: Schematic parallel  $k$ -lines for electronic states in aGNR

Figure 2.8 describes the shift of the Dirac point ‘K’ between neighboring  $k_y$ -lines, defined by the  $k_y$  discretization of the nanoribbon. If a strain is present the Dirac point is translated along the  $k_y$  axis according to (2.13), so that when the Dirac point arrives at the middle of these  $k_y$ -lines (position 2), the energy gap reaches the maximum. When the Dirac point coincides with a  $k_y$ -line (position 1 and position 3), the energy gap is decreased to 0. The solid red curve and solid black curve in Figure 2.7(a) are two neighboring energy dispersion lines. When the Dirac point moves from the K point to the K’ point, these two energy dispersion lines will change accordingly as Figure 2.7(b) shows.

$$\Delta k_y = \frac{2\pi(\alpha+1)}{\sqrt{3}a_{CC}(N+1)} - \frac{2\pi\alpha}{\sqrt{3}a_{CC}(N+1)} = \frac{2\pi}{\sqrt{3}a_{CC}(N+1)} \quad (2.16)$$

The variation of deformation required to go from a maximum to a minimum of the energy gap (i.e., the interval between two neighboring turning points) is here named  $\Delta d$  (see Figure 2.6), and can be interpreted as the deformation required for the Dirac point to move from position 1 to position 2. Therefore  $\Delta d$  is determined by imposing a consistency relation between expression (2.13) and (2.16).

$$\Delta k_F = \frac{\Delta k_y}{2} \quad (2.17)$$

From (2.13), if the Dirac point move from position 1 to position 2,

$$\Delta k_F = \frac{S_t(1+\nu_g)\Delta d}{a_{CC}} \quad (2.18)$$

The value of  $\Delta d$  is then

$$\Delta d = \frac{\pi}{\sqrt{3}S_t(1+\nu_g)} \frac{1}{N+1} \quad (2.19)$$

The maximum energy gap of aGNR can also be determined by the linear relationship,

$$E_{\text{gap}}^{\text{max}} = \frac{\sqrt{3}V\pi}{N+1} \quad (2.20)$$

The values of  $\Delta d$  and  $E_{\text{gap}}^{\text{max}}$  by using  $N=12$  are consistent with what we obtained in Figure 2.6. The linear dispersion relation around fermi point verifies the accuracy with respect to our modeling.

## 2.2 Effective mass and density of states

The previous model allows for the definition of the effective mass and the density of states, required to compute analytically the density of charge carriers in FETs. These parameters are introduced in Section 1.6 by recurring to approximations for small values of  $k$  [56], and should be modified to take into account the deformation of energy bands. Based on the discussion in previous section this is very simple, since a simple scaling together with a modification of the energy gap value need to be performed.

In nano-transistors modeling, we are concerned about the laying sub-bands which are related with the relevant transport phenomena. A simple parabolic approximation by developing both the cosines and the square root in (2.11) for small  $k$  leads to the definition of the effective mass  $M_\alpha^d$  of the deformed nanoribbon:

$$E_\alpha^{\text{EM,d}} = E_\alpha^d(0) + \frac{\hbar^2 k^2}{2M_\alpha^d} \quad (2.21)$$

$$M_{\alpha}^d = -\frac{2}{3} \frac{\hbar^2 E_{\alpha}^d(0)}{a^2 V^2 (1+d)^2 A_{\alpha}^d} \quad (2.22)$$

If only the cosines is approximated in (2.11), we obtain a simplified expression for the energy which keeps the square root, and which is more accurate on a large interval and for smaller values of the energy gaps:

$$E_{\alpha}^d(k) = \sqrt{\left[E_{\alpha}^d(0)\right]^2 + \frac{\hbar^2 E_{\alpha}^d(0) k^2}{M_{\alpha}^d}} \quad (2.23)$$

The formulas (2.21)-(2.23) extends similar results obtained in [56] for the non-deformed nanoribbon energy bands.

By means of the expressions (2.22) and (2.23), the density of states (DOS) in the presence of deformation can also be defined. DOS describes the density of mobile electrons or holes present in the solid at a given temperature [12]. This quantity is necessary to compute the charge densities and currents in the FET in the semi-analytic model. The definition of  $M_{\alpha}$  also allows different definitions of the density of states  $D_{\alpha}$  in the presence of deformation, according to the approximation chosen for the energy. Starting from the first-order approximation we obtain

$$D_{\alpha}^{\text{EM-d}} = \frac{2}{\pi \hbar} \sqrt{\frac{M_{\alpha}^d}{2 \left[E_{\alpha}^d(k) - E_{\alpha}^d(0)\right]}} \quad (2.24)$$

while, starting from the second-order approximation, we obtain

$$D_{\alpha}^{\text{I-d}} = \frac{2}{\pi \hbar} \sqrt{\frac{M_{\alpha}^d}{E_{\alpha}^d(0)}} \frac{\left[E_{\alpha}^d(k)\right]^2}{\sqrt{\left[E_{\alpha}^{\text{I-d}}(k)\right]^2 - \left[E_{\alpha}^d(0)\right]^2}} \quad (2.25)$$

The definition of the density of states is useful in order to compute electron density carrier by using Fermi-Dirac distributions functions.

The relations discussed in this subsection are summarized in Figure 2.9. In Figure 2.9(a), the tight-binding energy dispersion (2.5) together with its effective-mass (EM) approximation and the more accurate I-EM approximation are shown in the absence of any

deformation in the picture on the left. The corresponding densities of states for each approximation are shown in the figure on the right. The same results are shown in Figure 2.9 (b) and (c) for a deformation  $d = 0.1$  and  $d = -0.1$ , respectively. All the numerical results are computed for an aGNR with  $N = 12$ . It can be observed that the density of states changes accordingly to the different deformation values. In Figure 2.9, the variation of the energy dispersion edge  $E_\alpha^d(0)$  with different  $d$  is very visible. The results of energy dispersion also verify the accuracy of energy gap in Figure 2.6.

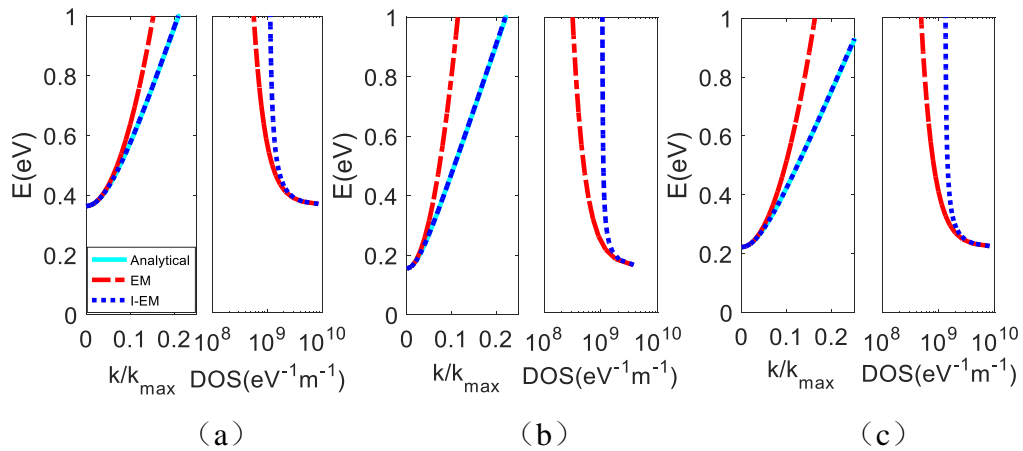


Figure 2.9: Energy dispersion curves and corresponding density of states of the lowest conduction subband of an aGNR with  $N = 12$ . (a) No deformation, (b)  $d = 0.1$ , (c)  $d = -0.1$ .

All these results extend the analysis done in [56] for non-deformed nanoribbon. It is easy to verify that the final formulas have the same form of the non-deformed expressions, apart from a change in the values of the energy gaps of each band  $E_\alpha^d(0)$ , the spectral scaling, and the replacement of the discretization factor  $A_\alpha$  with the deformed discretization factor  $A_\alpha^d$  responsible for the translation of the K point. Some care is however necessary when these formulas are used in equation (1.25) in order to compute the total charges on the microscopic scale. Since deformations can modify the energy gaps  $E_\alpha^d(0)$ , we require the formulation to be uniformly valid as  $E_\alpha^d(0)$  becomes arbitrarily small. In this limit (see Figure 2.7) the energy band becomes locally a straight line, having a locally constant density of states. This

linear expression is recovered in (2.23) if we put  $E_\alpha^d(0)=0$ , but not in (2.21). The approximation I-EM must then be used in our analysis.

Furthermore, in [56], a closed-form of the integrals in (1.25) valid with ohmic contacts (the  $T$  coefficients being unitary) is proposed in the assumption of a nondegenerate situation ( $E_\alpha(0)-3kT > \mu$ ). This allows for replacing the Fermi-Dirac distribution with a Maxwell-Boltzmann distribution [76]. The following result is obtained:

$$\int_0^{E^{\max}-E(0)} D_\alpha(E) f(\eta_{\alpha,s}^i) dE \cong \frac{2}{\pi\hbar} \sqrt{M_\alpha E_\alpha(0)} e^{\frac{q\varphi_c+\mu}{kT}} \int_1^{+\infty} e^{-\frac{z}{kT}} \frac{z}{\sqrt{z^2-1}} dz =$$

$$\frac{2}{\pi\hbar} \sqrt{M_\alpha E_\alpha(0)} e^{\frac{q\varphi_c+\mu}{kT}} K_1 \left[ \frac{E_\alpha(0)}{kT} \right] \quad (2.26)$$

This integral expression and the final closed-form result in term of the first-order Kelvin function  $K_1$  is not valid if  $E_\alpha^d(0) \rightarrow 0$ . Of course, this follows from the fact that the degenerate assumption is not verified. This is also clear by looking at the fact that the function  $K_1$  diverges for small arguments. In our approach, we compute then numerically these integrals even in the case of ohmic contacts. Note also that a close-form expression for the integral can be obtain if  $E_\alpha^d(0) = 0$  (closing of the energy gap):

$$\int_0^{E^{\max}} D_\alpha(E) f(\eta_{\alpha,s}^i) dE \cong \frac{2}{\pi\hbar} \sqrt{\frac{M_\alpha}{E_\alpha(0)}} \frac{1}{kT} \int_1^{+\infty} \frac{1}{1+e^{-\frac{E-q\varphi_c+\mu}{kT}}} dE =$$

$$\frac{2}{\pi\hbar} \sqrt{\frac{M_\alpha}{E_\alpha(0)}} kT \ln \left[ 1+e^{\frac{q\varphi_c+\mu}{kT}} \right] \quad (2.27)$$

### 2.3. Deformations in Schottky Field-Effect Transistor

Once the electronic properties of graphene nanoribbons under strain are determined, such as effective mass and density of states, the currents of the FET shown in Figure 2.10 can be calculated.

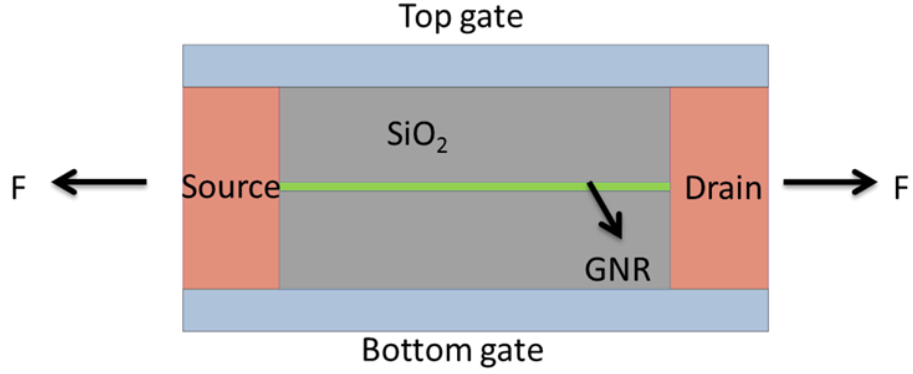


Figure 2.10: Sketch of strain on FET.

Equation (1.31) gives simple expressions for the transmissivity coefficients  $T_s$  and  $T_d$ . These parameters are used to calculate the current by using (1.20). We should notice that all the quantities in (1.20) are now computed in the presence of the same relative deformation  $d$ .

Any deformation along the source-drain direction will cause a deformation along the vertical direction too, expressed through the Poisson coefficient  $\nu_{SiO_2}$  (usually taken as 0.17) of the  $SiO_2$  dielectric [77], and a deformation along the nanoribbon width, expressed through the Poisson coefficient of the graphene nanoribbon  $\nu_g$ , usually taken approximately equal to 0.145 [71]. Such modifications of the oxide thickness  $t'_{SiO_2}$  and of the nanoribbon width  $w'$  will change the gate capacitance. The same formula *equation* (1.14) is used with different geometric parameters

$$C_g^d(t'_{SiO_2}, w') = C_g[t_{SiO_2}(1 - \nu_{SiO_2}d), w(1 - \nu_gd)] \quad (2.28)$$

## 2.4 Study of deformation effects on carbon-based transistors with Semi-Analytic and Ab-Initio Models

In this section we want to study the accuracy of the semi-analytic multiscale method discussed in Section 1.4.2 before using it to study the effects of longitudinal deformations of FET devices. To do so, the same physical device has been simulated with a different model. To compute the drain/source current in the presence of strain as a function of the voltages at the contacts, we have proposed an alternative method based on an *ab-initio* approach, jointly with the Federal University of Paraná (Brazil).

The method has been briefly described in Sect 1.5. We add here that, when a strain is applied, we use the elastic energy potential based on Hook’s law, which is a Taylor expansion around the minimum of the energy bounding two atoms. This expansion, ignoring higher orders terms, has a parabolic form, where second derivative is known as the spring constant  $K$ .  $K$  is found by considering the Poisson ratio and the graphene Young’s module  $Y$  by [78]

$$K = \frac{1}{3} \cdot \left( \frac{Y}{1-2\nu} \right) \quad (2.29)$$

The Young’s module is based on experimental data [79]. Also, the positions used in the Hamiltonian operator are modified, thus defining a “geometrically deformed” Hamiltonian.

We plot in Figure 2.11 the band diagram for the nanoribbon, where dashed lines show the analytical approach used in our compact model, while solid lines come from the *ab-initio* technique considering second nearest neighbors.

Despite the differences in the highest sub-bands, with no practical impact for transport analyses, we can see a very good match between the models. This result guarantees that the orbitals chosen for the *ab-initio* procedure are capturing the correct physical effects, and that the near-neighbor approximation used in the semi-analytic approach is sufficiently accurate.

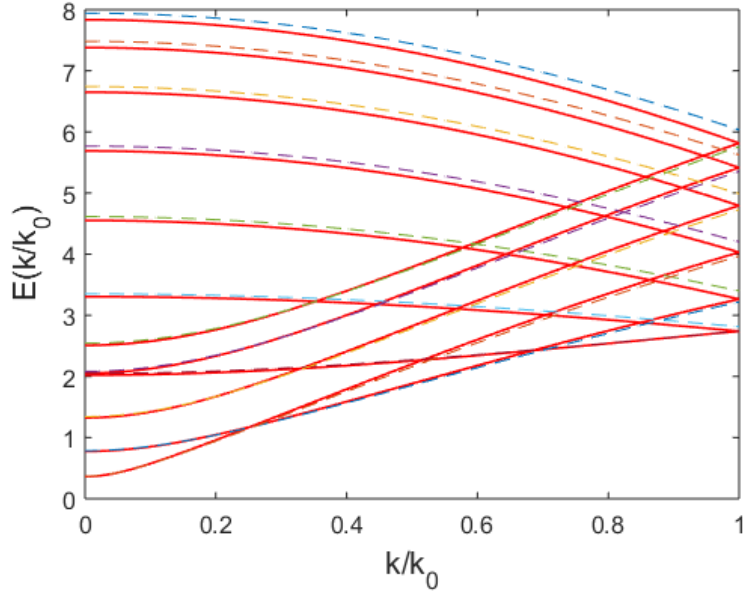


Figure 2.11: Band diagram of aGNR without deformation. *Ab-initio* procedure (*solid lines*), analytic equation (*dashed lines*).

In Figure 2.12(a) the drain-source current  $I_{ds}$  is calculated by keeping a constant gate potential  $V_g = 0.75$  V and changing the drain-source potential. In Figure 2.12(b) a constant gate potential  $V_{ds} = 0.5$  V is kept and the drain-source potential varies. In both figures, dashed lines come from the semi-analytic procedure, while solid lines from the *ab-initio* technique. By varying the parameter  $d$  the difference between the models is very small, meaning that the semi-analytic model correct captures the variation of the current with a significantly reduced computational complexity.

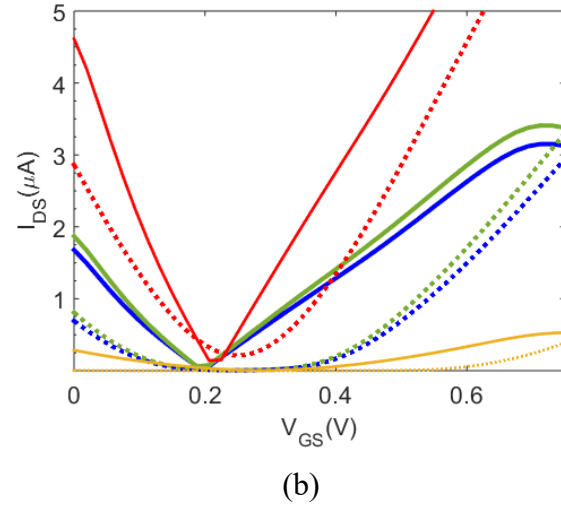
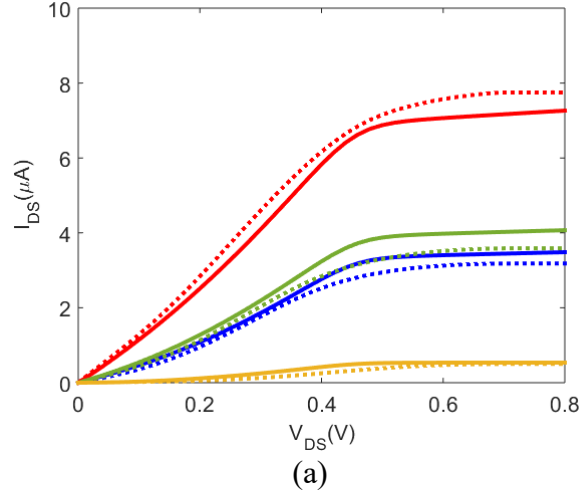


Figure 2.12: (a) Current  $I_{ds}$  vs. drain-source voltage  $V_{ds}$ .  $V_g = 0.75$  V. (b) Current  $I_{ds}$  vs. drain-source voltage  $V_{gs}$ .  $V_{ds} = 0.5$  V. Semi-analytic (*dashed lines*) and ab-initio results (*solid lines*). No deformation (*blue lines*),  $d = 0.0658$  (*green lines*),  $d = 0.08$  (*red lines*),  $d = 0.0348$  (*yellow lines*).

Interestingly, the green case ( $d = 0.0658$ ) has the same energy gap for the blue case ( $d = 0$ ), but even so we can capture some differences in their current levels. This difference comes from the Schottky barrier present at the contacts in both models. This means that, even in the presence of the same energy gap, the semi-analytic model is able to capture the effects of a strain.

We have to notice that in Figure 2.12 (b), for transfer characteristics, there are some discrepancies between the currents obtained with the *ab-initio* technique and the semi-analytic

method. This could depend on the different treatment of the consideration of edge effects, which are not present in the simplified method, and on different treatment of the boundary conditions at the contacts between the methods (gold contacts have been simulated in the *ab-initio* method, while ohmic contacts have been used in the analytic approach).

The semi-analytic method is by far faster than the *ab-initio* one. On an Intel Core i5-6300HQ @ 2.3GHzx4 and 8GiB of memory, the former requires around 1 minute of computation, while the latter takes more than 2 hours to compute 72 values of currents in the curves of Figure 2.12.

We also tested the computation time of our semi-analytic method for different cases in the same computer (Intel Core i7-4790CPU @ 3.6GHz and 16GB of memory). For ballistic regime, when  $N=9$ , each value of current in the curve for ballistic regime takes 0.453s; when  $N=12$ , each value of current in the curve for ballistic regime takes 0.731s; when  $N=15$ , each value of current in the curve for ballistic regime takes 0.746s. For 3 mean free path, when  $N=9$ , each value of current for partially ballistic regime takes 35.3 s; when  $N=12$ , each value of current for partially ballistic regime takes 21s; when  $N=15$ , each value of current for partially ballistic regime takes 73.6s. For 10 mean free path, when  $N=9$ , each value of current for partially ballistic regime takes 69.8 s; when  $N=12$ , each value of current for partially ballistic regime takes 139.8s; when  $N=15$ , each value of current for partially ballistic regime takes 932s.

## 2.5. Semi-analytical multiscale coupled modeling

Here we apply the semi-analytic method discussed in Section 1.4.2 and validated in previous section in order to study the effects of longitudinal deformations of the device on the current characteristics.

Numerical results are presented for currents and potentials in a deformed nanotransistor whose channel is an aGNR strip with different widths, both in ballistic and in partially ballistic regimes. We show at first results obtained in the approximation of constant hopping parameters. As shown in the previous sections, this choice does not describe the variation of the energy gap. Later, the full model with energy-gap variation will be used. Values for  $d$  are selected corresponding to different energy gaps, according to the results in

Figure 2.6. This choice of  $d$  and the comparison with the first simplified model will confirm the dominant role of energy gap values to determine the transistor current and the related parameters.

### **2.5.1 A short discussion on the tight binding model without variation of hopping parameters**

If the variation of the hopping parameter with the deformation is not considered, we can directly use (2.8) in our numerical modeling. As we said, no energy-gap variation with the deformation can be described. The non-deformed energy gap is then used to determine the effective mass and the density of states.

Some results are presented here for comparison with the results of the following subsection, keeping the correct hopping parameter variation. We studied both models in the absence of Schottky contacts (Ohmic contacts) and in the presence of Schottky contacts (SB contacts). The transmissivity coefficients  $T_s$  and  $T_d$  are used to calculate the current in (1.20). For numerical simulation with Schottky contacts, the transmission coefficients can be calculated through (1.31). For numerical simulation with Ohmic contacts, the transmission coefficients  $T_s$  and  $T_d$  are set equal to 1.

In Figure 2.13(a) and (b) we plot the currents  $I_{ds}$  with the Ohmic contacts without any deformation. In Figure 2.13(a),  $I_{ds}$  is varied by keeping a constant potential  $V_{DS} = 0.5$  V and changing the gate potential  $V_g$ . In Figure 2.13(b),  $I_{ds}$  is varied by keeping a constant gate potential  $V_g = 0.75$  V and changing the drain-source potential  $V_{ds}$ .

In Figure 2.13(c) and (d) we plot the currents  $I_{ds}$  in the presence of Schottky contacts without any deformation. In Figure 2.13(c),  $I_{ds}$  is varied by keeping a constant potential  $V_{ds} = 0.5$  V and changing the gate potential  $V_g$ . In Figure 2.13(d),  $I_{ds}$  is varied by keeping a constant gate potential  $V_g = 0.75$  V and changing the drain-source potential  $V_{ds}$ .

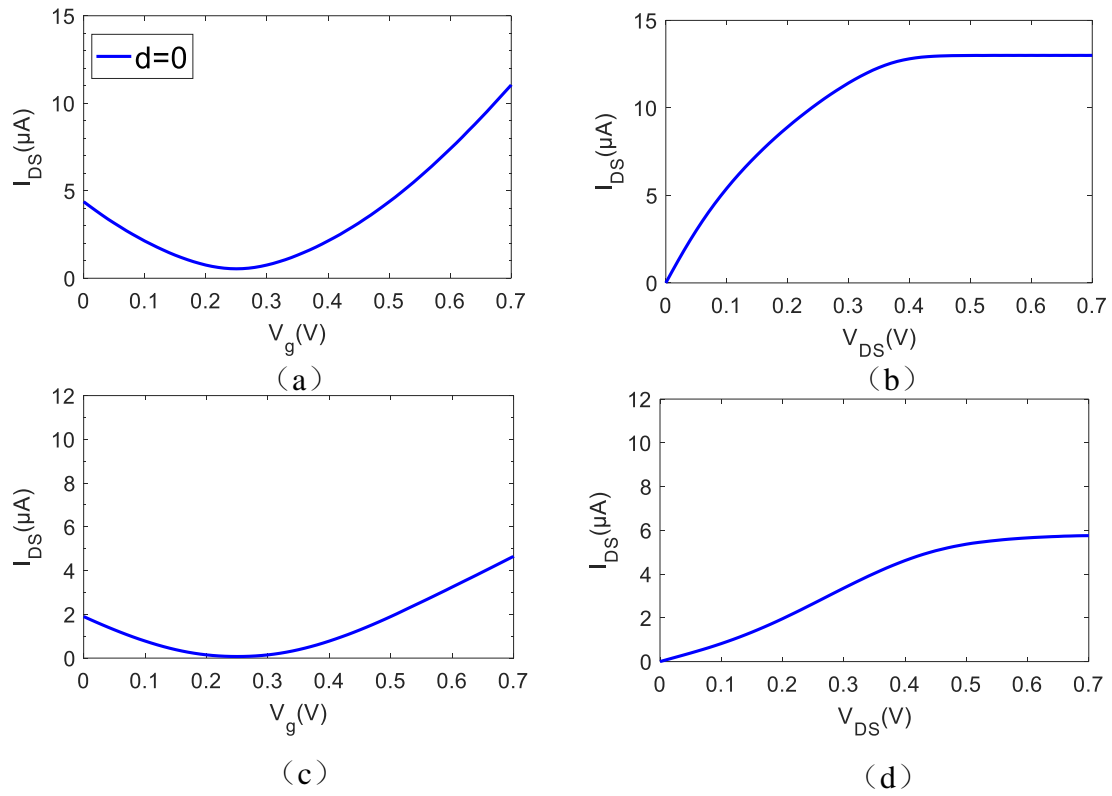


Figure 2.13: Source-drain current  $I_{ds}$  with  $N = 12$ . (a)  $I_{ds}$  vs.  $V_g$ , at  $V_{ds} = 0.5$  V with ohmic contacts. (b)  $I_{ds}$  vs.  $V_{ds}$ , at  $V_g = 0.75$  V with ohmic contacts. (c)  $I_{ds}$  vs.  $V_g$ , at  $V_{ds} = 0.5$  V with SB contacts. (d)  $I_{ds}$  vs.  $V_{ds}$ , at  $V_g = 0.75$  V with SB contacts.

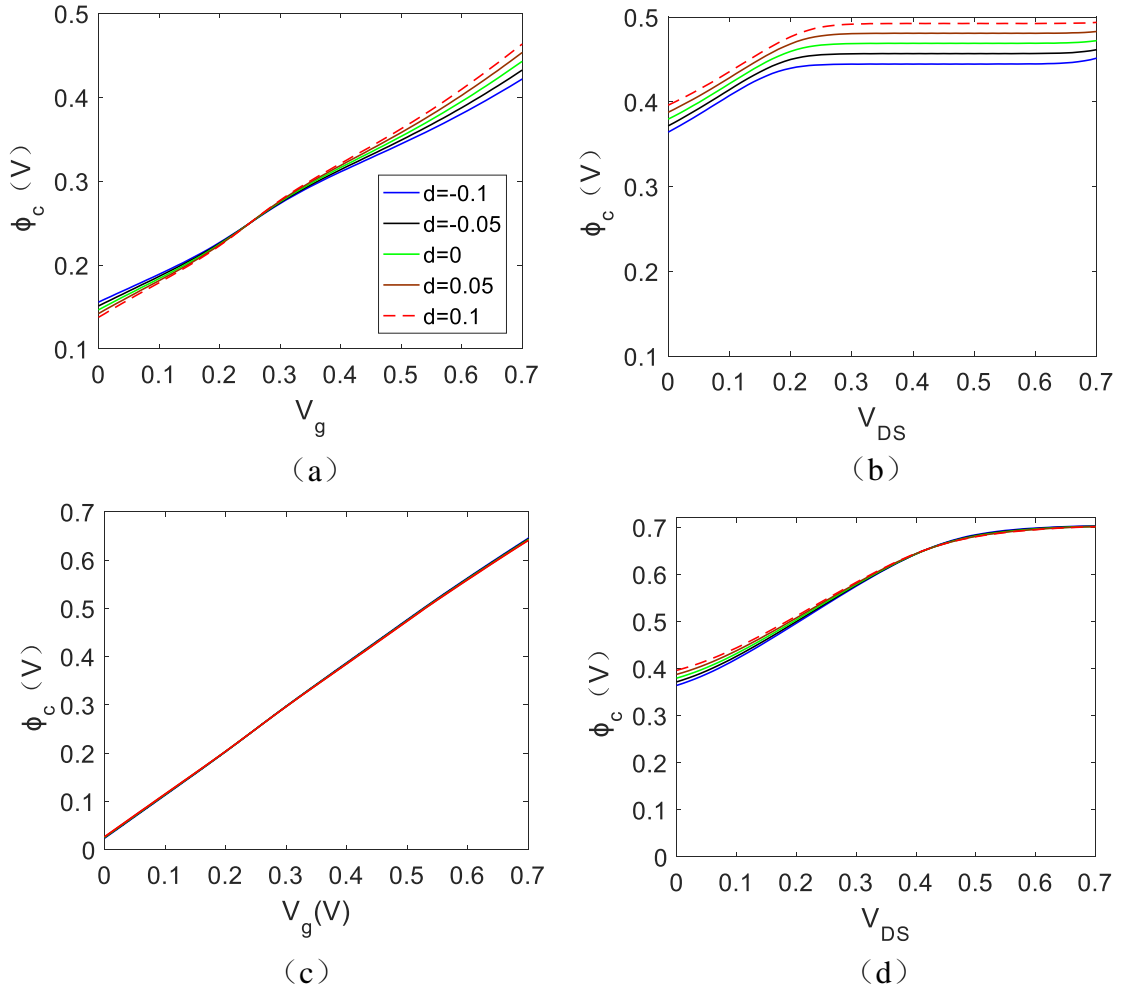


Figure 2.14: Channel potential with  $N = 12$ . (a)  $\phi_c$  vs.  $V_g$ , at  $V_{ds} = 0.5$  V with ohmic contacts. (b)  $\phi_c$  vs.  $V_{ds}$ , at  $V_g = 0.75$  V with ohmic contacts. (c)  $\phi_c$  vs.  $V_g$ , at  $V_{ds} = 0.5$  V with SB contacts. (d)  $\phi_c$  vs.  $V_{ds}$ , at  $V_g = 0.75$  V with SB contacts.

In Figure 2.14 we plot the variation of the channel potential  $\phi_c$  in different contact configurations and voltage excitation. Since a purely ballistic transport is considered in these figures, the potential is constant along the channel, and its variation with the voltages  $V_g$  and  $V_{ds}$  is shown. In Figure 2.14(a) and (b) Ohmic contacts are considered, and  $\phi_c$  is computed when the gate potential  $V_g$  and the drain-source potential  $V_{DS}$  is varied, respectively. The same results are shown in Figure 2.14(c) and (d) in the presence of Schottky contacts. Different values of the relative deformation  $d$  are shown in order to study the effect of  $d$  on the potential values. The variation is very small for the Schottky contacts, while it is slightly more evident in the case of Ohmic contacts.

$\phi_c$  is strongly related with the computation of the charges stored inside the channel. In Figure 2.15 (a) and (b) we plot  $Q$  in the absence of Schottky contacts, and in Figure 2.15(c) and (d) the presence of Schottky contacts is considered. Consistently with the previous results of  $\phi_c$ , a smaller variation with  $d$  is obtained for the Schottky contacts with respect to the Ohmic contacts.

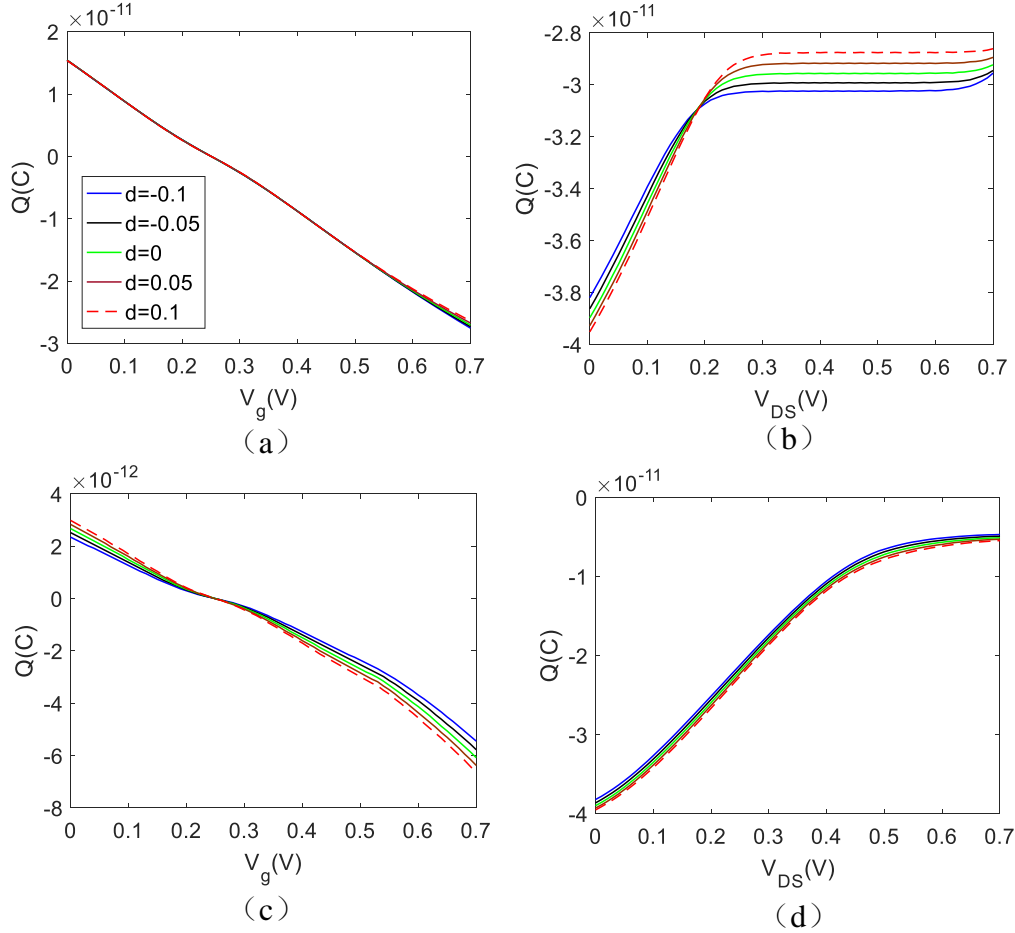


Figure 2.15: Macroscopic Charge  $Q$  with  $N = 12$ . (a)  $Q$  vs.  $V_g$ , at  $V_{ds} = 0.5$  V with ohmic contacts. (b)  $Q$  vs.  $V_{ds}$ , at  $V_g = 0.75$  V with ohmic contacts. (c)  $Q$  vs.  $V_g$ , at  $V_{ds} = 0.5$  V with SB contacts. (d)  $Q$  vs.  $V_{ds}$ , at  $V_g = 0.75$  V with SB contacts.

After the potential and the charges have been determined, the current  $I_{ds}$  can be computed. In Figure 2.16(a) and (b) we plot the currents  $I_{ds}$  for different strains with the Ohmic contacts. In Figure 2.16(a),  $I_{ds}$  is varied by keeping a constant potential  $V_{DS} = 0.5$  V and changing the gate potential  $V_g$ . In Figure 2.16(b),  $I_{ds}$  is varied by keeping a constant gate potential  $V_g = 0.75$  V and changing the drain-source potential  $V_{ds}$ . In Figure 2.16 (c) and (d) we plot the currents  $I_{ds}$  for different strains in the presence of Schottky contacts. In Figure

2.16 (c),  $I_{ds}$  is varied by keeping a constant potential  $V_{ds} = 0.5$  V and changing the gate potential  $V_g$ . In Figure 2.16 (d),  $I_{ds}$  is varied by keeping a constant gate potential  $V_g = 0.75$  V and changing the drain-source potential  $V_{ds}$ .

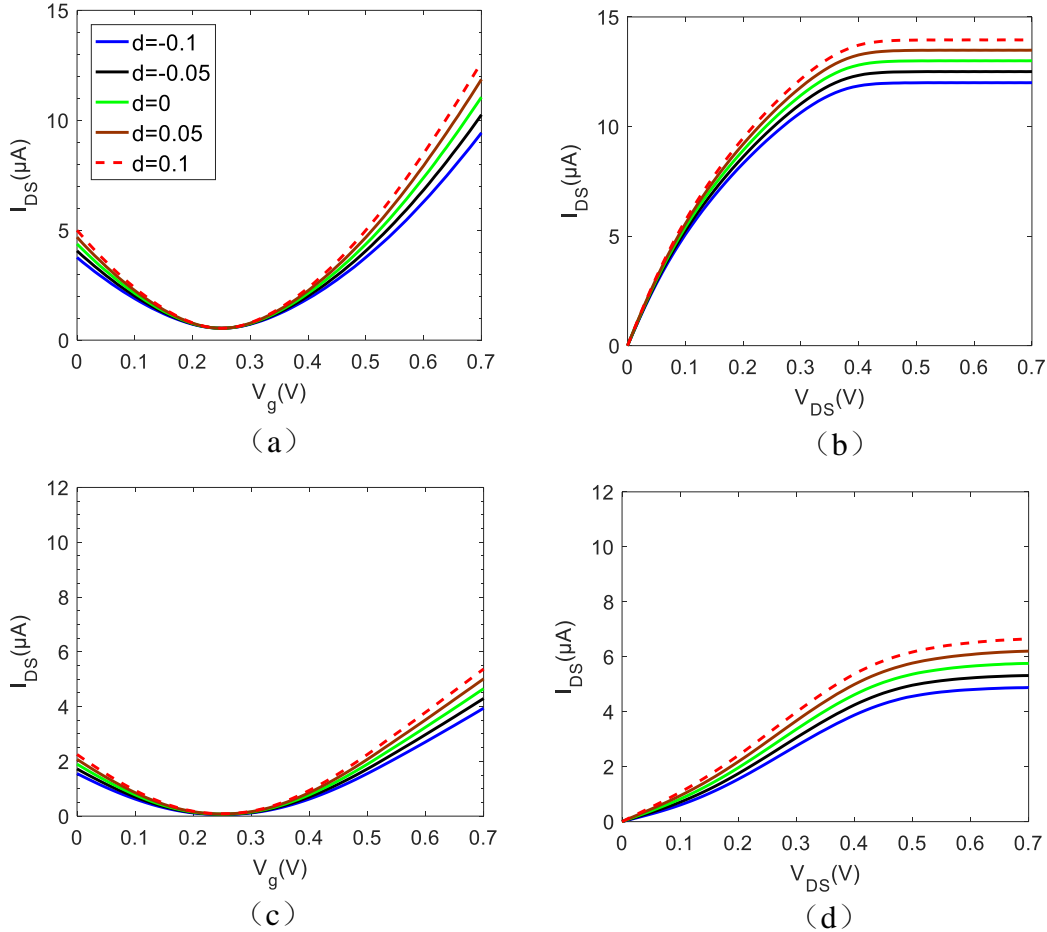


Figure 2.16: Source-drain current  $I_{ds}$  with  $N = 12$ . (a)  $I_{ds}$  vs.  $V_g$ , at  $V_{ds} = 0.5$  V with ohmic contacts. (b)  $I_{ds}$  vs.  $V_{ds}$ , at  $V_g = 0.75$  V with ohmic contacts. (c)  $I_{ds}$  vs.  $V_g$ , at  $V_{ds} = 0.5$  V with SB contacts. (d)  $I_{ds}$  vs.  $V_{ds}$ , at  $V_g = 0.75$  V with SB contacts.

Different ranges of relative deformation  $d$  are studied in order to discuss their effects on the computed current. Small values of  $d$  ( $d < 0.1$ ) are associated with applications of this class of devices to flexible electronics. As it can be seen in these results, the geometrical deformation of the graphene lattice together with the variation of the capacitance (2.28) are responsible of a slight variation of the saturation currents either for Ohmic and Schottky contacts.

## 2.5.2 The full model of deformation: the Ballistic regime

We show now the results obtained with the full method including deformations of energy bands and variations of the energy gaps of each sub-band. As expected, if compared with the results in the previous paragraph, energy gap considerably change both the effective mass and the density of states. These variations have a non-negligible impact on the computation of the density of charge and currents, much larger than the simple spectral scaling used in the previous section where the modification of the hopping parameters has been neglected.

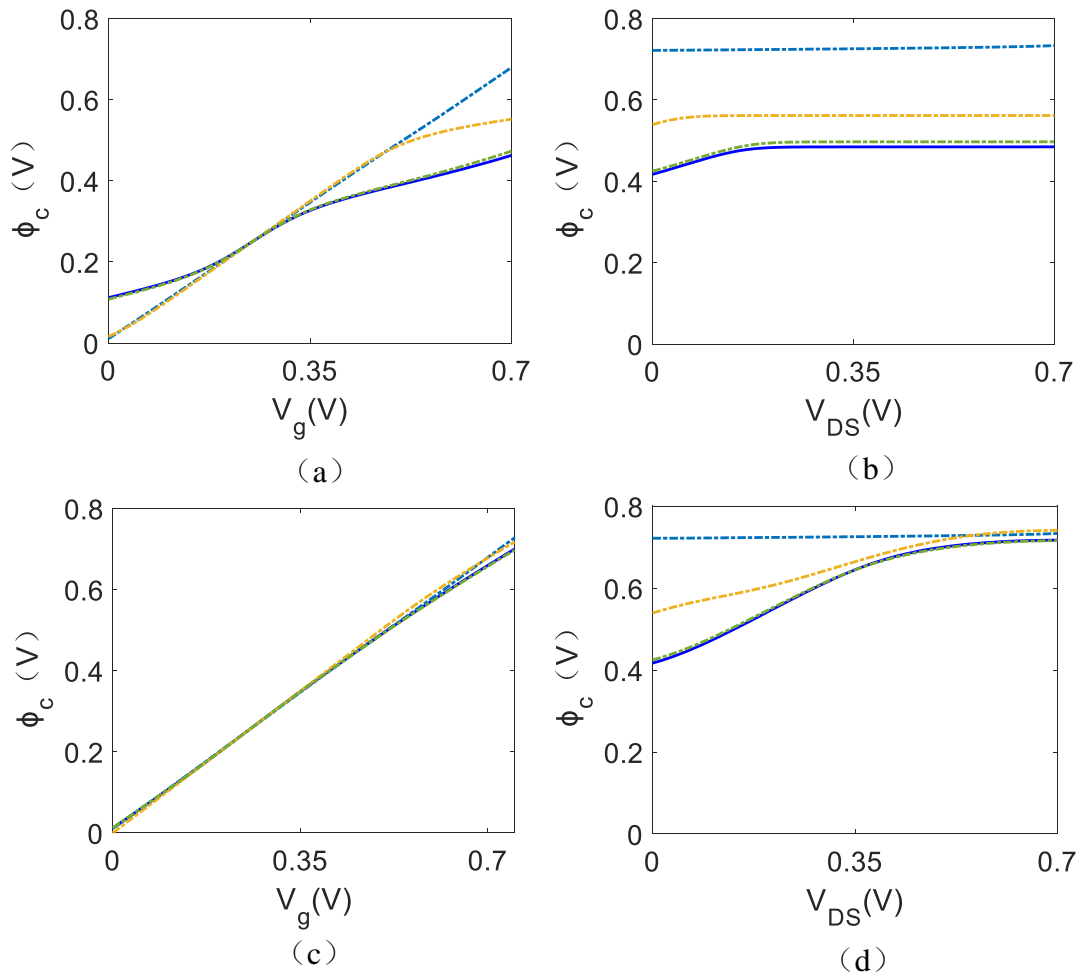


Figure 2.17: Channel potential with  $N = 12$ . (a)  $\phi_c$  vs.  $V_g$ , at  $V_{ds} = 0.5$  V with ohmic contacts. (b)  $\phi_c$  vs.  $V_{ds}$ , at  $V_g = 0.75$  V with ohmic contacts. (c)  $\phi_c$  vs.  $V_g$ , at  $V_{ds} = 0.5$  V with SB contacts. (d)  $\phi_c$  vs.  $V_{ds}$ , at  $V_g = 0.75$  V with SB contacts. Considered deformations:  $d = -0.063$  (dashed light blue line),  $d = 0$  (solid dark blue line),  $d = 0.0348$  (yellow line),  $d = 0.0658$  (green line).

In this paragraph, we show results concerning transistors in ballistic regime. As explained in Section 1.4.2, the ballistic regime occurs when the length of the channel is shorter than the mean-free path and the charge carriers move without experiencing any scattering. In this hypothesis, the channel potential  $\phi_c$  is considered constant along the channel and equation (1.35) is a scalar equation solved once for each contact voltage configuration.

In Figure 2.17 (a) and (b) we plot the surface potential  $\phi_c$  in the absence of Schottky contacts with respect to  $V_g$  (Figure 2.17 (a)) and is changed with respect to  $V_{ds}$  (Figure 2.17(b)). The same results are shown in Figure 2.17 (c) and (d) respectively, in the presence of Schottky contacts. These potentials are computed by solving the multiscale equation (1.35) with the full effect of deformation on nanoribbon energy bands. The source-drain current  $I_{ds}$  of a single ballistic-regime transistor is here computed using the Landauer–Büttiker approach, for different values of  $d$ . In Figure 2.18(a) and (b) we plot the currents  $I_{ds}$  with ohmic contacts, as a function of  $V_g$  (Figure 2.18(a)) and as a function of  $V_{ds}$  (Figure 2.18(b)). The expected typical behaviors of currents controlled by the gate voltage and a definite threshold  $V_g$  voltage are visible in the figures, and can be evaluated in a simple way with this approach. In the absence of deformation, the method agrees with results given in [56]. In Figure 2.18(c) and (d) we plot the currents  $I_{ds}$  in the presence of Schottky contacts. In Figure 2.18(c),  $I_{ds}$  is varied by keeping a constant potential  $V_{ds} = 0.5$  V and changing the gate potential  $V_g$ . In Figure 2.18(d),  $I_{ds}$  is varied by keeping a constant gate potential  $V_g = 0.75$  V and changing the drain-source potential  $V_{ds}$ .

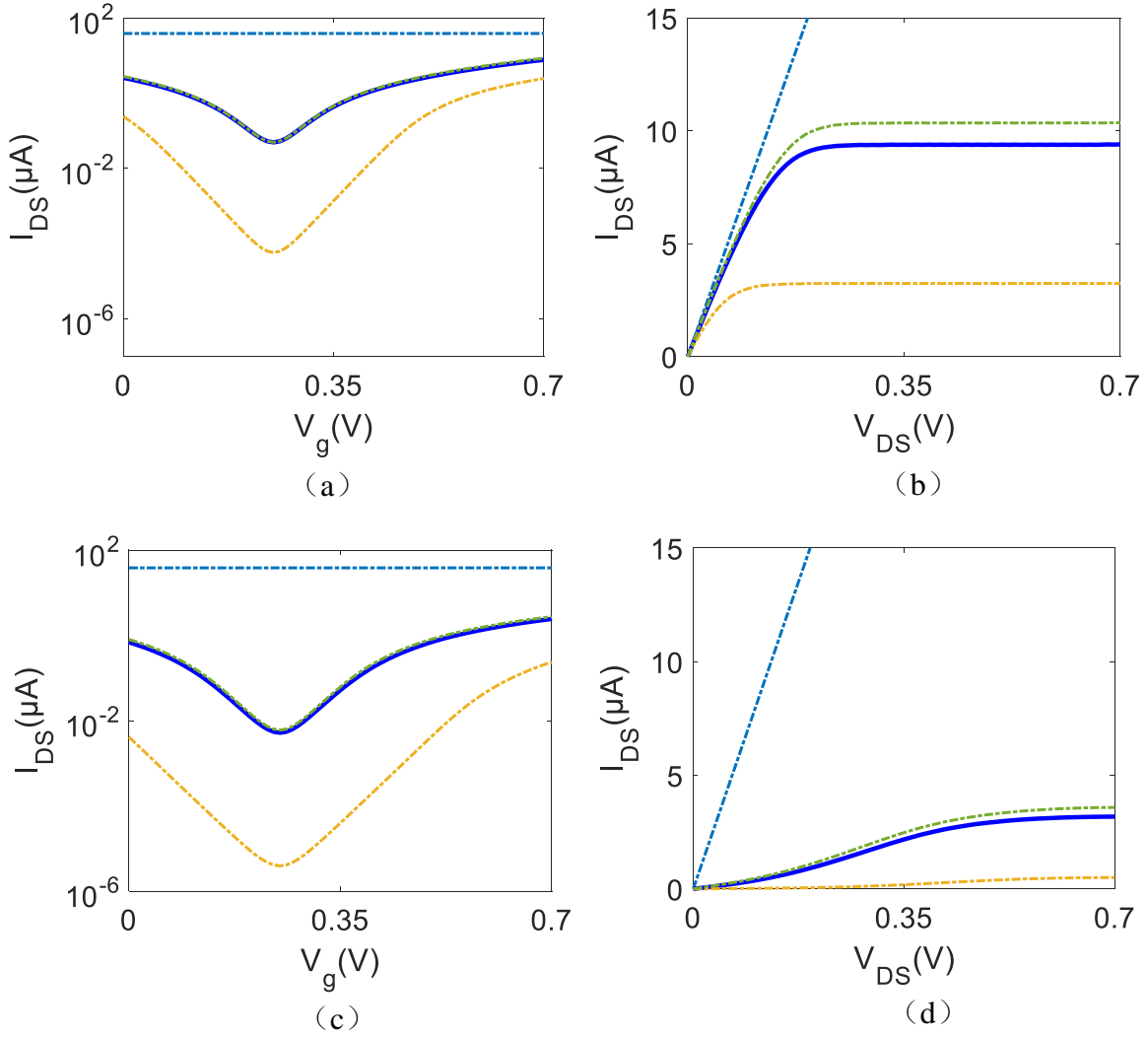


Figure 2.18: Source-drain current  $I_{ds}$ . (a)  $I_{ds}$  vs.  $V_g$ , at  $V_{ds} = 0.5$  V with ohmic contacts. (b)  $I_{ds}$  vs.  $V_{ds}$ , at  $V_g = 0.75$  V with ohmic contacts. (c)  $I_{ds}$  vs.  $V_g$ , at  $V_{ds} = 0.5$  V with SB contacts. (d)  $I_{ds}$  vs.  $V_{ds}$ , at  $V_g = 0.75$  V with SB contacts. Considered deformations:  $d = -0.063$  (dashed light blue line),  $d = 0$  (solid dark blue line),  $d = 0.0348$  (yellow line),  $d = 0.0658$  (green line).

Deformations do lead to observable variation in the current. However, if the numerical value of the energy gap is sufficiently large, the entity of these variations is not such to jeopardize the transistor functioning. Otherwise, if the numerical value of energy gap is very small, the variations has serious effect on transistor functioning. When the deformation suppresses any gap, the channel behaves as a metal. Different mechanical deformations can result in a similar energy gap. For instance, the numerical values of energy gap when  $d = 0$  and  $d = 0.0658$  are almost the same (see Figure 2.6). It can be observed in this case that corresponding curves of source-drain current  $I_{ds}$  are nearly overlapped. These results confirm

the importance of a correct modeling of the energy gap variation as the main factor determining the transistor performance.

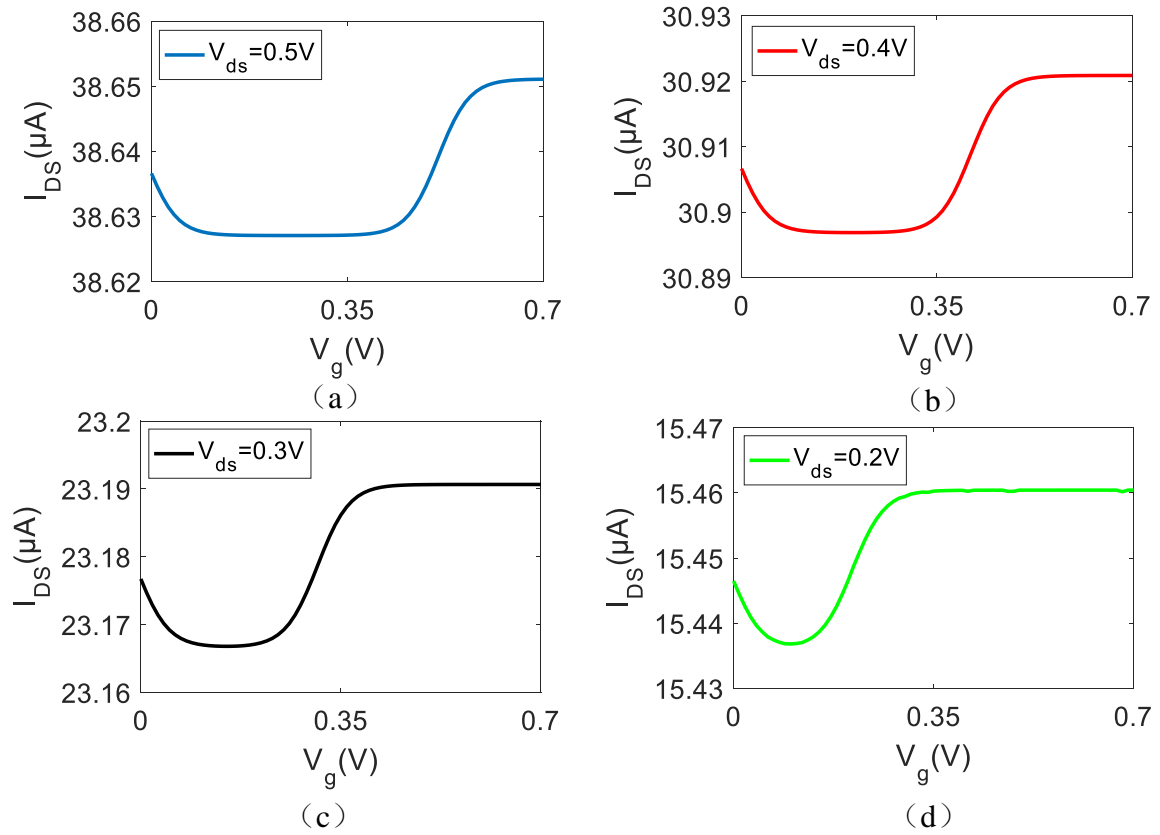


Figure 2.19: Source-drain current  $I_{ds}$ ,  $d = -0.063$ , ohmic contacts. (a)  $I_{ds}$  vs.  $V_g$ , at  $V_{ds} = 0.5$  V. (b)  $I_{ds}$  vs.  $V_g$ , at  $V_{ds} = 0.4$  V. (c)  $I_{ds}$  vs.  $V_g$ , at  $V_{ds} = 0.3$  V. (d)  $I_{ds}$  vs.  $V_g$ , at  $V_{ds} = 0.2$  V.

In Figure 2.19 we plot the currents  $I_{ds}$  with ohmic contacts when  $d = -0.063$ , with respect to  $V_g$ . This deformation suppresses energy gap for aGNR. In Figure 2.19(a),  $I_{ds}$  is varied by keeping a constant potential  $V_{ds} = 0.5$  V and changing the gate potential  $V_g$ . For Figure 2.19(b), Figure 2.19(c) and Figure 2.19(d),  $I_{ds}$  is varied by keeping a constant potential  $V_{ds} = 0.4$  V,  $V_{ds} = 0.3$  V,  $V_{ds} = 0.2$  V separately. From Figure 2.19, we see that, even if the deformation suppresses any gap, the current is not perfectly constant, but there are some small variations implying a on-off current ratio different from one, as observed in the literature. The ratio will change as expected as a function of  $V_{ds}$ .

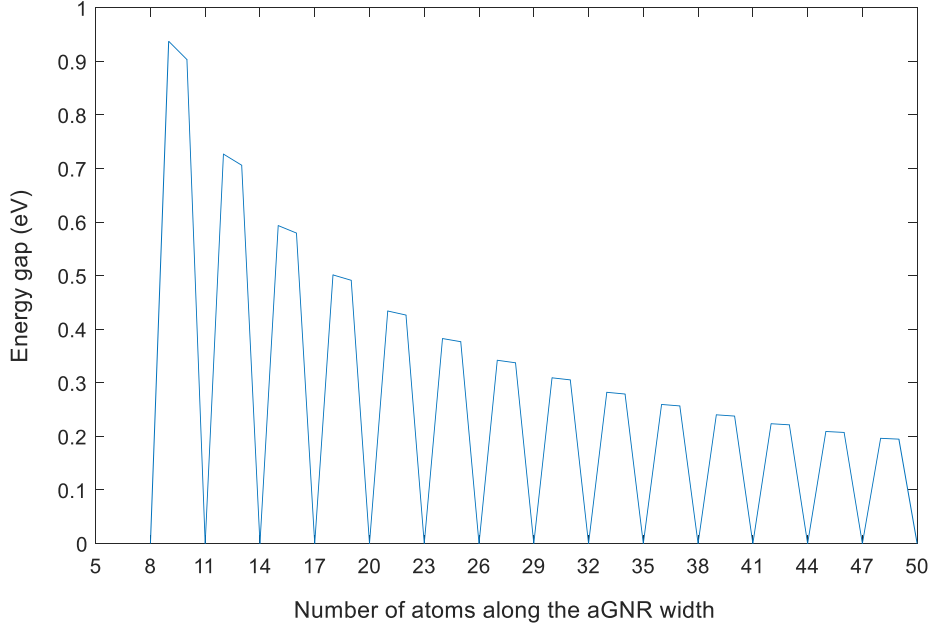


Figure 2.20: Relation of energy gap and number of atom in aGNR

Figure 2.20 shows energy gaps for different values of atoms along the width of the nanoribbon. As is well known (and can be verified with (2.6)), different number of atoms along the aGNR width can lead to different energy gaps. When the number of atoms equals to  $3z+2$  (where  $z$  is the positive integer), the energy gap becomes zero. The energy gap of aGNR is proportional to the number of atoms along the width direction. From the Figure 2.20, we can see for all values of  $z$ ,  $E_{\text{gap}}(3z) \geq E_{\text{gap}}(3z + 1) > E_{\text{gap}}(3z + 2) \approx 0$ .

Different values of carbon atoms in the direction of the ribbon width have been investigated. In Figure 2.21 (a) and (b) we plot the currents  $I_{\text{ds}}$  with the ohmic contacts for  $N=9$  atoms. In Figure 2.21 (a),  $I_{\text{ds}}$  is varied by keeping a constant potential  $V_{\text{DS}} = 0.5$  V and changing the gate potential  $V_{\text{g}}$ . In Figure 2.21 (b),  $I_{\text{ds}}$  is varied by keeping a constant gate potential  $V_{\text{g}} = 0.75$  V and changing the drain-source potential  $V_{\text{ds}}$ . In Figure 2.21 (c) and (d) we plot the currents  $I_{\text{ds}}$  in the presence of Schottky contacts. In Figure 2.21(c),  $I_{\text{ds}}$  is varied by keeping a constant potential  $V_{\text{ds}} = 0.5$  V and changing the gate potential  $V_{\text{g}}$ . In Figure 2.21(d),  $I_{\text{ds}}$  is varied by keeping a constant gate potential  $V_{\text{g}} = 0.75$  V and changing the drain-source potential  $V_{\text{ds}}$ .

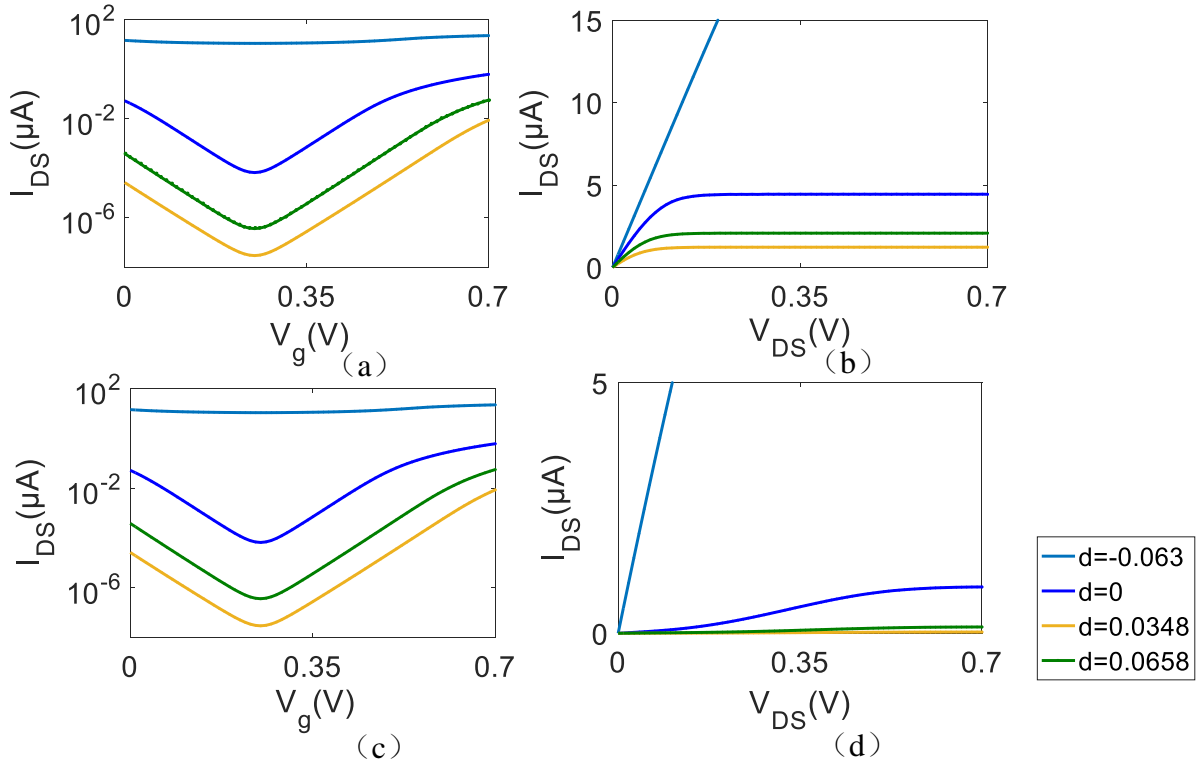


Figure 2.21: Number of atom for aGNR  $N=9$ , source-drain current  $I_{ds}$ . (a)  $I_{ds}$  vs.  $V_g$ , at  $V_{ds} = 0.5$  V with ohmic contacts. (b)  $I_{ds}$  vs.  $V_{ds}$ , at  $V_g = 0.75$  V with ohmic contacts. (c)  $I_{ds}$  vs.  $V_g$ , at  $V_{ds} = 0.5$  V with SB contacts. (d)  $I_{ds}$  vs.  $V_{ds}$ , at  $V_g = 0.75$  V with SB contacts. Considered deformations:  $d=-0.063$  (light blue line),  $d=0$  (dark blue line),  $d=0.0348$  (yellow line),  $d=0.0658$  (green line).

In Figure 2.22(a) and (b) we plot the currents  $I_{ds}$  with the ohmic contacts for  $N=15$  atoms, with respect to  $V_g$  (Figure 2.22(a)) and with respect to  $V_{ds}$  (Figure 2.22(b)). In Figure 2.22 (c) and (d) the same results are shown with Schottky contacts.

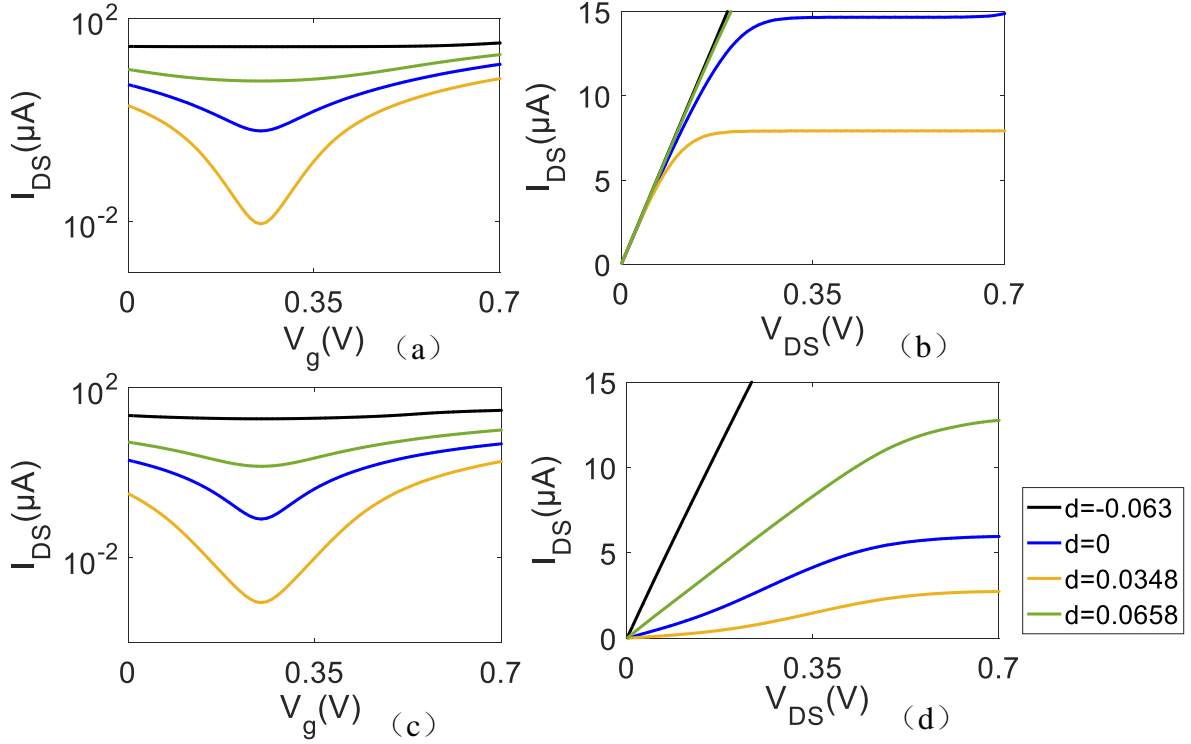


Figure 2.22: Number of atom for aGNR  $N=15$ , source-drain current  $I_{ds}$ . (a)  $I_{ds}$  vs.  $V_g$ , at  $V_{ds} = 0.5$  V with ohmic contacts. (b)  $I_{ds}$  vs.  $V_{ds}$ , at  $V_g = 0.75$  V with ohmic contacts. (c)  $I_{ds}$  vs.  $V_g$ , at  $V_{ds} = 0.5$  V with SB contacts. (d)  $I_{ds}$  vs.  $V_{ds}$ , at  $V_g = 0.75$  V with SB contacts. Considered deformations:  $d=-0.063$  (black line),  $d=0$  (dark blue line),  $d=0.0348$  (yellow line),  $d=0.0658$  (green line).

In Figure 2.21 and Figure 2.22, the same deformation values as in the previous  $N=12$  case are chosen ( $d=-0.063$ ,  $d=0.0348$ ,  $d=0.0658$ ). Again, different deformations also lead to observable variation in the current. We observe different effects on the current with respect to the previous  $N = 12$  case, since the number of the atom of aGNR modifies the energy band variation as a function of  $d$ . This is visible in (2.19). While similar gaps are found for  $d = 0$  and  $d = 0.0658$  in the  $N=12$  case, the same does not happen when  $N$  changes. Energy gaps are not similar anymore (as shown in Figure 2.23 and Figure 2.24). Figure 2.21 and Figure 2.22 again illustrate the importance of a correct modeling of the energy gap variation.

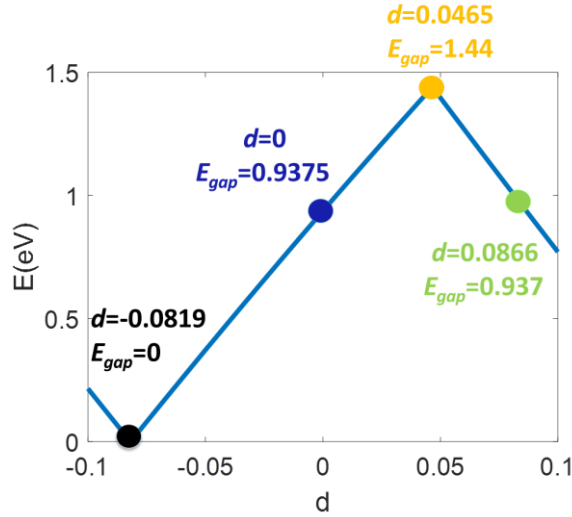


Figure 2.23: Energy gap of aGNR with respect to the uniaxial strain  $d$ ,  $N=9$  atoms along the width.

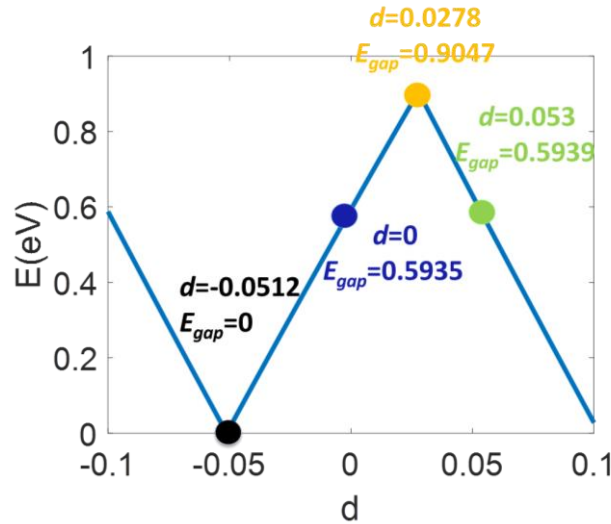


Figure 2.24: Energy gap of aGNR with respect to the uniaxial strain  $d$ ,  $N=15$  atoms along the width.

We have also calculated the energy gap when  $N=9$  and  $N=15$ . Energy gap variation for 9 atom aGNR with respect to different deformations ( $-0.1 \leq d \leq 0.1$ ) is shown in Figure 2.23. The 15-atom case is shown in Figure 2.24. The zigzag oscillation pattern commented in Figure 2.6 is recovered.

We now select the deformations of  $d = -0.819$ ,  $d = 0$ ,  $d = 0.0465$ ,  $d = 0.0866$  for  $N = 9$ ; they are shown explicitly in Figure 2.23. In Figure 2.25(a) and (b) we keep Ohmic contacts

and in Figure 2.25 (c) and (d) we keep Schottky contacts. Again, similar current behaviors are recovered for similar gaps as expected.

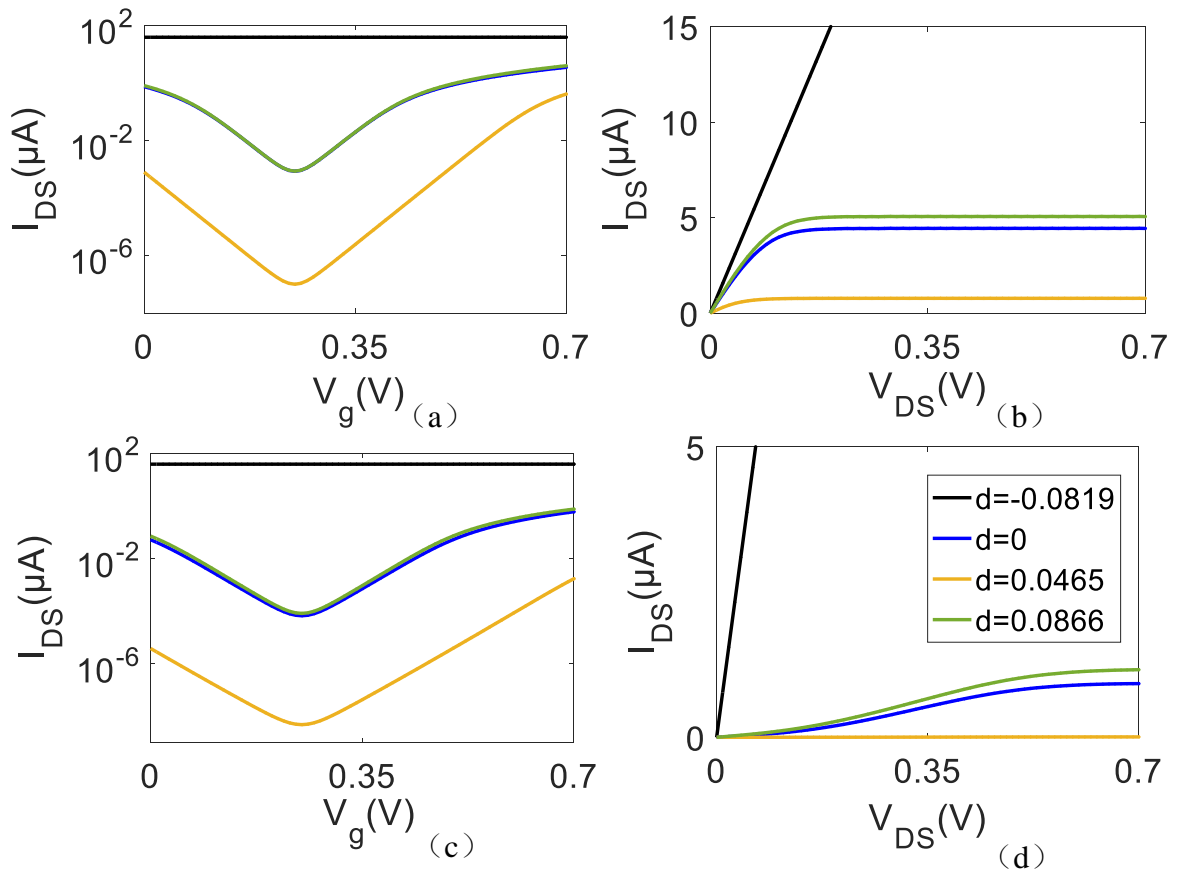


Figure 2.25: Number of atom for aGNR  $N=9$ , source-drain current  $I_{ds}$ . (a)  $I_{ds}$  vs.  $V_g$ , at  $V_{ds} = 0.5$  V with ohmic contacts. (b)  $I_{ds}$  vs.  $V_{ds}$ , at  $V_g = 0.75$  V with ohmic contacts. (c)  $I_{ds}$  vs.  $V_g$ , at  $V_{ds} = 0.5$  V with SB contacts. (d)  $I_{ds}$  vs.  $V_{ds}$ , at  $V_g = 0.75$  V with SB contacts. Considered deformations:  $d = -0.0819$  (black line),  $d = 0$  (blue line),  $d = 0.0465$  (yellow line),  $d = 0.0866$  (green line)

The same simulations have been performed for the case  $N=15$ , this time for the deformations of  $d = -0.0512$ ,  $d = 0$ ,  $d = 0.0278$ ,  $d = 0.053$  (shown explicitly in Figure 2.26) In Figure 2.26 the currents  $I_{ds}$  are computed, finding again similar currents for similar gap values.

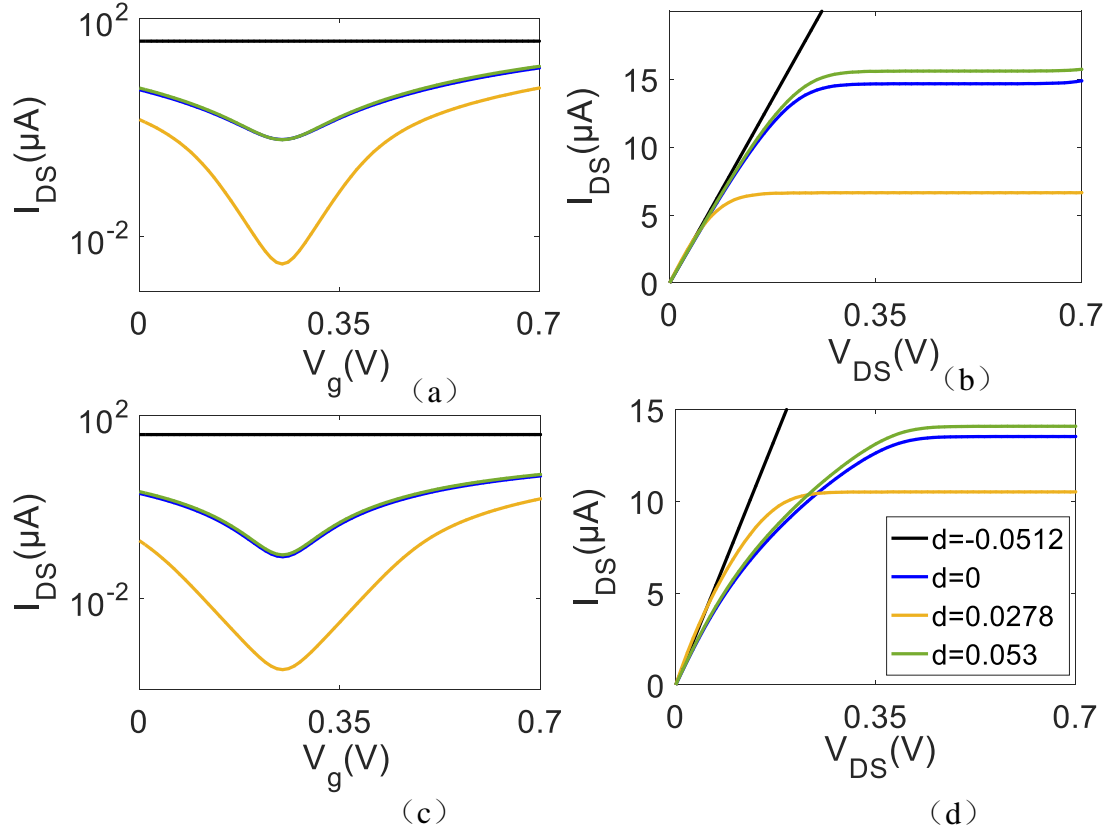


Figure 2.26: Number of atom for aGNR  $N=15$ , source-drain current  $I_{ds}$ . (a)  $I_{ds}$  vs.  $V_g$ , at  $V_{ds} = 0.5$  V with ohmic contacts. (b)  $I_{ds}$  vs.  $V_{ds}$ , at  $V_g = 0.75$  V with ohmic contacts. (c)  $I_{ds}$  vs.  $V_g$ , at  $V_{ds} = 0.5$  V with SB contacts. (d)  $I_{ds}$  vs.  $V_{ds}$ , at  $V_g = 0.75$  V with SB contacts. Considered deformations:  $d=-0.0512$  (black line),  $d=0$  (blue line),  $d=0.0278$  (yellow line),  $d=0.053$  (green line)

The results shown in Figure 2.25 and Figure 2.26 confirm the important impact of gap variation on the current level. They also show that the variations with respect to  $d$  are heavily dependent on the number  $N$  of atoms along the width of the aGNR. Furthermore, in all the cases we have verified that the transistor functioning are seriously affected if the energy gap is too small.

### 2.5.3 Partially Ballistic regime

In this paragraph, we show results concerning transistors in partially ballistic regime. In this hypothesis, the channel potential  $\phi_c$  varies along the channel. The transistor is then replaced with a cascade of  $N$  transistor,  $N$  being the number of mean-free paths contained in the channel [56][81][82]. The multiscale condition (1.35) is then replaced with a set of

multiscale conditions for each transistors, each condition involving a different sample of  $\phi_c$ , thus leading to the definition of a potential function of the position along the channel.

As Figure 2.27 shows, partially ballistic transistors can be regarded as a chain of ballistic transistors. Based on Büttiker virtual probe approach [81][82], scattering in the channel can be considered as localized in several special points, spaced by a length defined as “mean free path” [56].

A transistor with partially transport regime is connected by  $N_{\text{chain}}$  virtual probes with  $n = 1, \dots, N_{\text{chain}} - 1$ , where  $N_{\text{chain}}$  is number of ballistic transistors. For the boundaries, the electrochemical potential can be set as:

$$\begin{aligned}\mu_S &= -qV_S \\ \mu_D &= -qV_D\end{aligned}\tag{2.30}$$

As a first step in the calculation of the current, we enforce in the middle points between different ballistic transistors, an electrochemical potential is set as a linear variation between  $V_S$  and  $V_D$ . In the case  $V_S=0$ :

$$\mu_n = -qn V_D / N_{\text{chain}}\tag{2.31}$$

With  $n = 1, \dots, N_{\text{chain}} - 1$ . In the  $n$ th ballistic channel,  $\mu_n$  and  $\mu_{n-1}$  can be regarded as potential of the source and drain by using bisection method and numerical solution of (1.35) for  $\phi_c(x)$  can be obtained for every ballistic transistor in Figure 2.27. After we have the value of  $\phi_c(x)$ , then the current for each ballistic transistor can be calculated by using Landauer–Büttiker approach which shown in equation (1.20).

The current of  $I_n$  in any ballistic transistor is computed and we calculate the average of current of all the ballistic transistors:

$$I = \left( I_1 + I_2 + I_3 + \dots + I_{N_{\text{chain}}} \right) / N_{\text{chain}}\tag{2.32}$$

A non-linear system is then solved by enforcing that the same current flows through all the ballistic transistors. This leads to the determination of both the potential samples along the channel and the drain-source current.

In this paragraph, we study a partially ballistic regime with Ohmic contacts for a transistor whose length is three times the mean free path of electrons in the graphene. This choice of length allows observing the effects of a spatial variation of the potential along the channel. Due to the nanometric nature of graphene-based devices, a length of three mean-free paths (corresponding to around  $1.5 \mu\text{m}$  [83]) is a reasonable example of partially ballistic nanotransistor. The surface potential  $\phi_c$  assumes one value on each of them. These variations are shown in Figure 2.28 for  $V_{DS} = V_g = 0.5 \text{ V}$ . In Figure 2.29(a) and (b) we plot the  $I_{ds}$  for partially ballistic transistors with ohmic contacts, channel length of 3 mean free paths.  $I_{ds}$  is shown as a function of the relevant voltages. In Figure 2.29(a),  $I_{ds}$  is varied by keeping a constant potential  $V_{DS}$  and changing the gate potential  $V_g$ . In Figure 2.29(b),  $I_{ds}$  is varied by keeping a constant gate potential  $V_g$  and changing the drain-source potential  $V_{ds}$ . In the absence of deformation, the method also agrees with results in [56].

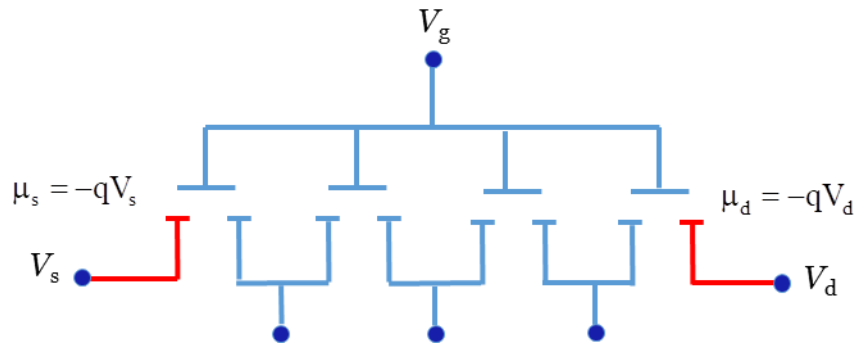


Figure 2.27: Partially ballistic transistor can be regarded as chain of  $N$  ballistic transistors.

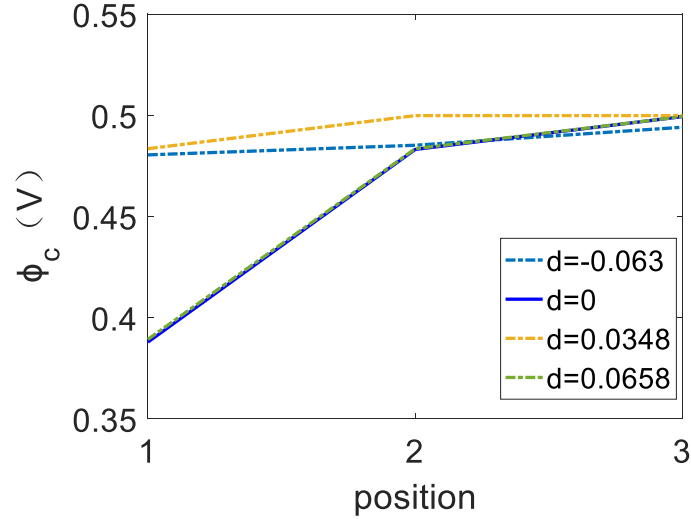


Figure 2.28: Potential  $\phi_c$  in a partially ballistic transistor with ohmic contacts, for different deformation.  $V_{ds} = V_g = 0.5$  V, channel length of 3 mean free paths. Considered deformations:  $d = -0.063$  (dashed light blue line),  $d = 0$  (solid dark blue line),  $d = 0.0348$  (yellow line),  $d = 0.0658$  (green line).

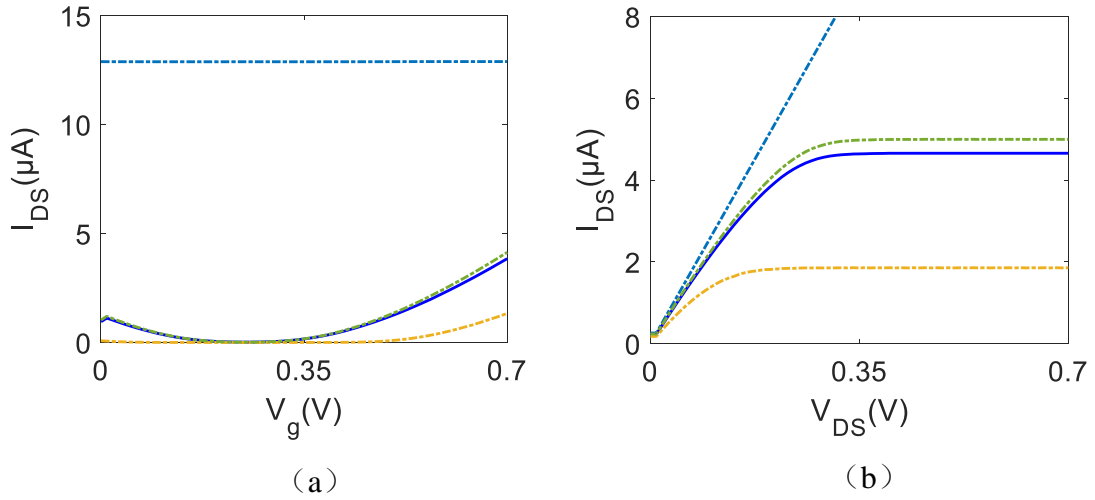


Figure 2.29:  $I_{ds}$  for partially ballistic transistors with ohmic contacts,  $N = 12$ , channel length of 3 mean free paths. (a)  $I_{ds}$  vs.  $V_g$ , at  $V_{ds} = 0.5$  V. (b)  $I_{ds}$  vs.  $V_{ds}$ , at  $V_g = 0.75$  V. Considered deformations:  $d = -0.063$  (dashed light blue line),  $d = 0$  (solid dark blue line),  $d = 0.0348$  (yellow line),  $d = 0.0658$  (green line).

Also in this case another nanoribbon with a different width has been studied. In Figure 2.30, the atoms along the aGNR width are 15. In Figure 2.30(a) and (b) we plot the  $I_{ds}$  for a channel length of 3 mean free paths, while in Figure 2.31 a channel length of 10 mean free

paths is chosen.

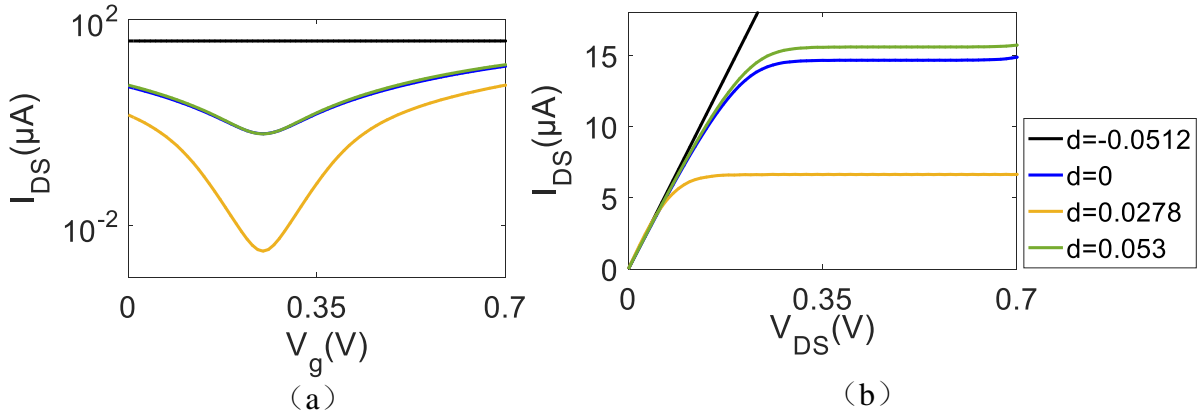


Figure 2.30:  $I_{ds}$  for partially ballistic transistors with ohmic contacts,  $N=15$ , channel length of 3 mean free paths. (a)  $I_{ds}$  vs.  $V_g$ , at  $V_{ds} = 0.5$  V. (b)  $I_{ds}$  vs.  $V_{ds}$ , at  $V_g = 0.75$  V. Considered deformations:  $d=-0.0512$  (black line),  $d=0$  (dark blue line),  $d=0.0278$  (yellow line),  $d=0.053$  (green line).

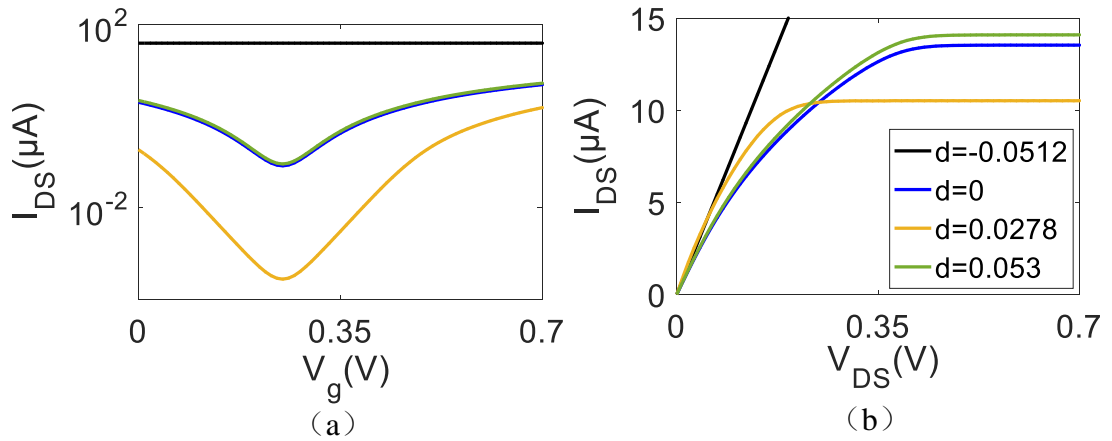


Figure 2.31:  $I_{ds}$  for partially ballistic transistors with ohmic contacts,  $N=15$ , channel length of 10 mean free paths. (a)  $I_{ds}$  vs.  $V_g$ , at  $V_{ds} = 0.5$  V. (b)  $I_{ds}$  vs.  $V_{ds}$ , at  $V_g = 0.75$  V. Considered deformations:  $d=-0.0512$  (black line),  $d=0$  (dark blue line),  $d=0.0278$  (yellow line),  $d=0.053$  (green line).

In both cases we observe that the same deformation has quite different effects on the performance of the nanotransistor according to the width of its ribbon. Again, some deformations can lead to small energy gaps, limiting the transistor performance.

#### 2.5.4 On/Off current ratio and differential conductance with different deformations

In Figure 2.32, we plot the On/Off current ratio for both ballistic and partially ballistic transistors with different deformations, whose atom number along the aGNR width direction is  $N=12$ . Figure 2.32(a) shows the On/Off current ratio for ballistic transistors. We can see that in the presence of a deformation of few percentage points, the On/Off current ratios can be modulated in a visible way and it can even achieve  $5 \cdot 10^4$  when  $d=0.034$ . We can deduce that the variation of current in ballistic FET could be used to detect deformations in nano-sensors.

Figure 2.32(b) shows On/Off current ratio for partially ballistic transistors which channel length is 3 mean free paths and Figure 2.32(c) shows On/Off current ratio for partially ballistic transistors which channel length is 10 mean free paths. As expected [56] the ratios are slightly larger in this latter transport regime with respect to the ballistic case. Also in this case, the On/Off current ratios are sensibly modified around the point  $d = 0$  for small deformations. From (2.19) we can state that larger widths of the nanoribbon present energy gaps that are more sensitive to deformations: as the width increases (the number of atoms  $N$  in (2.19)), it takes a smaller deformation to reach the point of zero gap. This means that the deterioration of the current ratio will occur with smaller deformation with respect to narrower nanoribbons.

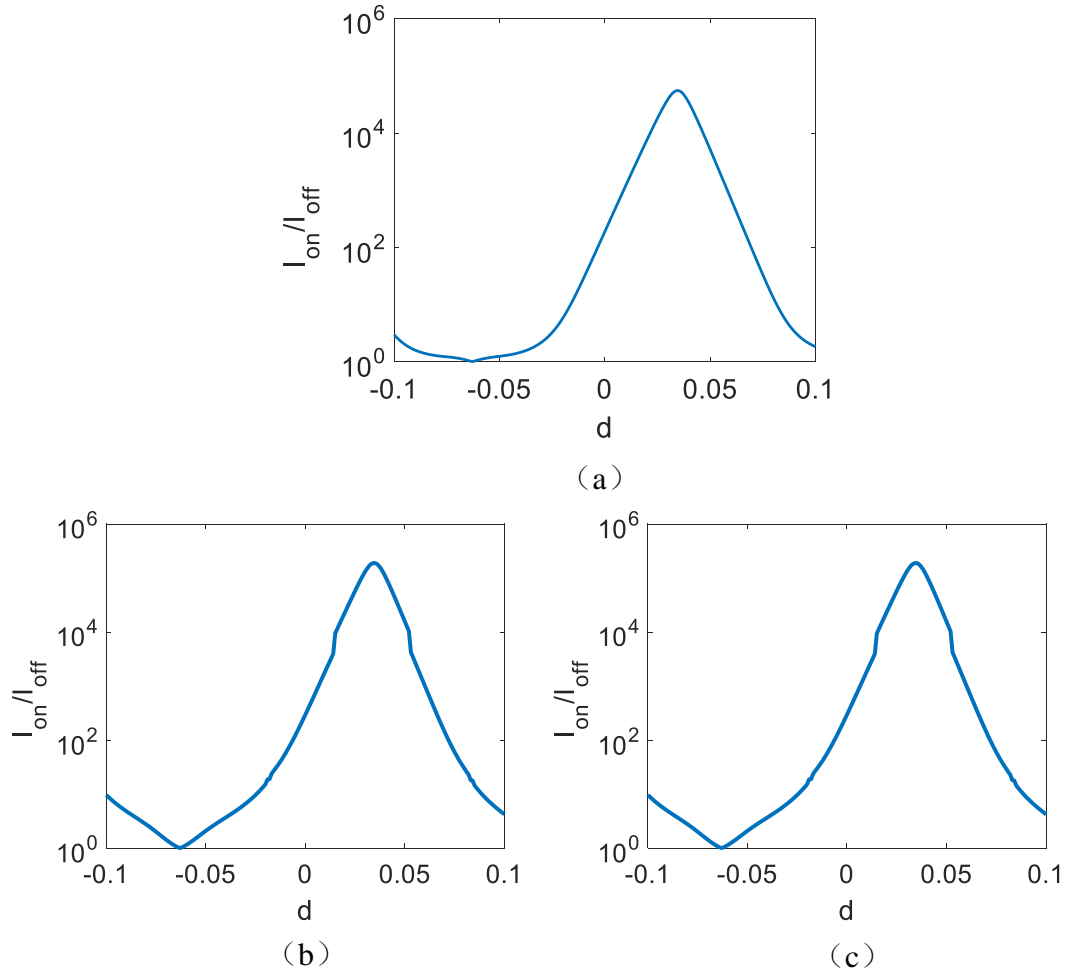


Figure 2.32: (a) On/Off current ratio of ballistic transistor for  $N=12$  with different deformations. (b) On/Off current ratio for partially ballistic transistors with ohmic contacts,  $N=12$ , channel length of 3 mean free paths. (c) On/Off current ratio for partially ballistic transistors with ohmic contacts,  $N=12$ , channel length of 10 mean free paths.

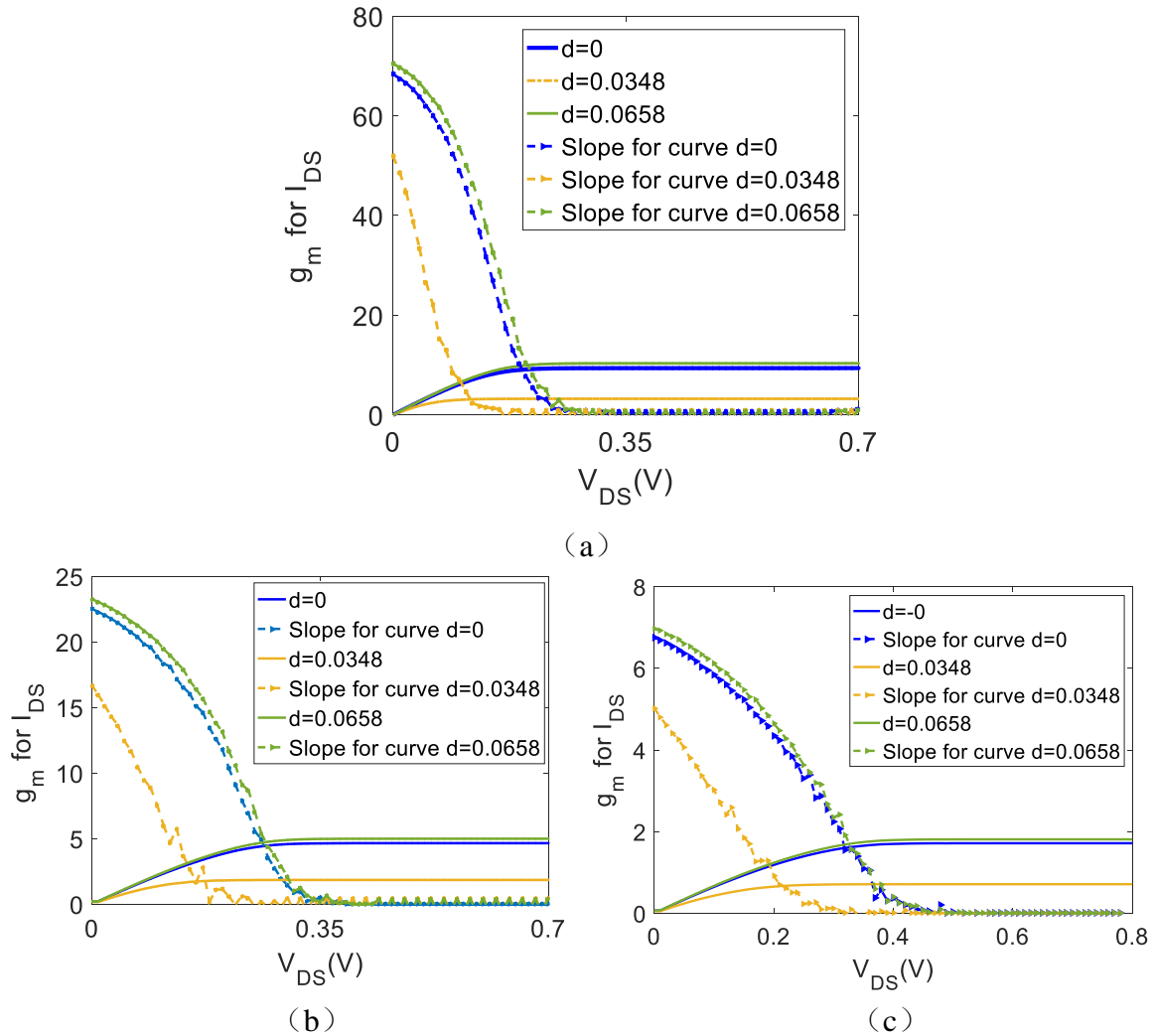


Figure 2.33: Differential conductance of aGNR FET with Ohmic contacts,  $N=12$ . (a) For ballistic transistor. (b) For partially ballistic transistors, channel length of 3 mean free paths. (c) For partially ballistic transistors, channel length of 10 mean free paths.

An accurate analysis of deformation effects on the output characteristics can also lead to the computation of the differential conductance  $g_m = \partial I_{ds} / \partial V_{ds}$ . In Figure 2.33(a), we compare  $g_m$  of three ballistic transistors for different deformations  $d=0$ ,  $d=0.0348$ ,  $d=0.0658$ . The differential conductance is varying slightly as long as  $d$  varies of a few percentage points. The linear region before saturation is also accordingly modulated. The differential conductance for  $d=-0.063$  becomes a flat straight line since the energy gap decreases to 0. For this reason the case is not explicitly shown here.

In Figure 2.33(b) and Figure 2.33(c), we compare the differential conductance of partially ballistic transistor for the same deformations. Similarly to Figure 2.33(a), the

differential conductance changes again with  $d$  in a similar qualitative way as in the ballistic case.

### 2.5.5 Shift of transfer characteristics with different SB height

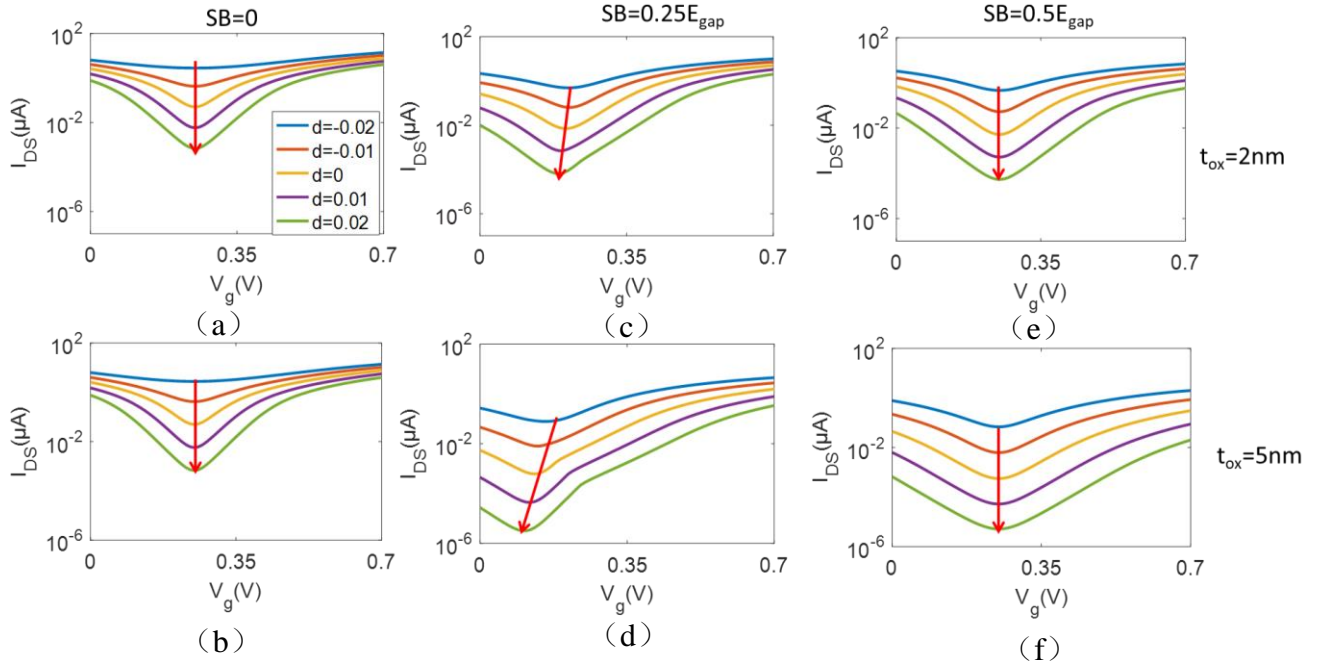


Figure 2.34: Transfer characteristics of aGNR FET with different oxide thicknesses  $t_{ox}$ ,  $V_{DS}=0.5$  V. Deformations simulated:  $d=-0.02, -0.01, 0, 0.01, 0.02$ . FET without SB (SB = 0) and with SBs of  $0.25E_g$  and  $0.5E_g$  are shown. Arrows represent the shift of transfer characteristics curves.

In Figure 2.34, we show also the transfer characteristics of aGNR FET with different oxide thickness  $t_{ox}$ . Different deformations  $d=-0.02, -0.01, 0, 0.01, 0.02$  are selected. In Figure 2.34(a) and (b), we keep SB height equals to 0 (ohmic contacts); in Figure 2.34(c) and (d), the SB height equals to  $0.25E_{gap}$ ; in Figure 2.34(e) and (f), the SB height equals to  $0.5E_{gap}$ .

From Figure 2.34, the  $I_{off}$  point and the shape of transfer characteristics are influenced by relative SB height. If SB height equals to 0 or  $0.5E_{gap}$ , the minimum OFF current point will shift vertically under the effect of a deformation, while if SB height equals to  $0.25E_{gap}$ , the minimum off current point will move sideways.

aGNR is one kind of electron–hole symmetrical materials. If the SB height equals to  $0.5E_{gap}$ , the electron hole symmetry is kept even under deformation, therefore the lowest point

of transfer characteristics (OFF state of current) moves vertically. If the SB height equals to  $0.25E_{\text{gap}}$ , the electron hole symmetry is broken, and the  $I_{\text{off}}$  moves sideways.

# Chapter 3. Application of Nanomesh in Field-Effect Transistor

In this chapter, the multiscale semi-analytic compact model presented in the previous Chapters is applied to graphene nanomesh transistors. As stated in Chapter 1 (Section 1.6), a bandgap can be induced in graphene-based structures with a variety of techniques. Here we study the effect of the inclusion of a nanomesh graphene in nano-transistors. The first part of the Chapter is focused on methods to estimate the energy gap of nanomesh, by means of analytical approximations or *ab-initio* approaches. These results are then used in the modelling of an entire FET, and the FET performance is compared with those of a nanoribbon FET having a similar size.

## 3.1 Graphene nanomesh and its electronic properties

Bandgap in graphene-based structures can be obtained by different methods. In Chapter 2, we have used graphene nanoribbons for this aim. Graphene nanoribbons with widths around 2-3 nm can open a band gap large enough for room temperature transistor operation, but processing graphene sheets less than 5 nm is still quite challenging. Namely, current manufacturing methods can lead to imperfect structures. However, another effective technique to tune bandgap is by creating an ordered array of holes with specific shape, size and density in the graphene plane [64]. The resulting structure is named graphene nanomesh. Fig 3.1 shows an example of circular hole graphene nanomesh [84].

As illustrated in Fig. 3.1(b), [84] mainly focuses on circular hole on graphene nanomesh. Holes of shape approximately circular are created on graphene and arranged in a periodic hexagonal lattice; the length of one side of the hexagonal unit-cell is  $L$ , and the radius of the hole is  $R$ .

In [84], Pedersen started from *ab-initio* simulations to find an approximate relation for the band gaps of circular-shaped GNH:

$$E_{\text{gap}} = K_{\text{GNM}} \frac{\sqrt{N_{\text{hole}}}}{N_{\text{total}}} \quad (3.1)$$

where  $N_{\text{hole}}$  is the number of atoms removed in the holes and  $N_{\text{total}}$  is the total number of atoms present in the sheet before removing the hole.

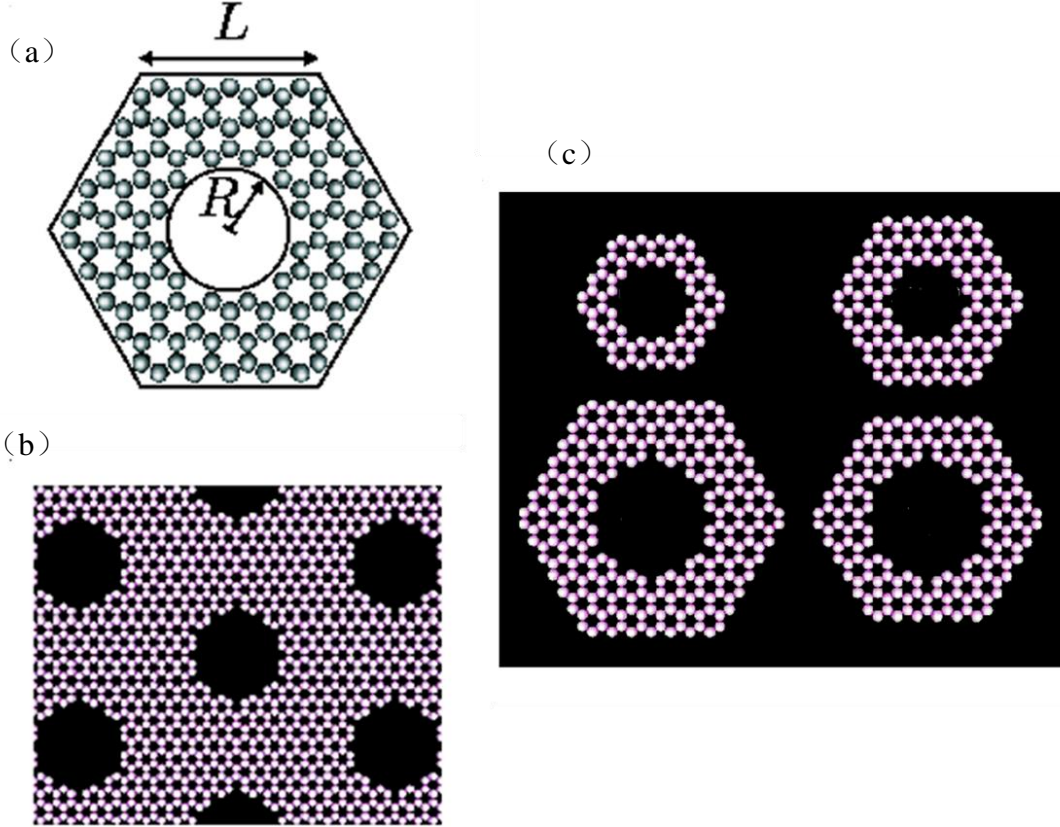


Figure 3.1: Schematic illustration of Graphene Nanomesh (a) Shape of nanomesh (b) Unit cell of nanomesh, side length  $L$ , hole radius  $R$  (c) several examples with different  $L$  and  $R$  [84].

The  $K_{\text{GNM}}$  constant is found by means of a fitting method, leading to  $K_{\text{GNM}} \approx 25 \text{ eV}$ .

After Pedersen, many interesting researches are proposed to study the electronic characteristics of graphene nanomesh [85]-[88]. In [85], H. Jippo et al. studied the full electronic structure and transport properties of graphene nanomesh lattices. Their results confirmed that graphene nanomesh can control the band gap and has the potential to be used as channel material in transistor. In [86], Y. Yan et al. investigated the thermoelectric properties of graphene nanomesh of 1D graphene antidot arrays with zigzag edges by using the nonequilibrium Green's function method. Their numerical results indicate that graphene

nanomesh may be promising for thermoelectric applications. In [87], V. H. Nguyen et al. investigated the transport characteristics of graphene nanomesh-based devices. Nguyen's research shows that graphene nanomesh offers various possibilities for a controllable energy bandgap by changing the nano-hole size [88]. In [88], Nguyen also considered the application of graphene nanomesh for electronic devices.

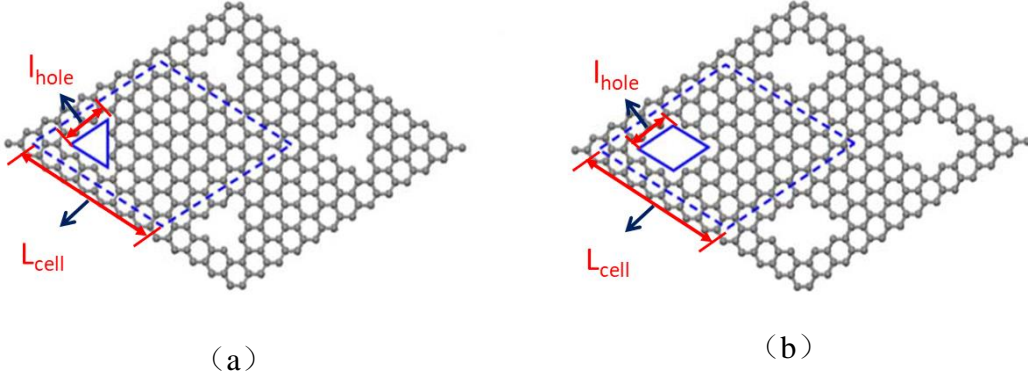


Figure 3.2: Schematic illustration of Graphene Nanomesh (a) Graphene nanomesh with triangular holes (b) Graphene nanomesh with rhombic holes [89].

The scaling rule (3.1) only works well for the circular shape holes. In [89], Liu et al. studied how the energy gap of graphene nanomesh is related with the shape of the hole (either armchair or zigzag edges). The following scaling rule for the bandgap is there proposed [89]:

$$E_{\text{gap}} \approx \lambda_{\text{GNM}} \frac{l_{\text{hole}}}{(L_{\text{cell}})^2} \quad (3.2)$$

where  $l_{\text{hole}}$  is the side length of the hole,  $L_{\text{cell}}$  is the side length of the unit cell as Figure 3.2 shows.

The parameter  $\lambda_{\text{GNM}}$  is obtained by fitting method and its value depends on the shape and edge type of graphene nanomesh hole. In Table 3.1 we report some values obtained in [89] for different geometries.

Table 3.1 Value of  $\lambda_{GNM}$  [89].

$\lambda_{GNM}$ (eV)	$E_{\text{gap}}$		
	$3n-2$	$3n-1$	$3n$
Length of the hole			
Armchair triangular graphene nanomesh	6.99	14.42	23.97
Armchair rhombus graphene nanomesh	14.63	24.59	6.78
Zigzag triangular graphene nanomesh		12.39	
Zigzag rhombus graphene nanomesh		6.72	

From the scaling rule (3.2) and the numerical values in Table 3.1, we can calculate the band gaps for different types of graphene nanomesh. The results are shown in Figure 3.3- Figure 3.4. In Figure 3.3, we show band gaps for different shapes and edge-type of graphene nanomesh with respect to the graphene nanomesh unit-cell side length. In this figure we keep the side length of the hole constant with 17 carbon atoms for each side. As expected, the energy gap always decreases as the unit cell length  $L$  increases. In fact, this corresponds to a decrease of the hole density, so that the zero gap of a graphene sheet is approached.

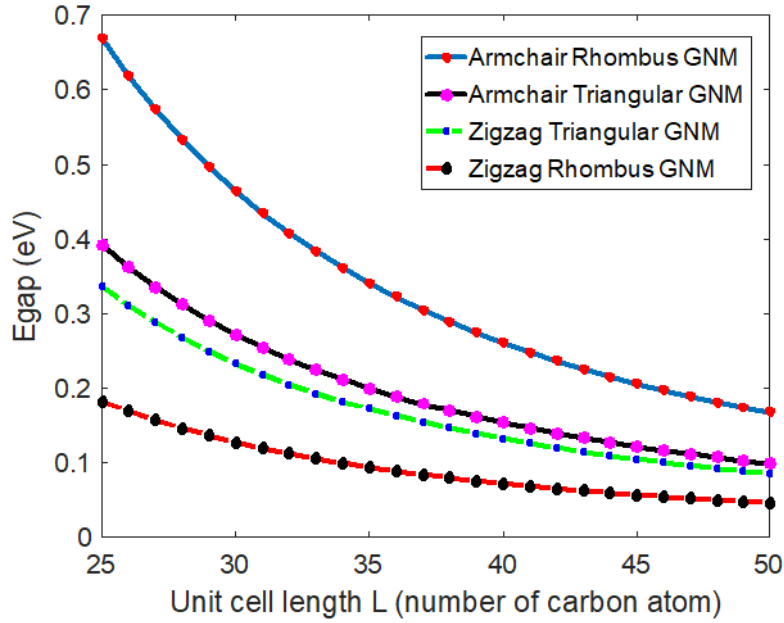


Figure 3.3: Energy gap of different shape graphene nanomesh, in unit cell, side length of the hole=17 carbon atom.

In Figure 3.4, band gaps for armchair rhombus nanomesh and armchair triangular nanomesh are plotted vs. the length of the unit-cell, for two different hole sizes (14 and 20, respectively).

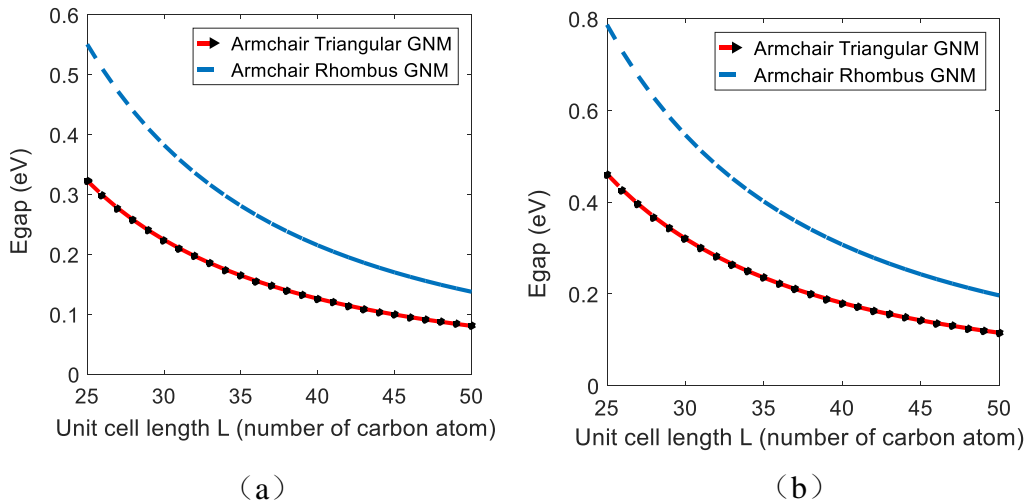


Figure 3.4: (a) Energy gap of different shape graphene nanomesh, in unit cell, side length of the hole=14 carbon atom. (b) Energy gap of different shape graphene nanomesh, in unit cell, side length of the hole=20 carbon atom.

Once we have a method to evaluate the energy gap of a nanomesh, we can study charge transport in nanomesh transistors.

### 3.2 Compact model validation with *ab-initio* method

As discussed in Chapter 2, graphene nano-transistors can be realized by means of armchair nanoribbons whose width is less than 2 or 3 nm, assuring the presence of an energy gap. However, the control of width and edge shape is still a difficult task for current fabrication procedures. A new field effect transistor which uses nanomesh as channel is proposed in [64]. The on-off current ratio of graphene nanomesh transistor can be enhanced by up to 10 times if compared pristine graphene transistor, thus obtaining results comparable with GNRs.

Once the electronic properties of graphene nanomesh are determined, such as the energy gap discussed previously, the currents of the FET shown in Figure 3.5 can be calculated by using the compact model described in Chapter 1 and used in Chapter 2.

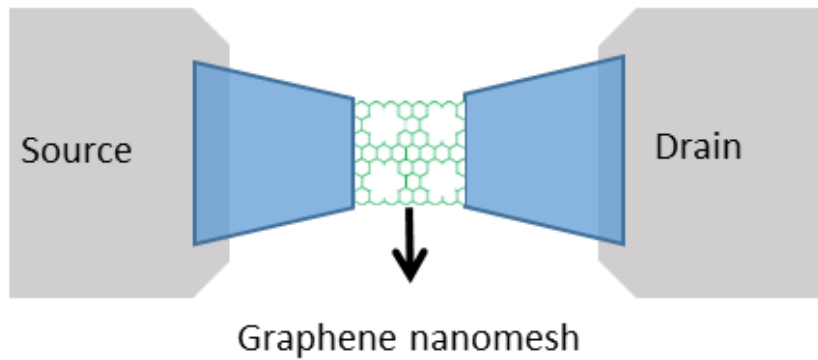


Figure 3.5: Nanomesh graphene transistor

Our graphene nanomesh channel structure is shown in Figure 3.6. The shape of the graphene nanomesh channel is a square whose side length is  $W_{\text{gnm}}$  of the square is 9 nm. 9 evenly distributed squared holes are arranged in a rectangular array, and the side length ( $l_{\text{r-hole}}$ ) of each hole is 2 nm, and the edge shape of the hole is of armchair type. The distance between each hole ( $d_{\text{r-hole}}$ ) is 1 nm.

By knowing the geometric structure of nanomesh, the energy gap can be calculated by using (3.2) and the parameter  $\lambda_{\text{GNM}}$  in Table 3.1. In this first case, the hole is of rhombic

shape and  $\lambda_{\text{GNM}}$  can be determined as 24.59 eV. The resulting energy gap is then about 0.67 eV. In order to obtain an independent validation of this approximate formula, we have compared  $E_{\text{gap}}$  with the result given by an *ab-initio* formulation [90]. For *ab-initio* formulation, the energy gap for this structure is about 0.66 eV (see Figure 3.7), in good agreement with the approximate value.

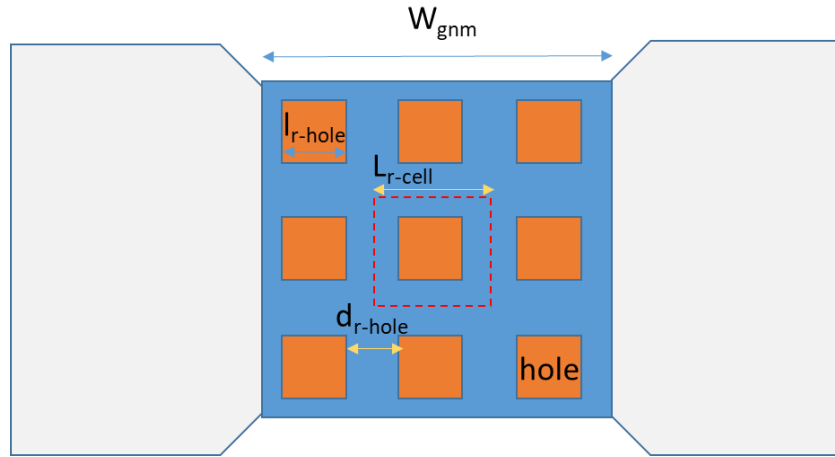


Figure 3.6: The shape of Graphene Nanomesh in transistor.

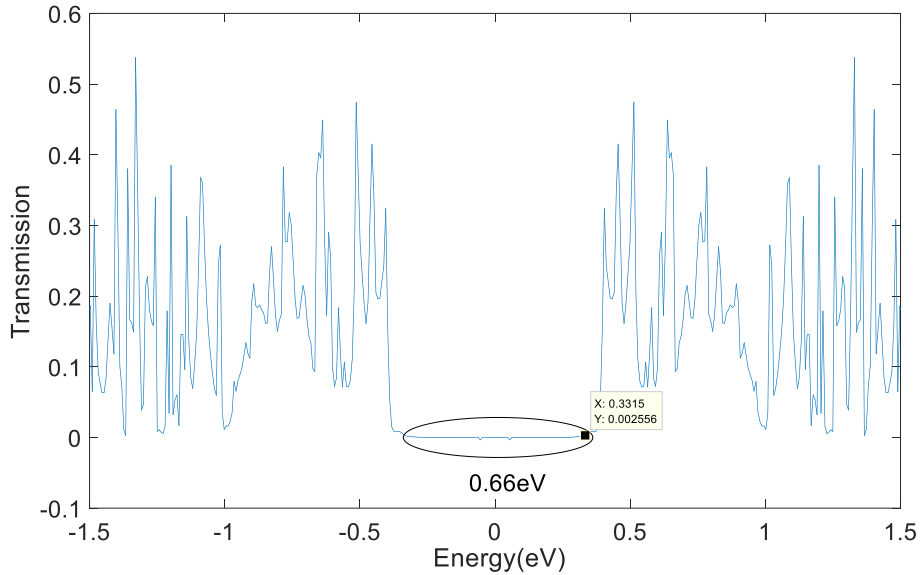


Figure 3.7: Transmission versus energy for a sample of 9 nm x 9 nm, from Fernando Zanella, Federal University of Paraná (UFPR).

As verified in the previous Chapter, the energy gap of the channel is the most important parameter determining the result of our calculation. In this Chapter, the energy gap

is chosen by using the closed-form expression (3.2). However, the energy gap obtained refers only to the lower energy band of the channel. Unfortunately, no analytic approximations are available for higher energy bands of nanomesh graphene. In order to keep the formulation as simple as possible, we will consider therefore only the fundamental band. Its shape is assumed as a parabolic curve (see Figure 3.8(b)) as in, and as confirmed by *ab-initio* simulations shown in literature [89]. Since here we do not deal with deformations, non-null values of energy gaps will be only considered, and the limit of small gaps discussed in Section 2.2 is not relevant. However, a last comment should be given regarding the shape of the energy band. Since no analytic expressions for the effective mass of the nanomesh are available in the literature to the best of our knowledge, the nano-mesh energy gap will be used in the analytic expressions of the density of state already derived for 1-D nanoribbon. The influence of the effective mass has been studied with a parametric analysis by varying this parameter in a range of values of the same order of magnitude of the nanoribbons of Chapter 2. As expected, the mass variation has a weak influence on the current if compared to the stronger influence due to the variation of the energy gap obtained with the removal of atoms. Since in this chapter we are especially interested in the comparison between on/off current ratios in nanoribbon and nanomesh, the same effective mass will be retained for the two devices. However, further work is planned in order to improve the description of the density of state and of the higher energy band on the basis of *ab-initio* simulations.

Finally, we assume that the width of the nanomesh is small enough to grant a one-dimensional conduction in the direction source-drain. This lead to the use of the same model used in Chapter 2 for nanoribbon graphene. The microelectronic model of graphene nanomesh transistor is in fact be expressed by the formula (1.25) where the sum over all the energy bands is suppressed and ohmic contacts have been considered for simplicity:

$$Q_{micro}^{e/h}(\phi_c) = q \int_0^{E^{max}-E(0)} \left[ f(\eta_s^{e/h}) + f(\eta_d^{e/h}) \right] D(E) dE \quad (3.3)$$

and the currents can be calculated as in (1.20), where again only one band is retained:

$$I_{e/h}(\phi_c) = \frac{q}{\pi \hbar} \int_0^{E^{max}-E(0)} \left[ f(\eta_s^{e/h}) - f(\eta_d^{e/h}) \right] dE$$

$$I = I_e - I_h \quad (3.4)$$

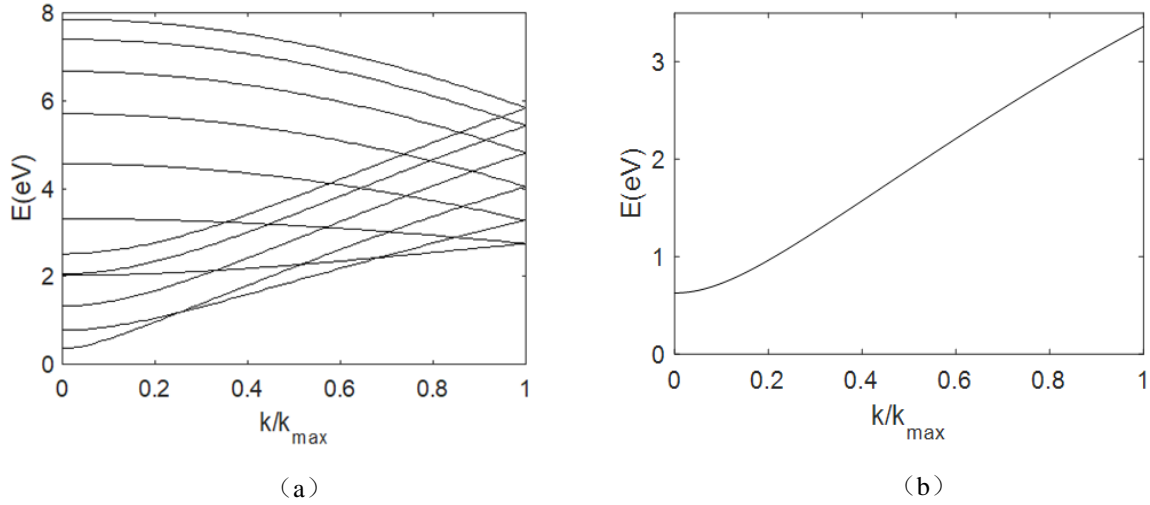


Figure 3.8: (a) Energy dispersion of graphene nanoribbon. (b) Illustration of energy dispersion of graphene nanomesh.

The capacitance of the gate for nanomesh transistor can be calculated as explained in Chapter 1. Once this value is computed, the capacitance of the source and drain can be calculated with the commonly used rule [56]:

$$C_s = C_d = 0.005C_g \quad (3.5)$$

In Figure 3.9 we plot the currents  $I_{ds}$  vs. the drain-source potential  $V_{ds}$  when by keeping a constant gate potential  $V_g = 0.75$  V. The following simulations have been performed by assuming Ohmic contacts in order to limit the number of results and the parameters under study. However, the method can be easily used to study Schottky barriers as shown in Chapter 2.

In order to validate the analysis, we have compared this current with the results given by the *ab-initio* formulation as Figure 3.9 shows. It can be seen that the comparison shows a very good agreement for low values of  $V_d$ . For higher values of  $V_d$  the compact model slightly underestimates the current.

In Figure 3.10(a), we plot the currents  $I_{ds}$  for nanomesh transistor vs.  $V_g$ , by keeping a constant potential  $V_{DS} = 0.5$  V. The simulation result shows an on-off current ratio close to 28 by choosing an on state for  $V_{DS} = 0.5$  V.

In Figure 3.10(b) we plot the variation of the channel potential  $\phi_c$  with different voltage excitation. Ohmic contacts are considered, and  $\phi_c$  is computed when the gate potential  $V_g$  is varied.

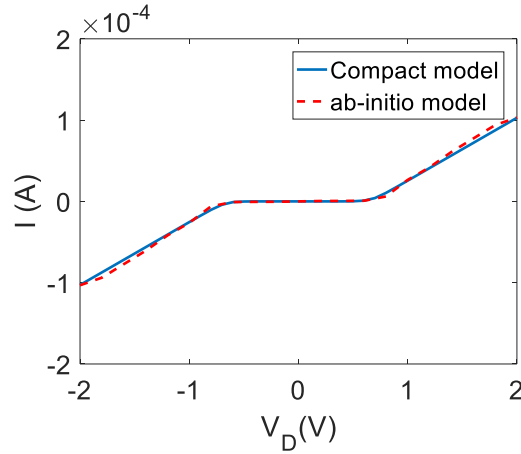


Figure 3.9: Source-drain current  $I_{ds}$ .  $I_{ds}$  vs.  $V_{ds}$ , at  $V_g = 0.75$  V.  $I_{ds}$  vs.  $V_g$ , at  $V_g = 0.75$  V. Different Models: Compact model (blue line), Ab-initio model (red line).

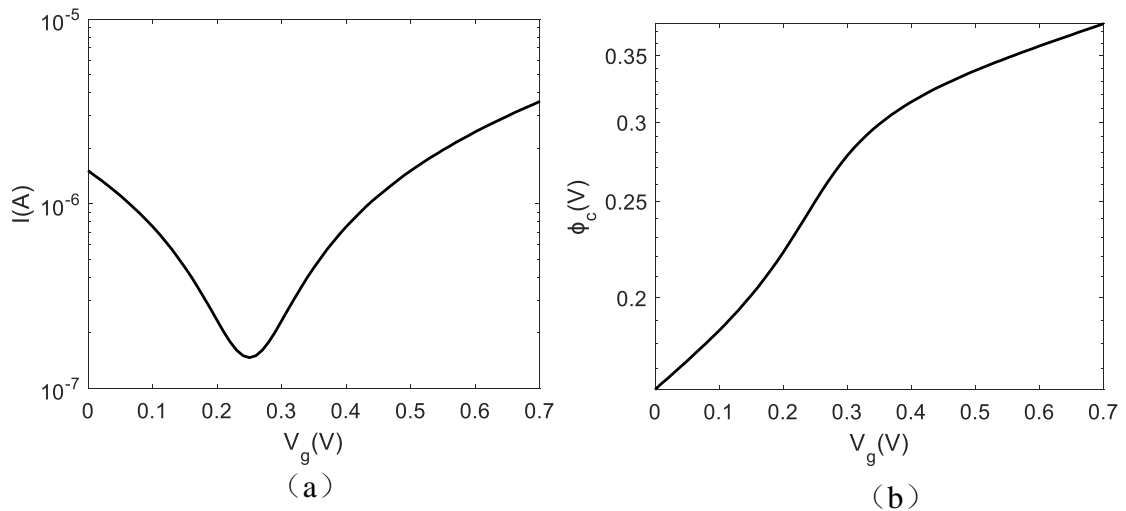


Figure 3.10: (a) Source-drain current  $I_{ds}$ ,  $I_{ds}$  vs.  $V_g$ , at  $V_{ds} = 0.5$  V (b)  $\phi_c$  vs.  $V_g$ , at  $V_{ds} = 0.5$  V.

Figure 3.11 is a plot of the current vs. gate voltage characteristics of the same device at different drain source voltages. The on-off current ratio are also changed for different drain-source voltages in the interval  $0 - 1$  V.

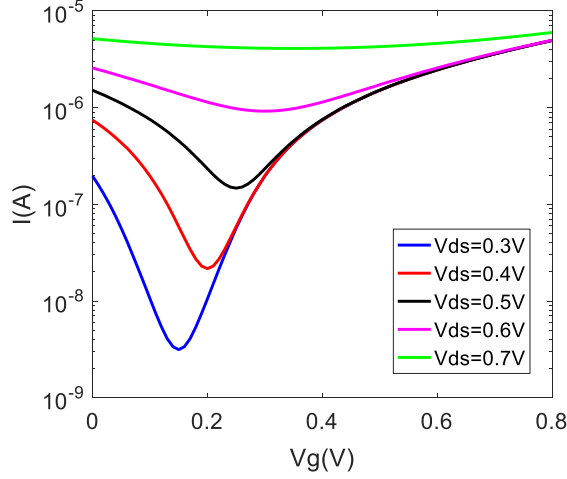


Figure 3.11: Source-drain current  $I_{ds}$ .  $I_{ds}$  vs.  $V_g$ , with different  $V_{ds}$

In Figure 3.12 we plot the variation of the channel potential  $\phi_c$  in different voltage excitation. In Figure 3.12 Ohmic contacts are considered, and  $\phi_c$  is computed when the gate potential  $V_g$  is varied. The drain-source current  $V_{ds}$  keep as a constant for every curve, the value of  $V_{ds}$  are selected as 0.3V, 0.4V, 0.5V, 0.6V, 0.7V respectively.

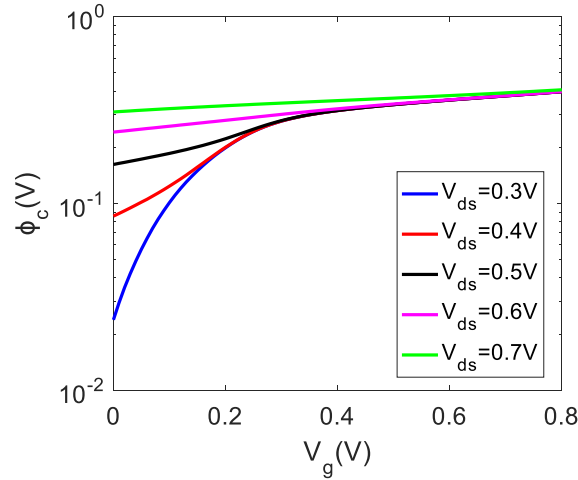


Figure 3.12:  $\phi_c$  vs.  $V_g$ , for different  $V_{ds}$ .

### 3.3 Graphene nanomesh transistor and its $I$ - $V$ characteristics

In order to investigate the impact of  $I$ - $V$  characteristics of nanomesh-based transistors, we test different shapes of nanomesh, namely rhombic and triangular shapes with different geometric parameters.

Table 3.2 Structures for different armchair rhombus graphene nanomesh samples used in FET.

$$\lambda_{GNM} = 24.59 \text{ in all these cases.}$$

<b>Armchair rhombus graphene nanomesh</b>			
Nanomesh Sample	Side length of the hole ( $l_{r\text{-hole}}$ ) (unit: nm)	Distance between each hole ( $d_{r\text{-hole}}$ ) (unit: nm)	Energy gap (unit: eV)
No.1	2	1	0.67
No.2	2	2	0.3616
No.3	2	3	0.2370
No.4	2	4	0.1672
No.5	2	5	0.1243

In Table 3.2 five nanomesh samples are considered, having holes of rhombic shape with armchair edges. Each sample has a squared hole of size  $l_{r\text{-hole}} = 2$  nm. According to the sample, different squared unit-cells have been chosen, so that the distance between holes ( $d_{r\text{-hole}}$ ) ranges from 1 nm to 5 nm. The value of  $\lambda_{GNM}$  depends on the shape and edge type of the hole, so that it is always the same for all these samples: it can be determined as 24.59 eV from Table 3.1, leading to energy gaps ranging from 0.67 eV to 0.1243 eV according to the dimension of the unit cell. Figure 3.13 is a plot of the current vs. gate voltage characteristics of Nanomesh sample No. 2 - No. 5 at different drain-source voltages.

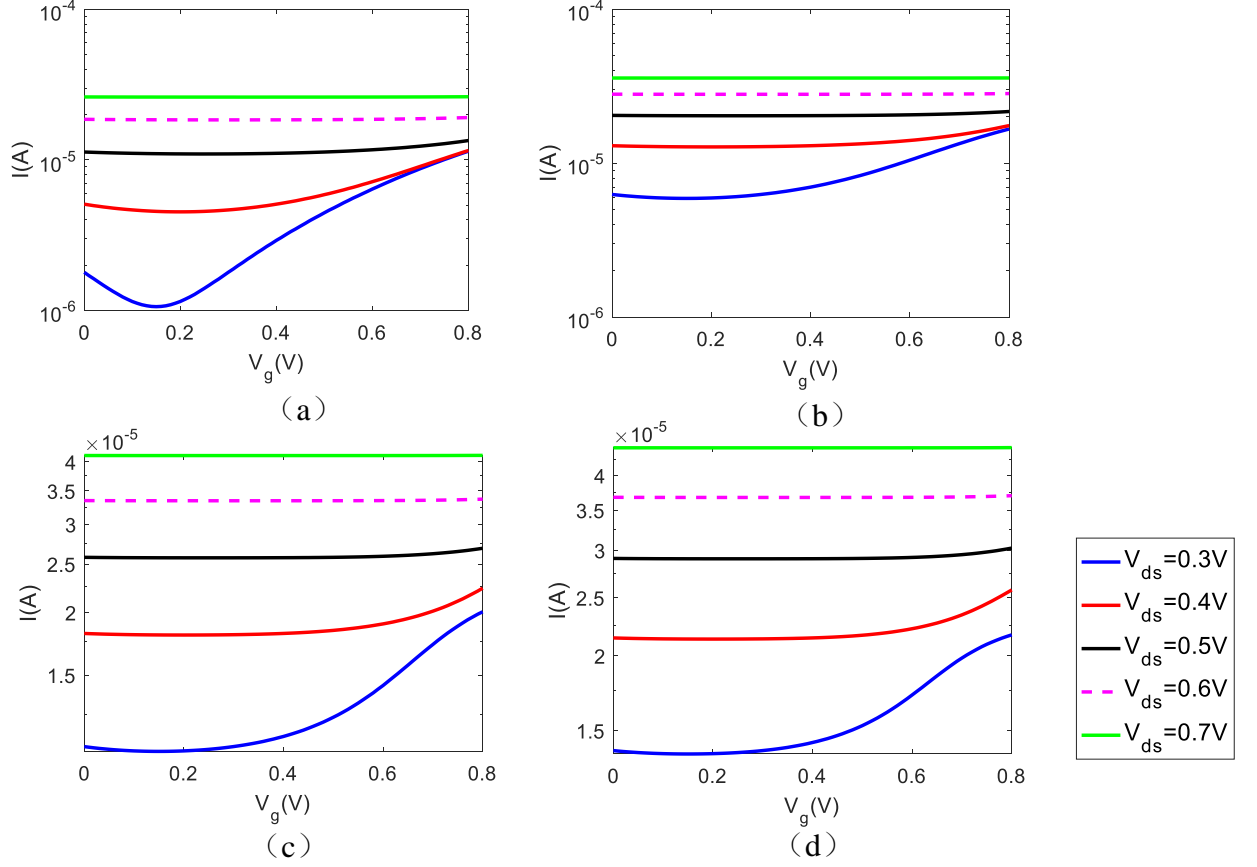


Figure 3.13: Source-drain current  $I_{ds}$  vs.  $V_g$ , with different  $V_{ds}$  for the nanomesh samples in Table 3.2. (a) Sample no. 2, (b) Sample no. 3, (c) Sample no. 4, (d) Sample no. 5.

We can see that the  $I_{on}/I_{off}$  ratios of different nanomesh transistors are strongly dependent on the lattice dimensions, i.e. on the mutual distance between holes. As the distance becomes large, (Figure 3.13(c) and (d)), the hole density is too small to obtain an effective energy gap, and the  $I_{on}/I_{off}$  deteriorates fast.

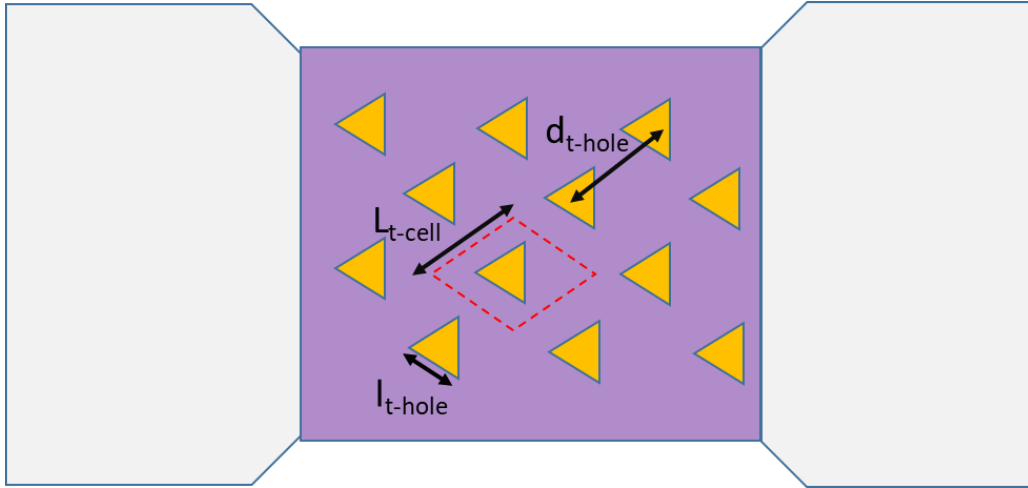


Figure 3.14: Triangular graphene nanomesh in transistor

We analyze now the same nanomesh lattice but we change the shape of each hole. Nanomesh samples No. 6 - No. 7, described in Table 3.3 are both triangular of armchair-type. The mutual distance between holes ( $d_{t-hole}$ ) is varied from 6 nm to 7 nm in the two samples. From Table 3.1, the value of  $\lambda_{GNM}$  is 23.97, leading to the energy gaps of 0.4027 eV and 0.2993 eV respectively. Figure 3.15(a) and (b) show the current vs. gate voltage characteristics of these two samples for different drain-source voltages.

Table 3.3 Structures of armchair triangular graphene nanomesh samples used in FET

<b>Armchair triangular graphene nanomesh</b>				
Nanomesh Sample	Side length of the hole ( $l_{t-hole}$ ) (unit: nm)	Distance between each hole ( $d_{t-hole}$ ) (unit: nm)	Fitting Parameter $\lambda_{GNM}$	Energy gap (unit: eV)
No.6	5	6	23.97	0.4027
No.7	5	7	23.97	0.2993

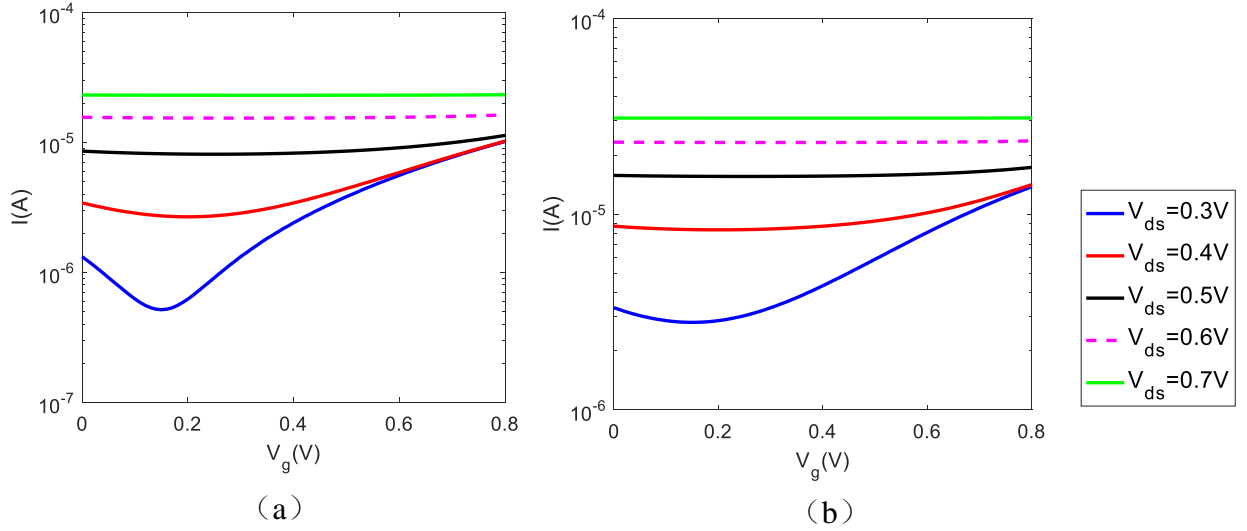


Figure 3.15: Armchair triangular graphene nanomesh FET: Source-drain current  $I_{ds}$  vs.  $V_g$ , with different  $V_{ds}$ . (a) Sample No. 6. (b) Sample No. 7.

Table 3.4 Structures of Zigzag triangular graphene nanomesh samples used in FET

<b>Zigzag triangular graphene nanomesh</b>				
Nanomesh Sample	Side length of the hole ( $l_{t-hole}$ ) (unit: nm)	Distance between each hole ( $d_{t-hole}$ ) (unit: nm)	Fitting Parameter $\lambda_{GNM}$	Energy gap (unit: eV)
No.8	2	3	12.39	0.337
No.9	2	4	12.39	0.1822

In Table 3.4, we analyze two nanomesh samples having holes with a zigzag edge, again of triangular shape. Again, distance between holes ( $d_{t-hole}$ ) is varied, the two values 3 nm and 4 nm being chosen. The value of  $\lambda_{GNM}$  corresponding to this geometry is 12.39, leading to the energy gaps of 0.337 eV and 0.1822 eV. Notice that with triangular holes zigzag edges lead to a  $\lambda_{GNM}$  smaller than the armchair type. In order to obtain energy gaps comparable to those of Figure 3.3, a denser lattice has been chosen in Table 3.4. Figure 3.16 show also in this case the current vs. the gate voltage of these transistors, confirming the importance of both the geometrical features of the lattice and of the edge properties of each hole on the  $I_{on}/I_{off}$  ratio.

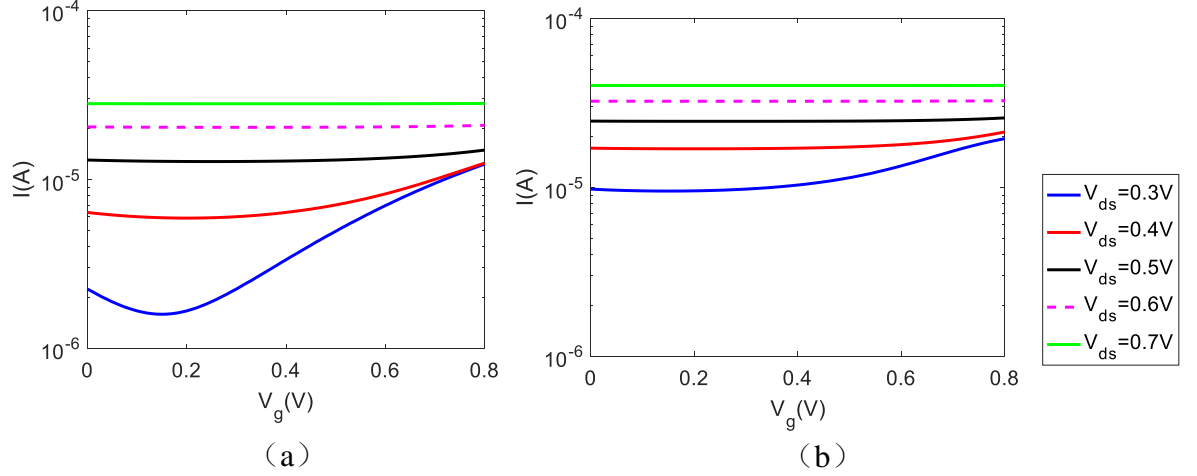


Figure 3.16: Zigzag triangular graphene nanomesh : Source-drain current  $I_{ds}$ ,  $I_{ds}$  vs.  $V_g$ , with different  $V_{ds}$ . (a) Sample No. 8. (b) Sample No. 9.

All previous results show the importance of keeping a dense mesh in order to grant a satisfactory on/off current ratio. As the holes get further the nanomesh approaches fast the behavior of a graphene sheet and the current ratio is degraded. This is described by the factor  $\frac{l_{hole}}{(L_{cell})^2}$  in (3.2), giving low energy gaps if  $L_{cell}$  becomes large even if  $l_{hole}$  grows proportionally. Furthermore, even if the nanomesh lattice is fixed, the shape of each hole can limit the performance of the FET, according to the different values of the  $\lambda_{GNM}$  factor in (3.2).

### 3.4 Numerical and experimental study of graphene nanomesh transistor

In the previous paragraphs, we have used available approximations for energy gaps of nanomesh graphene to analyze the characteristics of GFETs. The numerical results have been successfully tested with an *ab-initio* approach. In this last paragraph, we address a partial verification with experimental results performed at the L2E laboratory in cooperation with Prof. D. Brunel and Ph.D student J. Njeim.

Graphene monolayer has been successfully grown on top of a copper layer using chemical vapor deposition [91]. Raman spectroscopy has been used on every step of the fabrication in order to confirm the presence of monolayers and to continuously control the presence of defects.

The FET substrates are 285 nm thick  $\text{SiO}_2$  grown on the top of p-doped silicon.

Electron beam lithography techniques have been used to fabricate FETs with different dimensions [92]. Three different transistors are here considered, with three different channel sizes. The graphene channels were squares of  $1\ \mu\text{m} \times 1\ \mu\text{m}$ , of  $2\ \mu\text{m} \times 2\ \mu\text{m}$ . and of  $3\ \mu\text{m} \times 3\ \mu\text{m}$  respectively. Electrical measurements have been performed by using a semiconductor analyzer at room temperature.

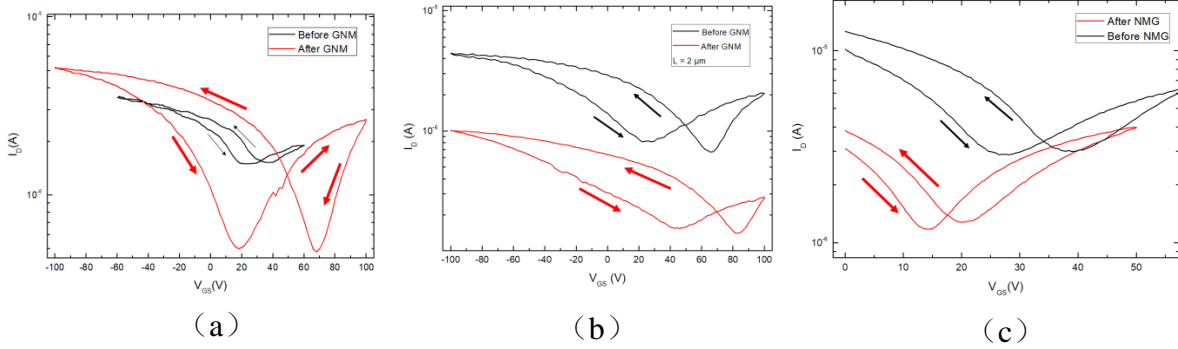


Figure 3.17: Source-drain current  $I_D$  in the experimental results at L2E, Sorbonne University. (a) transistor No. 1,  $1\ \mu\text{m}$  transistor. (b) transistor No. 2,  $2\ \mu\text{m}$  transistor. (c) transistor No. 3,  $3\ \mu\text{m}$  transistor.

For the first transistor (for clarity of description, we will call it transistor No. 1), a  $1\ \mu\text{m} \times 1\ \mu\text{m}$  square channels was designed by using reactive ion etching [92]. In Figure 3.17(a),  $I_D$  is varied by keeping a constant potential and changing the gate potential  $V_g$ . The black curve represents a reference of the same size as Transistor No. 1, but whose channel is rectangular graphene sample without any holes on it. The nanomesh is a matrix made of holes of size  $100\ \text{nm} \times 100\ \text{nm}$  having mutual distance of  $100\ \text{nm}$ . This correspond to the geometry in Figure 3.6, with physical parameters  $W_{\text{gnm}} = 1\ \mu\text{m}$ ,  $l_{\text{r-hole}} = 100\ \text{nm}$ ,  $L_{\text{r-cell}} = 200\ \text{nm}$ ,  $d_{\text{r-hole}} = 100\ \text{nm}$ . As expected, the experiment confirms that the nanomesh-based transistor shows improved on-off current ratio if compared with the reference graphene transistor.

For the second transistor (we will call it here transistor No. 2), a  $2\ \mu\text{m} \times 2\ \mu\text{m}$  square channel is used. In Figure 3.17(b),  $I_{\text{DS}}$  is varied by keeping a constant potential and changing the gate potential  $V_g$ . The black curve shows the characteristic of a transistor without any holes in the graphene channel. The red curve is a transistor with a nanomesh channel. This nanomesh is composed with holes of size  $150\ \text{nm} \times 150\ \text{nm}$  at mutual distance of  $150\ \text{nm}$ . As in Figure 3.6, these dimensions are:  $W_{\text{gnm}} = 2\ \mu\text{m}$ ,  $l_{\text{r-hole}} = 150\ \text{nm}$ ,  $L_{\text{r-cell}} = 300\ \text{nm}$ ,  $d_{\text{r-hole}} = 150\ \text{nm}$ .

For the third transistor (we will call it transistor No. 3), a  $3\ \mu\text{m} \times 3\ \mu\text{m}$  square channel is used. In Figure 3.17(c),  $I_{\text{DS}}$  is varied by keeping a constant potential and changing the gate potential  $V_g$ . Again a comparison is shown between a nanoribbon transistor (black curve) and a nanomesh transistor (red curve). The black curve represents  $I$ - $V$  characteristics of transistor No. 3 whose channel is a rectangular-shaped graphene without any holes on it, the dimension of the channel is  $3\ \mu\text{m} \times 3\ \mu\text{m}$ . The red curve represents  $I$ - $V$  characteristics of transistor No. 3 whose channel is a graphene nanomesh. The nanomesh is composed of  $200\ \text{nm} \times 200\ \text{nm}$  squared holes at mutual distance of  $150\ \text{nm}$ , corresponding to the following parameters in Figure 3.6:  $W_{\text{gnm}} = 3\ \mu\text{m}$ ,  $l_{\text{r-hole}} = 200\ \text{nm}$ ,  $L_{\text{r-cell}} = 350\ \text{nm}$ ,  $d_{\text{r-hole}} = 150\ \text{nm}$ .

In Figure 3.17(b) and Figure 3.17(c), nanomesh transistors do not show an improvement of the on-off current ratio if compared with reference graphene transistors. The different electric behavior among these transistors depends on the dimensions of the holes, on the sizes of the mesh lattice, and possibly on the shape and edge type of each hole, which could not be controlled during the process.

We want to verify if we can observe similar behaviors by simulating nanomesh transistors with different geometrical parameters. However, our simulations will be performed on different transistors of nano-scale size. This is due to the fact that the approximate expressions for the nanomesh gaps are obtained for nanometric meshes and lattice periods, so that we keep this range of parameters in order to apply those formulas.

The dimensions of the unit cell of our scaled nanomesh samples are  $l_{\text{hole}} = 1\ \text{nm}$ ,  $L_{\text{cell}} = 2\ \text{nm}$  (case No. 1),  $l_{\text{hole}} = 1.5\ \text{nm}$ ,  $L_{\text{cell}} = 3\ \text{nm}$  (case No. 2),  $l_{\text{hole}} = 2\ \text{nm}$ ,  $L_{\text{cell}} = 3.5\ \text{nm}$  (case No. 3). In all these cases, both triangular-shape and square-shaped holes have been studied.  $l_{\text{hole}}$  is the length of one side of each hole, while  $L_{\text{cell}}$  is the length of one side of the unit cell of the nanomesh. We compare each nanomesh FET with a nano-ribbon FET of width  $W$ .  $W$  has been chosen so that it corresponds to approximately five unit cells of the corresponding nanomesh sample along the transverse direction. This is done in order to compare two devices of comparable widths. While the widths of the nano-mesh samples are not uniquely defined in the method, the energy gap used to model the nano-mesh would require a large array of cells. We have then considered five cells along the width as a minimal threshold to use the analytic energy gaps.

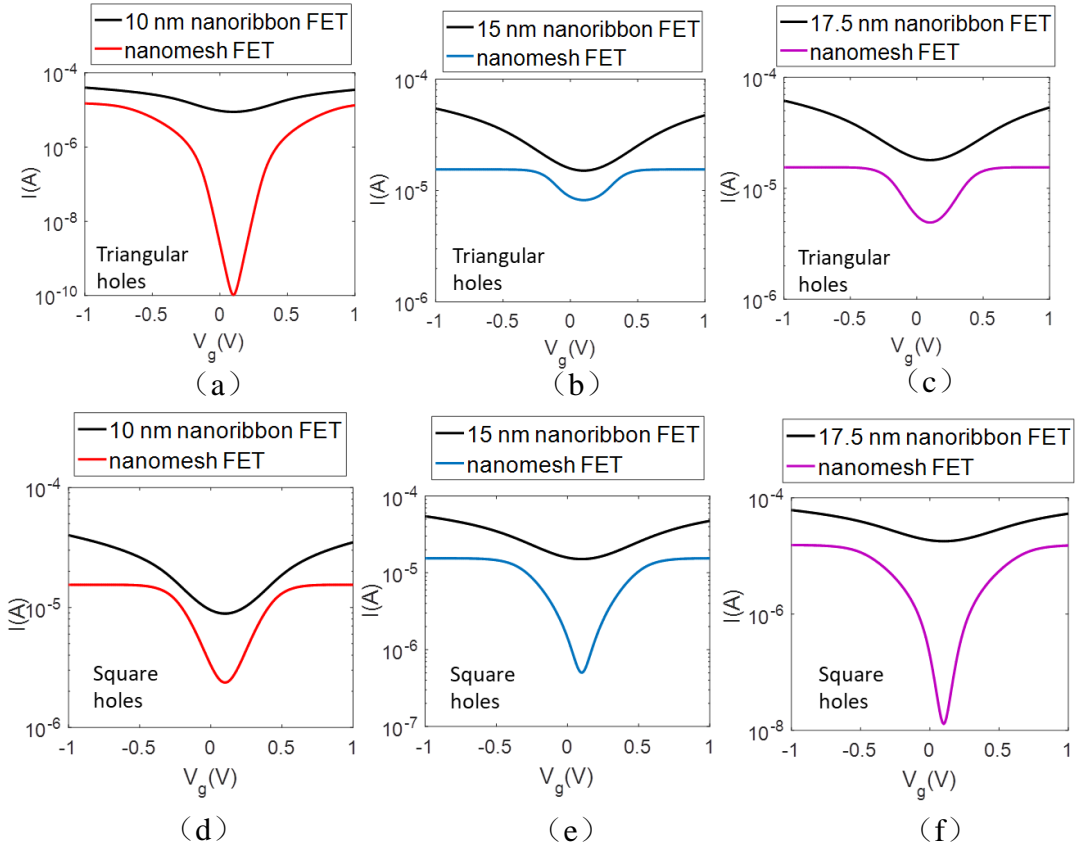


Figure 3.18: Transfer characteristics of scaled nanomesh FET with different geometrical configuration. (a) Triangular holes,  $l_{t-hole} = 1$  nm,  $L_{t-cell} = 2$  nm. (b) Triangular holes,  $l_{t-hole} = 1.5$  nm,  $L_{t-cell} = 3$  nm. (c) Triangular holes,  $l_{t-hole} = 2$  nm,  $L_{t-cell} = 3.5$  nm. (d) Square holes,  $l_{r-hole} = 1$  nm  $\approx 9$  carbon atom,  $L_{r-cell} = 2$  nm. (e) Square shape holes,  $l_{r-hole} = 1.5$  nm  $\approx 13$  carbon atom,  $L_{r-cell} = 3$  nm. (f) Square holes,  $l_{r-hole} = 2$  nm  $\approx 17$  carbon atom,  $L_{r-cell} = 3.5$  nm.

In Figure 3.18(a) (b) (c), we show  $I$ - $V$  characteristics of graphene nanomesh FET with triangular holes. In Figure 3.18(d) (e) (f), we show  $I$ - $V$  characteristics of graphene nanomesh FET with square holes. From Figure 3.18, we can find the scaled nanomesh transistor No.1 shows improved on-off current ratio with triangular holes. However, if the hole shape is a square, the scaled nanomesh transistor No.1 does not shown a significant improvement if compared with the reference nanoribbon transistors. The reason for this phenomenon is the different fitting parameter in Table 3.1 according to the number of removed atoms along the side of a hole.

Due to the sensitivity of these parameters according to the size of each hole, we perform another analysis by slightly modifying the size of each hole with respect to the Figure 3.18(d)-(f) in order to get the same parameter for the three cases. In Figure 3.19(a), we consider square holes of 10 carbon atoms instead of 9 in the FET of Figure 3.18(d) (see Figure 3.19(a)); we keep the same hole as in Figure 3.18(e) (see Figure 3.19(b)); we consider square hole of 16 atoms instead of 17 in the FET of Figure 3.18(f) (see Figure 3.19(c)). These three nanomesh samples have now the same fitting parameter, and the difference among the energy gaps depend only on the sizes of the holes and the lattice period. Energy gaps of 0.5062eV, 0.3043eV, 0.2783eV are obtained for the three different transistors, respectively. Also in this case, the numerical results in Figure 3.19 confirm that the very different impact on the on/off current ratio can be obtained by playing with the geometric features of the nanomesh channel.

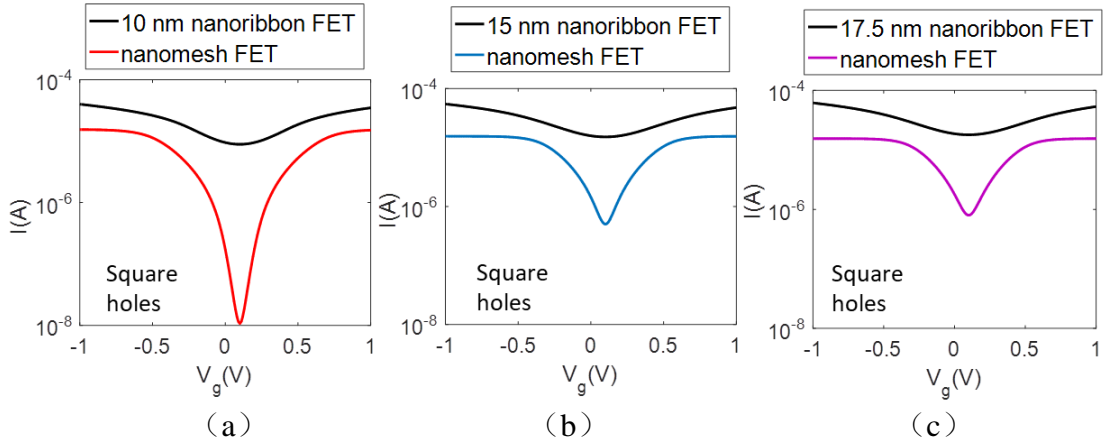


Figure 3.19: Transfer characteristics of nanomesh FET with different geometrical configurations and square-shaped holes. (a)  $l_{r-hole} = 1.1 \text{ nm} \approx 10$  carbon atom,  $L_{r-hole} = 2 \text{ nm}$ . (b)  $l_{r-hole} = 1.5 \text{ nm} \approx 13$  carbon atom,  $L_{r-hole} = 3 \text{ nm}$ . (c)  $l_{r-hole} = 1.84 \text{ nm} \approx 16$  carbon atom,  $L_{r-hole} = 3.5 \text{ nm}$ .

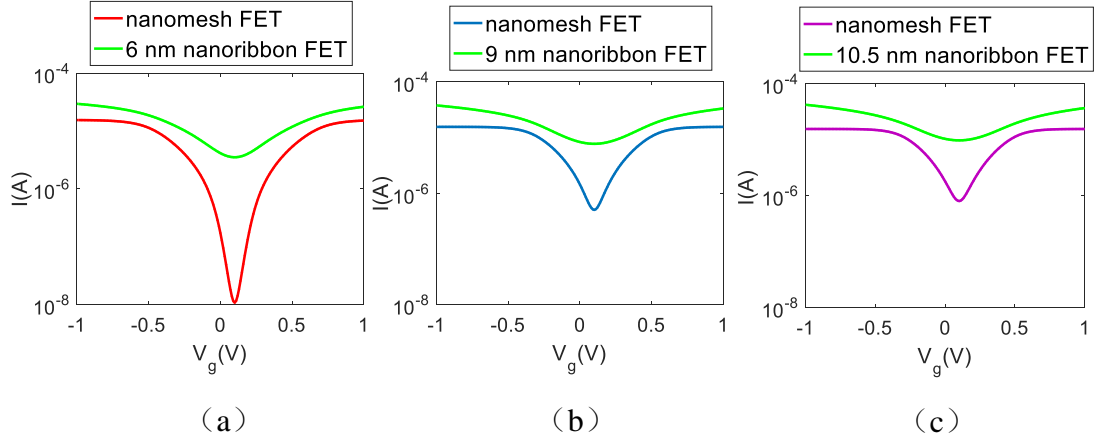


Figure 3.20: Comparison of transfer characteristics of nanomesh FET and different geometrical nanoribbon FET. (a) Nanomesh:  $l_{r-hole} = 1.1 \text{ nm} \approx 10$  carbon atom,  $L_{r-hole} = 2 \text{ nm}$ ; nanoribbon: length 6 nm. (b) Nanomesh:  $l_{r-hole} = 1.5 \text{ nm} \approx 13$  carbon atom,  $L_{r-hole} = 3 \text{ nm}$ ; nanoribbon: length 9 nm. (c) Nanomesh:  $l_{r-hole} = 1.84 \text{ nm} \approx 16$  carbon atom,  $L_{r-hole} = 3.5 \text{ nm}$ ; nanoribbon: length 9nm.

In Figure 3.20, we change the width of the reference nanoribbon to approximately three nanomesh unit cells. From these comparisons, we can see that even in this case, the on/off current ratios of graphene nanomesh FET are larger than graphene nanoribbon FET. In Figure 3.20,  $I$ - $V$  characteristics of graphene nanomesh FET are compared with  $I$ - $V$  characteristics of graphene nanoribbon FET for different design parameter values.

## Conclusions and Perspectives

In this thesis we have studied two cases of carbon-based nano-transistor in ballistic and partially-ballistic transport regimes, by applying a semi-analytical method involving a multiscale analysis of the device. The charge carriers are computed both by means of a suitable integration over the energy bands of the carbon-based channel, and by means of an electrostatic approach. In the geometry considered here, the Poisson equation does not need to be solved numerically since closed-form expressions for the contact capacitances are available.

Mechanical deformations on graphene nanoribbon-based FETs have been investigated thanks to a simple method to determine the effect of small deformations on electric properties of nanoribbons. The same information on geometrical deformation is retained in the electrostatic analysis, where the capacitance of contacts is modified accordingly. These kinds of deformation phenomena may occur in flexible electronics, where components can be submitted to different strains. In this context, small but not negligible deformations will occur; we found that if the relative deformation is small, the current variations are not strong enough to jeopardize the good functioning of the devices in terms of on/off current ratio. However, if larger deformation occurs, the energy gap created by cutting the nanoribbon can disappear and the FET current ratio can be degraded. As is well known, the smaller is the width of the nanoribbon, the more effective is the gap opening. This means that a larger on/off current ratio is obtained. Results show that, since small-width nanoribbon have a gap more resistant to deformation (i.e., a larger deformation is required to obtain a zero gap), their current ratio is also more robust to deformation. A validation with an *ab-initio* approach proved the correctness of the method, which can lead to a very fast modeling of deformed both ballistic and partially ballistic conduction regimes. Experimental results involving the fabrication of graphene on flexible substrates and the measurement of deformed transistors have been carried out during a visit at Chang Gung University, Taiwan. Namely, measurements on transistors with different deformations do show a variation of the current level. However, due to the relative large size of the transistor measured, to a on/off current ratio not very high, and to the possible presence of non-ideal behavior (e.g. contact deformation and partial breaking) the effects due to quantum confinement emerged in the model cannot be directly observed in the experiments.

As a second case of carbon-based nanotransistor, the effect of different geometrical configurations of graphene nanomesh transistors has been studied with the compact model. A ballistic regime has been considered for this study; the energy gap of the nanomesh channel has been estimated thanks to closed-form expressions proposed in the literature, resulting from a fitting of *ab-initio* simulations. Again, our FET model shows good agreement with a more complex model based on an *ab-initio* method. Our numerical results for nano-scale transistors in ballistic regime confirm that nanomesh can significantly improve the on-off current ratio of the transistor. However, the variability of the energy gap of the nanomesh with respect to different geometric parameters should warn about possible limitations of this technique. The size of the hole, the distance between adjacent holes, the shape of the hole, and the kind of edge of each hole (zigzag or armchair) are all parameters which affect the on-off current ratio in a non-negligible way. The cases of triangular and rhombic holes have been analyzed in detail. Also in this case, experimental results have been shown on micro-scale transistors. They confirm that for micro-scale transistor on-off current ratio is dependent on the different geometric parameters (the distance and the size of the hole, since the shape and edge type could not be controlled) and that the current ratio improvement can be achieved or not, according to the dimensions chosen.

The results presented lead to further work necessary to study more complex structures and increase the accuracy of the model. The response of nano-ribbon FET to deformation could lead to the design of nanosensors sensitive to deformation on the basis of their current ratio. *Ab-initio* simulations should be performed to assess the impact of more complex deformations such as those due to nanoparticles placed on the FET, which would not define a simple longitudinal strain.

The study of nanomesh FET will require further work to assess how the behavior observed scale with dimensions. Finally, *ab-initio* results could help us to characterize deformations in nanomesh and to evaluate the response of this kind of transistors to mechanical strains. This analysis could be of interest in flexible electronics and for application to nanosensors.

## **Annex: Experiments on graphene transistors at Chang Gung University**

In this annex we briefly describe some research activities conducted during a research stay at CGU (Chang Gung University, Taiwan) in summer 2017. At CGU, several projects involve the use of graphene. Among other activities, the participation to the fabrication and measurement of graphene nano-transistor are briefly described here. This activities were meant to complete the analysis of the impact of deformation on graphene-based transistors from an experimental point of view. It should be pointed out that, due to the facilities available at Chang Gung University, the size of the transistors fabricated and measured is not of the order of the nanoribbon FET simulated in the previous part of this chapter. The results of this section will then be compared only qualitatively to those previously obtained.

### **A.1 Chemical Vapor Deposition (CVD) method to produce graphene and graphene transfer technology**



Figure A.1: 1100°C Tube Furnace in CGU.

In CGU, the research work was cooperated with a Ph.D student, Mamina SAHOO. In this project, we wanted to study the effect of deformation on graphene in nano-transistors. Graphene was fabricated by using Chemical Vapor Deposition (CVD) method.

Firstly, copper film was cut into a suitable shape and then it was rolled in a cylinder. The cylinder copper film was inserted into the furnace tube (as Figure A.1 shows). The

graphene growth temperature was set to 1000°C. Mixed gas (methane and hydrogen) was introduced into the tube for 20 minutes and the graphene was extracted once the tube to cooled down to the room temperature.

Graphene transfer was based on poly methyl methacrylate (PMMA) method. The transfer media we choose to use is PMMA, which has a strong interaction with graphene. The PMMA coating graphene-Copper film substrate then can be immersed into diluted FeCl<sub>3</sub> solution. Copper foil will be etched and PMMA graphene will be separated. Then PMMA graphene was immersed into deionized water in order to remove residues. After this process, we could get clean PMMA graphene and transfer it to the substrate. Lastly, the PMMA can be removed by acetone at 90 °C.

## A.2 Deformation of pristine graphene based transistor in CGU

Figure A.2 shows the structure of GFET tested in CGU. In Figure A.2 naturally formed Al<sub>x</sub>O<sub>x</sub> acts as a dielectric layer. The source and drain are made of Nichel and the gate of Aluminum.

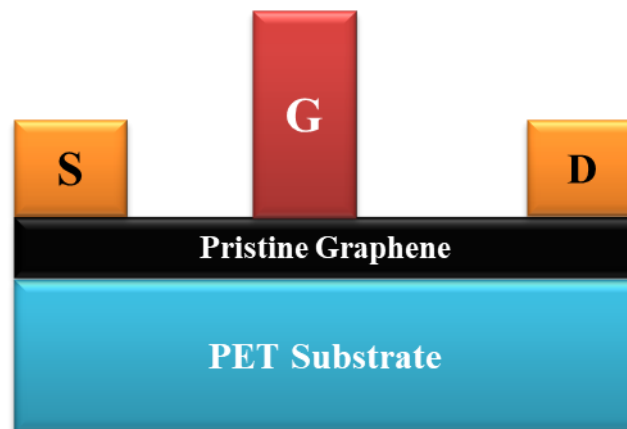


Figure A.2: GFET with naturally formed Al<sub>x</sub>O<sub>x</sub> as dielectrics on flexible substrate.

We have used rectangular graphene as the channel material in transistor, which dimension is 30\*50 μm. Then measurements are conducted in order to check possible transfer characteristics variation occurring for different deformations. As shown in Figure A.3, we paste the same transistor on different metallic cylinders. These metallic cylinders have different diameters 6 mm, 8 mm, 10 mm. For each measurement, the transistor will suffer different strain.

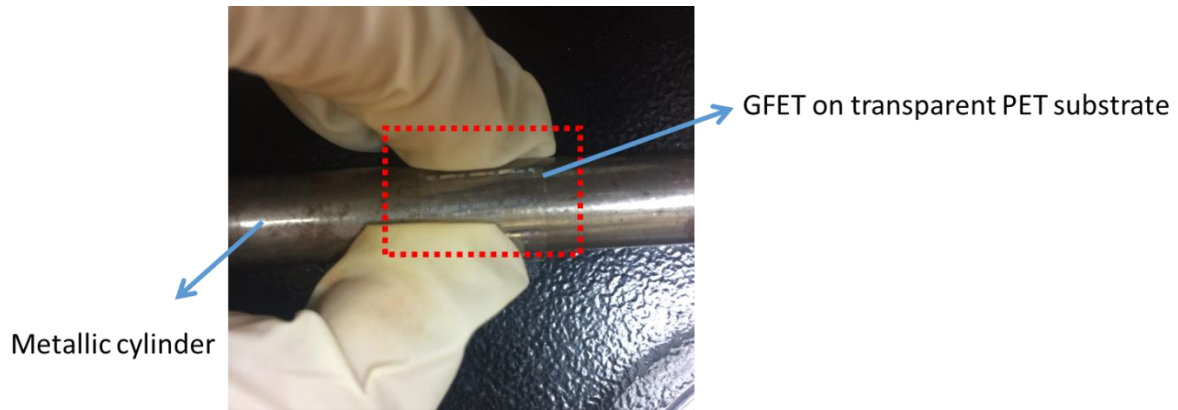


Figure A.3: GFET on transparent PET substrate which paste on metallic cylinder.

We have fixed the metallic cylinder on the platform and kept a constant potential  $V_{DS}$  to obtain the transfer characteristics. During this process, B1500A Semiconductor Device Parameter Analyzer was used in the CGU semiconducting lab (see Figure A.4).



Figure A.4: B1500A Semiconductor Device Parameter Analyzer.

In Figure A.5, we plot the  $I$ - $V$  characteristics. In Figure A.5 (a), the transistor is fixed on the flat platform, In Figure A.5 (b), the transistor is pasted on the metallic cylinder with diameter 10 mm, In Figure A.5(c), a metallic cylinder with diameter 8 mm is used. In Figure A.5 (d), a metallic cylinder with diameter 6 mm is used. In all cases,  $I_{ds}$  is varied by keeping a constant potential  $V_{DS} = 2$  V and changing the gate potential  $V_g$ .

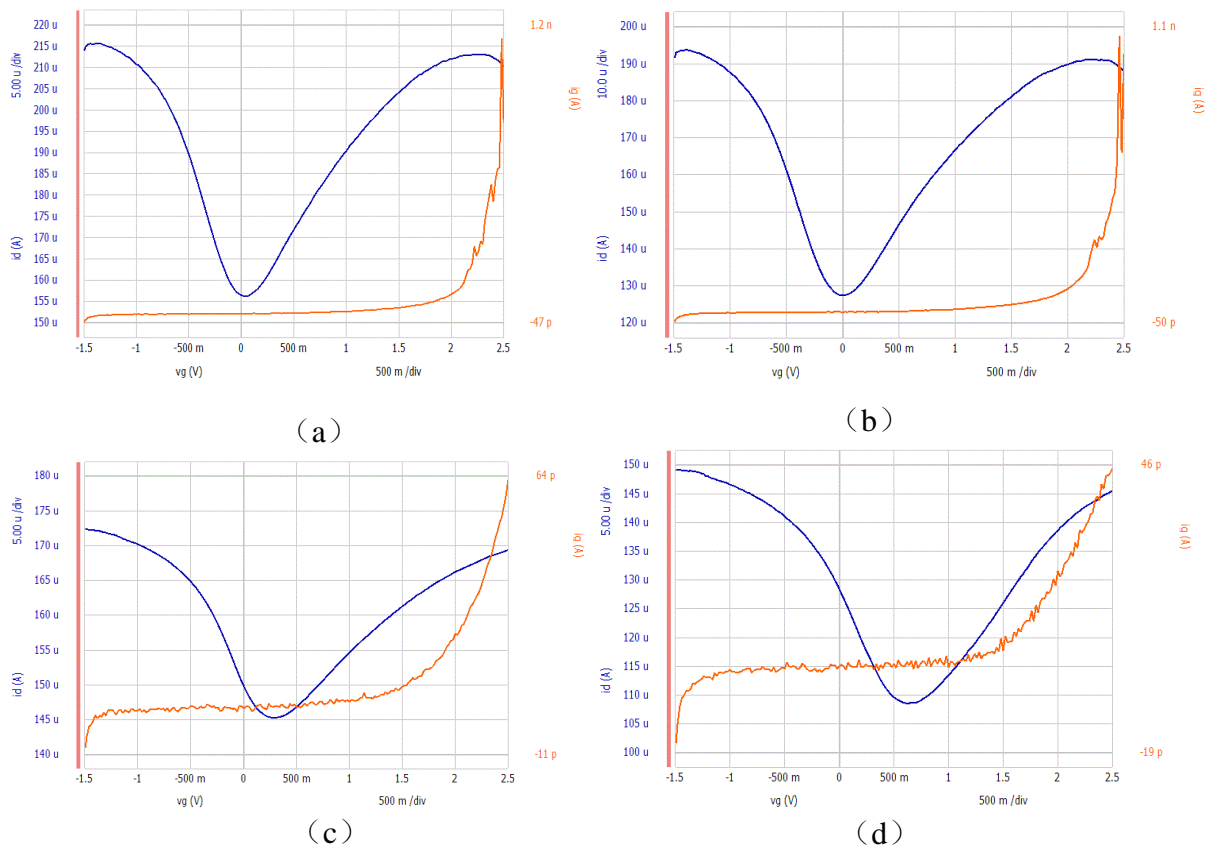


Figure A.5:  $I$ - $V$  Characteristics for same transistor pasted on different metallic cylinder (blue curve, represents  $I_d$  vs.  $V_g$ ): (a) normal and flat platform (b) transistor pasted on metallic cylinder which diameter is 10 mm (c) transistor pasted on metallic cylinder which diameter is 8 mm (d) transistor pasted on metallic cylinder which diameter is 6 mm.

In order to compare the  $I$ - $V$  characteristics under different situations, we plot these transfer characteristics in Figure A.6. In Figure A.6, we can see the observable variation in the current due to different deformations.

It has to be stated that a direct comparison with the simulated transistors of the previous sections is not possible. The size of the transistors fabricated and measured is much larger than the size of the nano-ribbon considered for simulation. Furthermore, we could not enforce a specific edge type of the graphene sample (aGNR in our simulations). Finally, different non-ideal effects could happen during the measurements (such as defects and contacts imperfections related to the deformation).

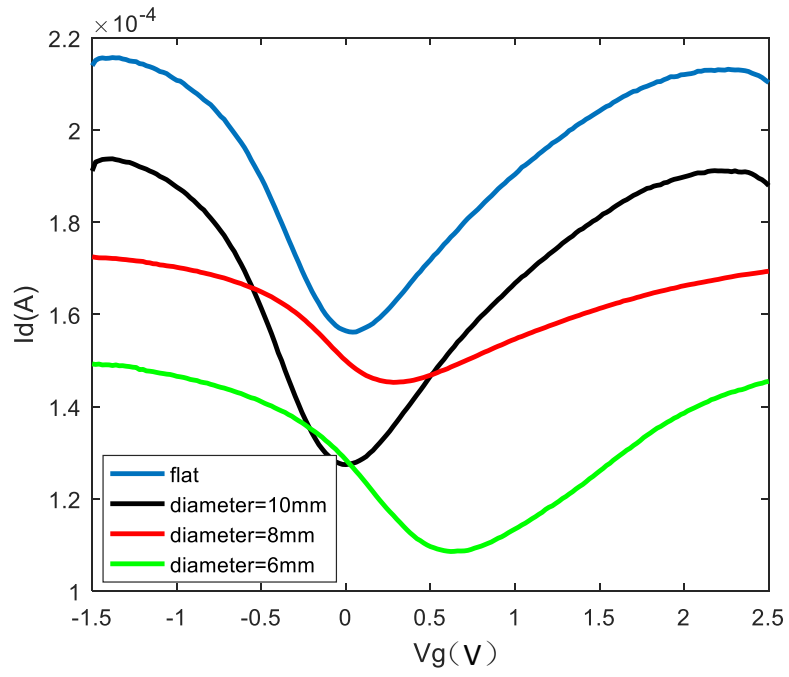


Figure A.6: Source-drain current  $I_{ds}$ .  $I_{ds}$  vs.  $V_g$ , at  $V_{ds} = 2$  V with ohmic contacts.

# List of Publications

## International Journal Papers:

- [1] Yi Zheng, Guido Valerio, and Zhuoxiang Ren, “Effects of Mechanical Stresses on Graphene-based Devices”, International Journal of Numerical Modelling: Electronic Networks, Devices and Fields, 2017.
- [2] Yi Zheng, Fernando Zanella, Guido Valerio, and Zhuoxiang Ren, César Augusto Dartora, “Study of Carbon-Based Transistors with Semi-Analytic and *Ab initio* Models”, IEEE Transactions on Magnetics, 2017.
- [3] Y. Zheng, F. Zanella, J. Njeim, C. A. Dartora, E. Cambril, A. Madouri, D. Brunel, G. Valerio, and Z. Ren, "Numerical and Experimental Study of Graphene Nanomesh for Field Effect Transistor", in preparation.

## International Conferences:

- [1] Yi Zheng, Guido Valerio, and Zhuoxiang Ren, “Effects of Mechanical Stresses on Graphene-based Devices”, in Proceedings of the 10th International Symposium on Electric and Magnetic Fields (EMF), 2016.
- [2] Yi Zheng, Guido Valerio, and Zhuoxiang Ren, “Effect of Deformations on Carbon-Based Transistors in Ballistic and Partially Ballistic Regimes”, in Proceedings of the 17th Biennial IEEE Conference on Electromagnetic Field Computation (CEFC), 2016.
- [3] Yi Zheng, Fernando Zanella, Guido Valerio, and Zhuoxiang Ren, César Augusto Dartora, “Study of Carbon-Based Transistors with Semi-Analytic and Full-Band Models”, in Proceedings of the 21st International Conference on the Computation of Electromagnetic Fields (COMPUMAG), 2017.
- [4] Yi Zheng, Guido Valerio, and Zhuoxiang Ren, “Study of Deformation on Nanoribbon-Graphene Transistors”, International Electron Devices & Materials Symposium (IEDMS), 2017.
- [5] Fernando Zanella, César Augusto Dartora, Yi Zheng, Guido Valerio, and Zhuoxiang Ren, “Numerical Technique to Describe Memory Phenomena in Nano Devices”, in Proceedings of the 9th European Conference on Numerical Methods in Electromagnetics (NUMELEC), 2017.

- [6] Y. Zheng, F. Zanella, J. Njeim, C. A. Dartora, E. Cambriil, A. Madouri, D. Brunel, G. Valerio, and Z. Ren, "Numerical and Experimental Study of Graphene Nanomesh for Field Effect Transistor", in Proceedings of the 18th Biennial IEEE Conference on Electromagnetic Field Computation (CEFC), 2018.

## Bibliography

- [1].J. Bardeen, "Semiconductor research leading to the point contact transistor," Nobel Lecture, December 11, 1956.
- [2].G. Moore, "Cramming more components onto integrated circuits," Electronics, retrieved 2016-07-01.
- [3].P. Avouris, J. Appenzeller, R. Martel, and S. Wind, "Carbon nanotube electronics," Proc. IEEE, vol. 91, no. 11, pp. 1772–1784, Nov. 2003.
- [4].R. Martel, H. S. P. Wong, K. Chan, and P. Avouris, "Carbon nanotube field effect transistors for logic applications," in IEDM Tech. Dig., pp. 159–162, 2001.
- [5].A. Javey, J. Guo, Q. Wang, M. Lundstrom, and H. Dai, "Ballistic carbon nanotube field-effect transistors," Nature, vol. 424, no. 6949, p. 654, Aug. 2003.
- [6].W. J. Hyun, E. B. Secor, M. C. Hersam, C. Daniel Frisbie, L. F. Francis, "High - resolution patterning of graphene by screen printing with a silicon stencil for highly flexible printed electronics," Advanced Materials, vol. 27, no 1, pp. 109-115, 2015.
- [7]. "IBM builds graphene chip that's 10,000 times faster, using standard CMOS processes," <https://www.extremetech.com/extreme/175727-ibm-builds-graphene-chip-thats-10000-times-faster-using-standard-cmos-processes>
- [8].H. LEE, et al. "A graphene-based electrochemical device with thermoresponsive microneedles for diabetes monitoring and therapy," Nature nanotechnology, 2016.
- [9].Research reveals how graphene can boost touchscreen flexibility, <http://www.surrey.ac.uk/features/research-reveals-how-graphene-can-boost-touchscreen-flexibility>
- [10].A graphene patch that monitors and possibly treats diabetes, <https://arstechnica.com/science/2016/03/a-graphene-patch-that-monitors-and-possibly-treats-diabetes/>
- [11].K. Geim and K. S. Novoselov, "The rise of graphene," Nat. Mater., 6-18391, 2007.
- [12].H. S. Philip Wong and D. Akinwande, "Carbon nanotube and Graphene Device Physics," Cambridge University Press, 2011.
- [13].K. S. Novoselov, A. K. Geim, S. V. Morozov, D. Jiang, Y. Zhang, S. V. Dubonos, I. V. Crigorieva, A. A. Firsov, "Electric Field Effect in Atomically Thin Carbon Films," Science, 306, 666–669, 2004.

- [14].What is Graphene? An In-depth Look into Graphene,  
<http://graphenewholesale.com/what-is-graphene/>
- [15].C. Lee, X. Wei, J. W. Kysar, J. Hone, "Measurement of the Elastic Properties and Intrinsic Strength of Monolayer Graphene". *Science*. 321 (5887): 385–8, 2008.
- [16].A. A. Balandin, S. Ghosh, W. Bao, I. Calizo, D. Teweldebrhan, F. Miao, C. N. Lau, "Superior Thermal Conductivity of Single-Layer Graphene". *Nano Letters ASAP*. 8 (3): 902–907, 20 February 2008.
- [17]. "ASTM A36 Grade Shape structural shape Steel - Matmatch". [matmatch.com](http://matmatch.com). Retrieved 2018-06-08.
- [18]. "Elastic Properties and Young Modulus for some Materials," The Engineering ToolBox, [https://www.engineeringtoolbox.com/young-modulus-d\\_417.html](https://www.engineeringtoolbox.com/young-modulus-d_417.html).
- [19]. "Thermal Conductivity of common Materials and Gases," [www.engineeringtoolbox.com](http://www.engineeringtoolbox.com).
- [20]. Electrical properties of silicon, Ioffe Institute Database,  
<http://www.ioffe.ru/SVA/NSM/Semicond/Si/electric.html>.
- [21]. W. VanRoosbroeck, "Theory of flow of electrons and holes in germanium and other semiconductors," *Bell System Technical Journal*, vol. 29, pp. 560-607, 1950.
- [22]. H. Gummel, "A self-consistent iterative scheme for one-dimensional steady state transistor calculations," *IEEE Trans. Electron Devices* ED-11, 455–465, 1964.
- [23]. V. Sverdlov, E. Ungersboeck, H. Kosina and S. Selberherr, "Current transport models for nanoscale semiconductor devices," *Mater. Sci. Eng. R* 58, 228–270, 2008.
- [24]. C. Jacoboni, P. Lugli, "The Monte Carlo Method for Semiconductor Device Simulation," Springer, Wien, New York, 1989.
- [25]. J. S. Martin, A. Bournel, and P. Dollfus, "On the Ballistic Transport in Nanometer-Scaled DG MOSFETs," *IEEE Transactions on Electron Devices*, Vol. 51, No. 7, July 2004.
- [26]. D. Querlioz et al., "On the ability of the particle Monte Carlo technique to include quantum effects in nano-MOSFET simulation," *IEEE Transactions on Electron Devices*, vol. 54, no. 9, pp. 2232-2242, Sept. 2007.
- [27]. C. L Gardner, "Semiconductor Device Simulation: the Hydrodynamic Model", *IEEE Potentials*, 22 (5), pp. 17-19, 2003.

- [28].R. Thoma, A. Emunds, B. Meinerzhagen, H. J. Peifer, and W. L. Engl, "Hydrodynamic equations for semiconductors with nonparabolic band structure," *IEEE Trans. Electron Devices*, vol. 38, pp. 1343–1353, June 1991.
- [29].K. Bloekjæ, "Transport equations in two-valley semiconductors," *IEEE Trans. Electron. Dev. ED-17*, 38–47, 1970.
- [30].V. Ryzhii, M. Ryzhii, and T. Otsuji, "Thermionic and tunneling transport mechanisms in graphene field-effect transistors," *Phys. Status Solidi A*, vol. 205, no. 7, pp. 1527–1533, Jul. 2008.
- [31].J. G. Champlain, "A first principles theoretical examination of graphene-based field effect transistors," *J. Appl. Phys.*, vol. 109, no. 8, p. 84515, Apr. 2011.
- [32].J. G. Champlain, "A physics-based, small-signal model for graphene field effect transistors," *Solid-State Electron.*, vol. 67, no. 1, pp. 53–62, Jan. 2012.
- [33].S. Thiele and F. Schwierz, "Modeling of the steady state characteristics of large-area graphene field-effect transistors," *J. Appl. Phys.*, vol. 110, no. 3, p. 34506, Aug. 2011.
- [34].M. G. Ancona, "Electron Transport in Graphene from a Diffusion-Drift Perspective," *IEEE Trans. Electron Devices*, vol. 57, no. 3, pp. 681–689, Mar. 2010.
- [35].V. H. Nguyen, A. Bournel, C. Chassat, and P. Dollfus, "Quantum transport of Dirac fermions in graphene field effect transistors", 2010 International Conference on Simulation of Semiconductor Processes and Devices (SISPAD), 2010.
- [36].I. Meric, M. Y. Han, A. F. Young, B. Ozyilmaz, P. Kim, and K. L. Shepard, "Current saturation in zero-bandgap, top-gated graphene field-effect transistors," *Nat. Nanotechnol.*, vol. 3, no. 11, pp. 654–659, Nov. 2008.
- [37].S. A. Thiele, J. A. Schaefer, and F. Schwierz, "Modeling of graphene metal-oxide-semiconductor field-effect transistors with gapless large-area graphene channels," *J. Appl. Phys.*, vol. 107, no. 9, p. 94505, May 2010.
- [38].S. Frégonèse, M. Magallo, C. Maneux, H. Happy, and T. Zimmer "Scalable Electrical Compact Modeling for Graphene FET Transistors," *IEEE Transactions on Nanotechnology*, Vol. 12, No. 4, July 2013.
- [39].H. Wang, A. Hsu, J. Kong, D. A. Antoniadis, and T. Palacios, "Compact Virtual-Source Current-Voltage Model for Top- and Back-Gated Graphene Field-Effect Transistors," *IEEE Trans. Electron Devices*, vol. 58, no. 5, pp. 1523–1533, May 2011.

- [40].D. Jimenez and O. Moldovan, "Explicit Drain-Current Model of Graphene Field-Effect Transistors Targeting Analog and Radio-Frequency Applications," *IEEE Trans. Electron Devices*, vol. 58, no. 11, pp. 4049–4052, Nov. 2011.
- [41].D. Jimenez, "Explicit Drain Current, Charge and Capacitance Model of Graphene Field-Effect Transistors," *IEEE Trans. Electron Devices*, vol. 58, no. 12, pp. 4377–4383, Dec. 2011.
- [42].O. Habibpour, J. Vukusic, and J. Stake, "A Large-Signal Graphene FET Model," *IEEE Trans. Electron Devices*, vol. 59, no. 4, pp. 968–975, Apr. 2012.
- [43].M. B. Henry and S. Das, "SPICE-compatible compact model for graphene field-effect transistors," in *2012 IEEE International Symposium on Circuits and Systems*, 2012, pp. 2521–2524.
- [44].K. N. Parrish and D. Akinwande, "An exactly solvable model for the graphene transistor in the quantum capacitance limit," *Appl. Phys. Lett.*, vol. 101, no. 5, p. 53501, Jul. 2012.
- [45].S. Frégonèse, N. Meng, H. N. Nguyen, C. Majek, C. Maneux, H. Happy, and T. Zimmer, "Electrical compact modelling of graphene transistors," *Solid-State Electron.*, vol. 73, pp. 27–31, Jul. 2012.
- [46].S. Frégonèse, M. Magallo, C. Maneux, H. Happy, and T. Zimmer, "Scalable Electrical Compact Modeling for Graphene FET Transistors," *IEEE Trans. Nanotechnol.*, vol. 12, no. 4, pp. 539–546, Jul. 2013.
- [47]. S. Rodriguez, S. Vaziri, A. Smith, S. Frégonèse, M. Ostling, M. C. Lemme, and A. Rusu, "A Comprehensive Graphene FET Model for Circuit Design," *IEEE Trans. Electron Devices*, vol. 61, no. 4, pp. 1199–1206, Apr. 2014.
- [48].I. J. Umoh, T. J. Kazmierski, and B. M. Al-Hashimi, "Multilayer Graphene FET Compact Circuit-Level Model with Temperature Effects," *IEEE Trans. Nanotechnol.*, vol. 13, no. 4, pp. 805–813, Jul. 2014.
- [49].S. Rakheja, Y. Wu, H. Wang, T. Palacios, P. Avouris, and D. A. Antoniadis, "An Ambipolar Virtual-Source-Based Charge-Current Compact Model for Nanoscale Graphene Transistors," *IEEE Trans. Nanotechnol.*, vol. 13, no. 5, pp. 1005–1013, Sep. 2014.
- [50].A. Behnam, A. S. Lyons, M. H. Bae, E. K. Chow, S. Islam, C. M. Neumann, and E. Pop, "Transport in nanoribbon interconnects obtained from graphene grown by chemical vapor deposition," *Nano Lett.* 12, 4424, 2012.

- [51].S. Datta, *Electronic Transport in Electronic Systems*. Cambridge University Press, Cambridge, 1995.
- [52].P. C. Martin and J. Schwinger, "Conservation Laws and the Quantum Theory of Transport: The early days," *Physical Review*, vol. 115, pp 1342-1358, 1959.
- [53].Y. Zheng, F. Zanella, G. Valerio, C. A. Dartora, and Z. Ren, "Study of Strain Effects on Carbon-Based Transistors with Semi-Analytic and Ab-Initio Models", *IEEE Transactions on Magnetics*, Vol. 54, No. 3, March 2018.
- [54].G. Mugnaini and G. Iannaccone, "Physics-based compact model of nanoscale MOSFETs-Part I: transition from drift-diffusion to ballistic transport," in *IEEE Transactions on Electron Devices*, vol. 52, no. 8, pp. 1795-1801, Aug. 2005.
- [55].G. Mugnaini and G. Iannaccone, "Physics-based compact model of nanoscale MOSFETs-Part II: effects of degeneracy on transport," in *IEEE Transactions on Electron Devices*, vol. 52, no. 8, pp. 1802-1806, Aug. 2005.
- [56].P. Michetti and G. Iannaccone, "Analytical model of one-dimensional carbon-based Schottky-barrier transistors," *IEEE Trans. Electr. Dev.*, vol. 57, no. 7, pp. 1616 - 1625 May 2010.
- [57].A. K. Kaw, E. E. Kalu, D. Nguyen, "Numerical methods with applications: Abridged," Chapter 3, 2008.
- [58].C. Sadlowski, S. Balderston, N. Sandhu, R. Hajian, C. Liu, T.P Tran, M. J. Conboy, J. Paredes, N. Murthy, I.M Conboy, and K. Aran, "Graphene-based biosensor for on-chip detection of bio-orthogonally labeled proteins to identify the circulating biomarkers of aging during heterochronic parabiosis," *Lab Chip*, 2018.
- [59].Z. H. Ni, T. Yu, Y. H. Lu, Y. Y. Wang, Y. P. Feng, and Z. X. Shen, "Uniaxial strain on graphene: Raman spectroscopy study and band-gap opening," *ACS Nano* 2, 2301-2305, 2008.
- [60].M. S. Sarker, M. M. Islam, M. R. Islam, "An analytical approach to study energy band structure in strained graphene," *Electrical Information and Communication Technology (EICT)*, 2013.
- [61].G. Gui, J. Li and J. Zhong, "Band structure engineering of graphene by strain: First-principles calculations," *Phys. Rev. B*, 78, 075435, 2008.

- [62].M. R. Moslemi, M. H. Sheikhi, K. Saghafi, M. K. Moravvej-Farshi, “Electronic properties of a dual-gated GNR-FET under uniaxial tensile strain,” *Microelectronics Reliability*, vol. 52, pp. 25792584, 2012.
- [63].K. Alam, “Uniaxial strain effects on the performance of a ballistic top gate graphene nanoribbon on insulator transistor,” *IEEE Trans. Nanotechnol.*, vol. 8, pp. 528534, 2009.
- [64].J. Bai et al., “Graphene nanomesh,” *Nature Nanotechnology*, volume 5, pp. 190–194, 2010.
- [65].R. Krishnakumar, R. S. Swathi, “Tunable Azacrown-Embedded Graphene Nanomeshes for Ion Sensing and Separation,” *ACS Appl. Mater. Interfaces*, 9 (1), pp 999–1010, 2017.
- [66].A. Zhang, H. F. Teoh, Z. Dai, Y. P. Feng, and C. Zhang, “Band gap engineering in graphene and hexagonal BN antidot lattices: A first principles study,” *Appl. Phys. Lett.* 98, 023105, 2011.
- [67].F. Ouyang, S. Peng, Z. Liu, and Z. Liu, “Bandgap Opening in Graphene Antidot Lattices: The Missing Half”, *ACS Nano* 5, 2011.
- [68].H. Sahin and S. Ciraci, “Structural, mechanical, and electronic properties of defect-patterned graphene nanomeshes from first principles”, *Phys. Rev. B* 84, 035452, 2011.
- [69].W. Oswald and Z. Wu, “Energy gaps in graphene nanomeshes,” *Phys. Rev. B* 85, 115431, 2012.
- [70].X. Liang, Y. S. Jung, S. Wu, A. Ismach, D. L. Olynick, S. Cabrini, and J. Bokor, “Formation of Bandgap and Subbands in Graphene Nanomeshes with Sub-10 nm Ribbon Width Fabricated via Nanoimprint Lithography,” *Nano Lett.* 10, 2454, 2010.
- [71].S. V. Rotkin, S. Subramoney, “Applied Physics of Carbon Nanotubes: Fundamentals of Theory, Optics and Transport Devices”, *NanoScience and Technology*, Springer, 2005 edition.
- [72].Y. W. Son, M. Cohen, and S. Louie, “Energy gaps in graphene nanoribbons,” *Phys. Rev. Lett.*, vol. 97, no. 21, p. 216 803, Nov. 2006.
- [73].L. Yang and J. Han, “Electronic structure of deformed carbon nanotubes,” *Phys. Rev. Lett.*, 85, 154–157, 2000.
- [74].Y. Li, X. Jiang, Z. Liu, and Z. Liu, “Strain Effects in Graphene and Graphene Nanoribbons: The Underlying Mechanism,” *Nano Research.*, 3(8): 545556, August 2010.
- [75].W. A. Harrison, “Electronic Structure and the Properties of Solids: The Physics of the Chemical Bond”, New York, 1989.

- [76].D. Akinwande, Y. Nishi and H. P. Wong, "An Analytical Derivation of the Density of States, Effective Mass, and Carrier Density for Achiral Carbon Nanotubes," *IEEE Transactions on Electron Devices*, vol. 55, no. 1, pp. 289-297, Jan. 2008.
- [77].B. El-Kareh, "Fundamentals of Semiconductor Processing Technologies," Kluwer Academic Publishers, 1995.
- [78].W. D. Callister and D. G. Rethwisch, "Materials Science and Engineering. An Introduction", 8th ed. New York, NY, USA: Wiley, 2006.
- [79].J. U. Lee, D. Yoon, and H. Cheong, "Estimation of young's modulus of graphene by raman spectroscopy", *Nano Lett.*, vol. 12, 2012.
- [80].P. C. Martin and J. Schwinger, "Conservation Laws and the Quantum Theory of Transport: The early days," *Physical Review*, vol. 115, pp 1342-1358, 1959.
- [81].M. Büttiker, "Small normal-metal loop coupled to an electron reservoir," *Phys. Rev. B, Condens. Matter*, vol. 32, no. 3, pp. 1846–1849, Aug. 1985.
- [82].M. Büttiker, "Role of quantum coherence in series resistors," *Phys. Rev. B, Condens. Matter*, vol. 33, no. 5, pp. 3020–3026, Mar. 1986.
- [83].L. Banszerus, M. Schmitz, S. Engels, M. Goldsche, K. Watanabe, T. Taniguchi, B. Beschoten, and C. Stampfer, "Ballistic transport exceeding 28  $\mu\text{m}$  in cvd grown graphene," *Nano Lett.* 2016, 16 (2), pp 1387–1391.
- [84].T. G. Pedersen, C. Flindt, J. Pedersen, N. A. Mortensen, A. P. Jauho, and K. Pedersen, "Graphene Antidot Lattices: Designed Defects and Spin Qubits," *Phys. Rev. Lett.* 100, 189905, 2008.
- [85].H. Jippo, M. Ohfuchi, and C. Kaneta, "Theoretical study on electron transport properties of graphene sheets with two-and one-dimensional periodic nanoholes," *Phys. Rev.B* 84, 075467, 2011.
- [86].Y. Yan, Q. F. Liang, H. Zhao, C. Q. Wu and B. Lid, "Thermoelectric electric properties of one-dimensional graphene antidot arrays", *Phys. Lett. A*376, 24252429, 2012.
- [87].V. Hung Nguyen, F. Mazzamuto, J. S. Martin, A. Bournel and P. Dollfus, "Graphene nanomesh-based devices exhibiting a strong negative differential conductance effect," *Nanotechnology* 23, 065201, 2012.
- [88].V. H. Nguyen, M. C. Nguyen, H. V. Nguyen, and P. Dollfus, "Disorder effects on electronic bandgap and transport in graphene-nanomesh-based structures," *J. Appl. Phys.* 113, 013702, 2013.

- [89].W. Liu, Z. F. Wang, Q. W. Shi, J. Yang, and F. Liu, "Band-gap scaling of graphene nanohole superlattices," *Phys. Rev. B* 80, 233405, 2009.
- [90].K. L. Ishikawa, T. Sato, "A Review on Ab Initio Approaches for Multielectron Dynamics," *IEEE Journal of Selected Topics in Quantum Mechanics*, Vol. 21, 2015.
- [91].Z. Han et al., "Homogeneous optical and electronic properties of graphene," *Adv. Funct. Mater.*, pp. 964-970, 2014.
- [92].Y. Zheng, F. Zanella, J. Njeim, C. A. Dartora, E. Cambril, A. Madouri, D. Brunel, G. Valerio, and Z. Ren, "Numerical and Experimental Study of Graphene Nanomesh for Field Effect Transistor", 18th Biennial IEEE Conference on Electromagnetic Field Computation (CEFC), 2018.